HAL
open science

The Electric Field at an Oxide Surface - Impact on Reactivity of Prebiotic Molecules

Sara Laporte

To cite this version:

Sara Laporte. The Electric Field at an Oxide Surface - Impact on Reactivity of Prebiotic Molecules. Chemical Physics [physics.chem-ph]. Université Pierre et Marie Curie - Paris VI, 2016. English. NNT : 2016PA066314 . tel-01469587

HAL Id: tel-01469587

https://theses.hal.science/tel-01469587v1

Submitted on 16 Feb 2017

HAL is a multi-disciplinary open access archive for the deposit and dissemination of scientific research documents, whether they are published or not. The documents may come from teaching and research institutions in France or abroad, or from public or private research centers.

L'archive ouverte pluridisciplinaire **HAL**, est destinée au dépôt et à la diffusion de documents scientifiques de niveau recherche, publiés ou non, émanant des établissements d'enseignement et de recherche français ou étrangers, des laboratoires publics ou privés.

Université Pierre et Marie Curie
École Doctorale de Physique et Chimie des Matériaux

The Electric Field at an Oxide Surface

Impact on Reactivity of Prebiotic Molecules

PhD Thesis

SARA LAPORTE

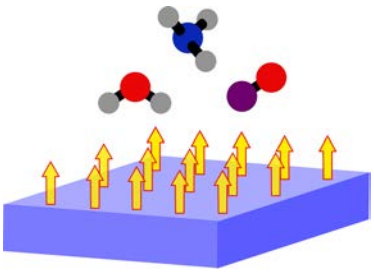

Supervisor: Antonino Marco Saitta

Paris, October 2016

Université Pierre et Marie Curie
École Doctorale de Physique et Chimie des Matériaux

The Electric Field at an Oxide Surface

Impact on Reactivity of Prebiotic Molecules

PhD Thesis

SARA LAPORTE

Supervisor: Antonino Marco Saitta

Defended on the 28th of September 2016

before the jury composed of :

Prof.	Dominique Costa	Examiner and Rapporteur
Prof.	Michiel Sprik	Examiner and Rapporteur
Prof.	Marie-Laure Bocquet	Examiner
Prof.	Mounir Tarek	Examiner
Prof.	Edouard Kierlik	Examiner
Prof.	Antonino Marco Saitta	PhD Supervisor
Prof.	Fabio Pietrucci	Invited Member

Paris, October 2016

Université Pierre et Marie Curie
École Doctorale de Physique et Chimie des Matériaux

Copyright © – All rights reserved. Sara Laporte, 2016.

(Signature)

.....
Sara Laporte

Abstract

Mineral surfaces are thought to be of importance to prebiotic chemistry due to their catalytic properties, which include a strong electric field at the interface. In this work the electric field at the surface of MgO and at the interface of MgO and water is studied through ab-initio molecular dynamics. The spontaneous electric field from the surface is found to be local and intense, on the order of V/Å, even when completely covered with water. A model prebiotic reaction is then studied on the model MgO surface: carbon monoxide and water yielding formic acid. Using metadynamics, reaction pathways were found with no a priori knowledge of the transition states, and umbrella sampling was then used to compute free energy landscapes to about 5 kcal/mol accuracy. The presence of the mineral surface was found to stabilise formic acid by at least 15 kcal/mol compared to the bulk case. The reaction was also studied in solution with an applied electric field of 0.3 V/Å, in order to estimate to impact of the surface electric field on the free energy landscape. The field is also found to stabilise the product, and formic acid is found to have a preferred orientation in the direction of both the applied electric field and the surface electric field. This work shows that near surface conditions (without direct adsorption) can significantly alter the free energy landscapes of chemical reactions, in a way which could be of importance for prebiotic chemistry.

Keywords

molecular dynamics; prebiotic chemistry; electric field; surface; MgO; formic acid

Acknowledgements

Thanks to everyone who helped me during this work!

I'd like to especially thank Marco my supervisor, who's enthusiasm and bright ideas have always made for an enjoyable research environment. Thanks also to Fabio F. for significant guidance in dealing with the simulation of the MgO surface, and Fabio P. who initiated me to the enhanced sampling methods found in this work. Thanks also to François, for helping to place the work in a geochemical context.

Thanks to the PHYSIX research team here at the lab, Stefan for answering my 'budget' related questions, Fred for recommending me at the end of my Master's, Sandra for helping find a teaching position.

I've had an impressive amount of colleagues here at IMPMC, a lot of whom have been important to me professionally and/or personally. I won't pretend to be able to name everyone of them without forgetting anyone. I'll stay 'local' by thanking my three-year long 'co-bureau' Adrien, for all the laughs and good discussions. Thanks also to Giuseppe, Silvio, and Andrea, for the lively group meetings and the practical help.

Zooming out a little, I want to thank my fellow PhD students (or doctors now!), and the post-docs as well (les non-permanents), many of whom have become close friends. I really don't want to start the list because I will forget people for sure (!!!) and to be cliché I will just say that you know who you are ;). Collectively I'd like to say that in this sometimes uncertain, sometimes stressful period, whether we choose to continue with research or not, it's really great to have friendship and support everyday. I hope the warm atmosphere between 'the young researchers' of IMPMC continues!

...and a special thanks to Fabien, obviously!! Looking forward to our next adventure!

Contents

Abstract **1**

Acknowledgements **3**

1 Introduction **7**

1.1 Prebiotic Context 8

1.2 Mineral Surfaces and Confined Water 9

1.3 The Electric Field 10

2 Theoretical Background **13**

2.1 Ab Initio Molecular Dynamics 14

2.1.1 Molecular Dynamics 14

2.1.2 Density Functional Theory 15

2.1.3 Car-Parrinello Molecular Dynamics 19

2.1.4 Applying an Electric Field via The Modern Theory of Polarisation 21

2.2 Accessing the Electric field 24

2.2.1 Application to a model surface 25

2.3 Enhanced Sampling Techniques 29

2.3.1 Parametrisation of the Free Energy Landscape 29

2.3.2 Metadynamics 31

2.3.3 Umbrella Sampling 33

3 The Electric Field at the Surface of MgO **35**

3.1 Introduction and Context 35

3.2 Static Results on Bare MgO 38

3.2.1 MgO(001) 38

3.2.2 MgO(111) and MgO(015) 40

3.3 One monolayer of H_2O on MgO(001) 44

3.4 Dynamic Results on the MgO/water Interface at 300K 45

3.4.1 Surface-assisted proton transfer 51

3.5 Mimicking the Surface Electric Field 54

3.5.1 Description and implementation 54

3.5.2 Tests and Remarks 54

3.5.3 Results 56
3.6 Conclusion 57

4 Surface Effects on a Pre-biotic Reaction **59**
4.1 Introduction and Context 59
4.2 Preliminary Study of the Configuration Space 60
4.3 Simulation Procedure 64
4.4 Temperature and Electric Field Effects 65
4.5 Effect of the Mineral Surface 68
4.6 Further Analysis 70
4.6.1 Entropic vs Enthalpic Contributions 71
4.6.2 Transition States and Isomers 73
4.7 Conclusion 75

5 Conclusions and Perspectives **77**

Appendices **79**

A Simulation Details **81**
A.1 Computational Details 81
A.1.1 AIMD with Quantum Espresso 81
A.1.2 Metadynamics and Umbrella Sampling with the Plumed Plugin 82
A.2 System Descriptions 83

Bibliography **96**

Chapter 1

Introduction

This study is motivated by two main points: there is a local electric field at the surface of minerals, and strong electric fields can significantly alter both the thermodynamics and kinetics of chemical reactions, such as prebiotic reactions. Although both mineral surfaces and electric fields can have a role in reactions leading to the building blocks of life, in ways which are outlined in this chapter, neither the surface electric field nor the strong fields present during the discharge in the Miller experiment [1] have been very much studied in this context, until recently [2]. The aim of this work is to identify links between prebiotic chemistry, a mineral surface and its electric field.

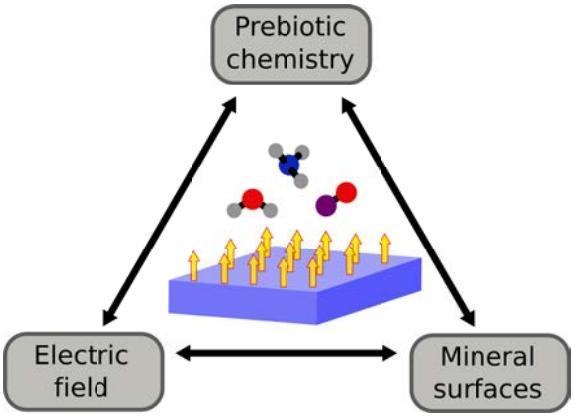

Figure 1.1: *Diagram of prebiotic molecules on a mineral surface. The electric field is represented by yellow arrows.*

The work is done using computer simulations, with specific methods briefly described in chapter 2. A model mineral surface was chosen, and the surface electric field was studied both in vacuum and in water, as detailed in chapter 3. The investigation of how the field from the model surface may influence a prebiotic reaction is presented in chapter 4. Finally, conclusions on the work and some perspectives are given in chapter 5.

1.1 Prebiotic Context

The question of how life came to be is one that has been repeatedly asked in many contexts. From a scientific point of view there are puzzles to be solved at every level of complexity, from the formation of the first amino acids and sugars, to oligomerisation and polymerisation of organic molecules, to the emergence of self-replicating systems all the way to the evolution of complex single and multi-cellular beings. The first step of this complexity ladder is known as prebiotic chemistry, which spans chemical reactions that took small molecules readily found in the interstellar medium or on the early earth to larger organic molecules and oligomers. Darwin, although he was reluctant to make this public [3], was one of the first to put forward the idea of the primordial soup in which these molecules could have first formed, but it wasn't until the Miller-Urey experiment [1] that the feasibility of this was verified experimentally. In the original Miller experiment an electric discharge, analogous to lightning on the early earth, was applied on a type of primordial gas mixture, consisting of water, methane, ammonia and hydrogen, which yielded various organic compounds such as amino acids and sugars. Since then pre-biotic theories have multiplied, and even though the precise composition of an early earth atmosphere is not completely agreed upon, variations of the Miller-Urey experiment have similarly been conducted with similar results – the atmosphere may have contained carbon mono- and dioxides, water, and nitrogen [4].

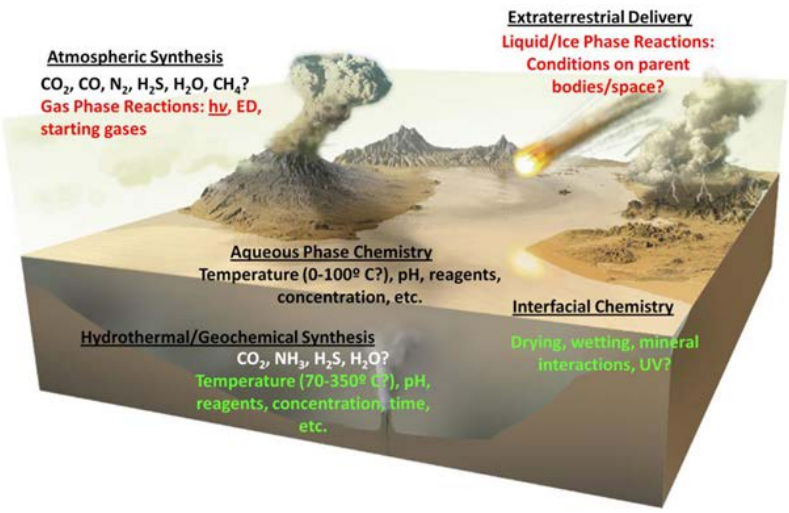

Figure 1.2: *Illustration of possible prebiotic scenarios on the early earth, taken from [5]*

The composition of the atmosphere is only one of the key questions in prebiotic chemistry. As summarised in figure 1.2, many prebiotic scenarios are possible,

and may or may not have occurred simultaneously, or in sequence throughout earth's early history. Extraterrestrial delivery scenarios postulate that prebiotic compounds are formed in outer space on asteroids or in the interstellar medium. Ribose may be synthesised from ultraviolet irradiation of interstellar ices [6] and the recent detection of amino acids and phosphorus on comet 67P/Churyumov–Gerasimenko by the Rosetta mission [7] adds weight to the extraterrestrial source of the building blocks of life. Such molecules could even have been synthesised during impact events on the early earth [8]. Other possible scenarios include hydrothermal synthesis with iron sulfide catalysts near deep ocean vents [9], and interfacial chemistry, in which wetting and drying cycles may have lead to accumulation and polymerisation of monomers [10]. In these examples and in many more not mentioned here, mineral surfaces hold a key role be it for their potential catalytic or confinement properties.

1.2 Mineral Surfaces and Confined Water

Many types of mineral surfaces have a key role in prebiotic chemistry scenarios. The surface of clay minerals are thought to aid in the polymerisation of amino acids, which is thermodynamically unfavourable in water alone [11, 12]. Clays as lamellar crystals can be hydrated, and the water confined therein is known to have special dielectric properties [13], as well as nucleation properties [14]. Anatase (TiO_2) is also a popular mineral in prebiotic chemistry, as it is photoactive and may have been abundant on the primitive earth. Coupled with shockwaves from meteoritic impacts, amino acids and sugars may have been formed on such surfaces [15]. Iron sulfides such as pyrite (FeS) [16] and greigite [9] could be of importance to prebiotic chemistry in the iron-sulphur world hypothesis, which is that the first autocatalytic metabolic precursors appeared on these minerals in hydrothermal conditions [17]. It has even been postulated that the enantiomeric nature of chiral molecules in living things today may be partly linked to the slight excess of one type of chiral quartz crystals with respect to the other on earth [18].

Aside from specific chemical or templating effects of mineral surfaces, the environment at mineral surfaces in general has been shown to differ greatly from the bulk, and this may result in catalytic properties. On surfaces in vacuum or in contact with a gas, molecules may adsorb and react on the surface, resulting in new species being formed. In the field of prebiotic chemistry this can result in formation of amino acids [19]. When the mineral is in contact with water, other special properties can be noticed. The first layer on the surface is often more dense than in the bulk, be it on graphene [20], BaF_2 [21], or oxides such as MgO [22], TiO_2 [23] and undoubtedly others. Furthermore, the dielectric properties

of confined water have very recently been found to differ from the bulk, even at a flexible surface [24]. This leads us to think of a general surface effect, not completely dependent on the specific chemistry, which may be due to the mere confinement and electrostatic properties at the interface. Confined water is known to freeze more easily [25, 26] and has in general different solvation properties than bulk water. In these examples, neither chemisorption nor physisorption is directly involved, and solvated molecules experience the surface effects by means of the confinement properties of the surface. As will be shown in chapter 3 these confinement properties may be partly reproduced by an appropriately shaped electric field, mimicking the lateral, coarse grained, electrostatic properties of a 'non-chemical' surface. In doing this we can hope to elucidate general effects of a surface electric field field which is proxy to confinement and some of the special properties of near surface conditions. Thus, in this work special focus is given to the spontaneous electric field at the surface, and the reader may be surprised by this choice which seems to ignore specific chemical effects. Indeed these obviously cannot be completely put aside, and the idea is to gauge to what extent the surface electric field can influence prebiotic reactions.

1.3 The Electric Field

It is known that an applied electric potential can modify reaction rates. Oriented electric fields at an STM tip have recently been shown to accelerate the formation of carbon-carbon bonds [27] thus expanding the field of electrostatic catalysis to beyond redox systems. Water structure is drastically modified when a strong external field is applied [28], and water molecules dissociate from fields of about 0.35 V/Å [29]. Furthermore, strong electric fields can modify reaction pathways and transition states, and new molecular species may be stabilised due to the rearrangement of valence electrons [30, 31, 32]. Enzyme catalysis has been shown to depend strongly on the high electric fields generated at the catalytic sites, which are on the order of V/Å [33]. These orders of magnitude for electric fields are too high to be applied uniformly to a macroscopic system, for example in a capacitor, because of dielectric breakdown resulting in a spark, or discharge across the medium. Nevertheless, on short scales, several V/Å is the order of magnitude that atoms and molecules feel locally from each other, and is definitely enough to cause rearrangement of valence electrons and strong polarisation. To forcibly apply such strong fields to a system one must use sharp electrode like in the setup of reference [34], or between a metallic surface and electrode tip like in reference [27]. Indeed, this is referred to as electrocatalysis, and is a form of heterogeneous catalysis where a surface potential can be tuned to get the desired catalytic properties. The experiment in reference [34] is particularly interesting

because the electric field at the tip induces crystallisation of proteins in solution, thereby showing that the electric field, as well as being important on the free energy of chemical reactions, clearly induces order due to it being a vector field.

The spontaneous electric field at an insulating surface cannot be modulated like at a metal surface. However, as has been shown in the literature before and as is shown in chapter 3, local fields at the surface are indeed very high and comparable to the field at the surface of enzymes for example. Recently, a 'spontelectric' phase of matter has been proposed [35], in which a high spontaneous electric field is maintained in thin films of solid carbon monoxide, which are known to exist on the surface of interstellar grains. Prebiotic chemistry may happen at the surface of such grains in the interstellar medium [6].

The electric double layer (EDL) models [36] describe solid-liquid interfaces by electrostatics. Two distinct examples of a double layers are shown schematically in figure 1.3, where we can see the electrostatic potential drop at the interface on the left panel, and the orientation of the dipoles of relevant water molecules in shown in the right panel. In the first case, the surface charge is positive, and in the second case it is negative, however in either case the double layer is formed by attraction of counter ions to the charged surface. If the surface is an electrode, the surface charge can be modulated however, in the case where the surface is an insulator, the surface charge is uniquely defined for specific surfaces depending on the pH of the solution. The point of zero charge (PZC) is the pH at which the surface is neutral and differs according to the surface type [37]. The double layer refers to the Stern layer, which is on the order of Å, and the diffuse layer in which the potential decays exponentially. The diffuse layer may extend nm to μm beyond the surface, depending on the ions in the electrolyte. Even without the presence of dissolved ions, water can act as an electrolyte due to its dipole moments and because on an oxide surface, depending on the PZC, either OH^- or H^+ may adsorb on the surface. The electric double layer is a simple example of how the spontaneous surface electric field may act, even in solution. In practise, the Stern layer can be simulated using molecular dynamics, including ions and counter ions [38, 39]. In the following work, ions are not included in the system and all calculations are run at neutral pH. This is in part due to the limited system size. Nonetheless, a steep potential drop in the Stern layer was reproduced, resulting in an electric field, as will be explained in detail in chapter 3.

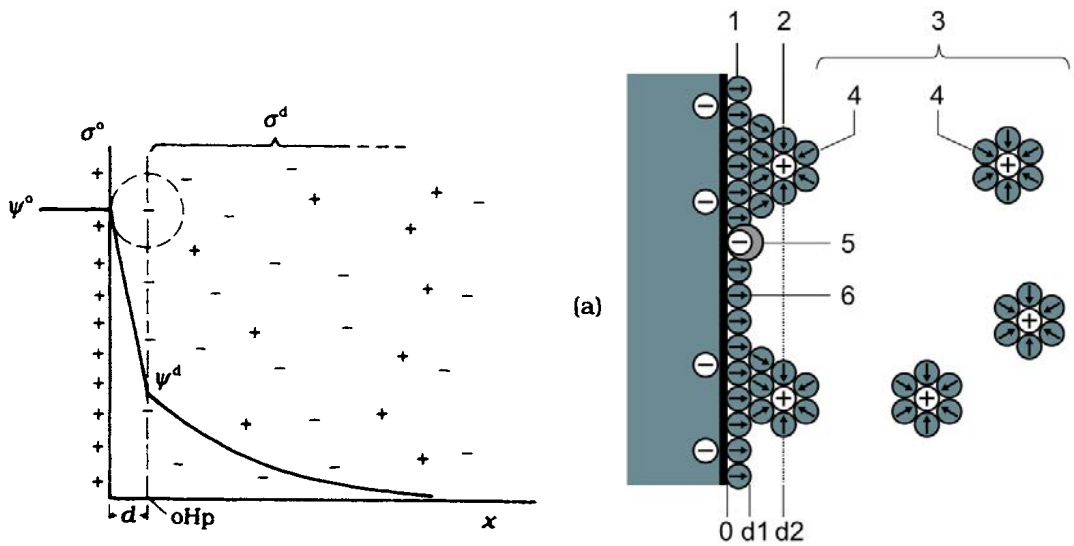

Figure 1.3: *Diagrams of the electric double layer. Left shows the electrostatic potential profiles and the distribution of ions in the diffuse layer. Taken from [36]. Right shows water dipoles as arrows and included a specifically adsorbed anion [40].*

Chapter 2

Theoretical Background

To model systems at the atomic level, molecular dynamics (MD) uses the atomic positions, forces given by atomic or molecular potentials, and the equations of motion (section 2.1.1). MD was performed with QUANTUM ESPRESSO [41], which uses density functional theory, DFT (section 2.1.2) to calculate electronic properties of materials as well as atomic and molecular potentials. *Ab-initio* molecular dynamics (AIMD) is the result of coupling MD and DFT — we calculate potentials through DFT rather than using empirical potentials. This is more costly in terms of computation time, but has the advantages of being a first-principles method and is able to account for dissociation and polarisation of molecules. An efficient way to use DFT with MD was devised by Car and Parrinello (section 2.1.3) which reduces the computation time significantly in certain cases, such as when applying an electric field through the modern theory of polarisation (section 2.1.4). The full vector electric field is accessible through analysis of the charge distribution, and various electric field profiles were obtained for the surface calculations, as outlined in section 2.2.

Enhanced sampling techniques were then used to induce reactions which are not accessible on an ab initio timescale. The reaction is described in terms of path coordinates explained in section 2.3.1 and exploratory metadynamics (section 2.3.2) was applied to get a reaction pathway involving solvent molecules explicitly. Finally umbrella sampling was used to obtain a precise free energy landscape. The umbrella sampling and weighted histogram analysis methods are outlined in section 2.3.3.

2.1 Ab Initio Molecular Dynamics

2.1.1 Molecular Dynamics

Molecular dynamics works by solving the many-bodied problem numerically, by integrating Newton's equation for each atom at each time step. We have for the ith atom:

$$\mathbf{a}_i = \ddot{\mathbf{R}}_i = \frac{\mathbf{F}_i}{m_i} \tag{2.1}$$

$\mathbf{R}_i$ being the atomic positions, m_i the respective masses and $\mathbf{F}_i$ the forces. A simple and effective way to integrate this numerically over a given timestep Δt is the Verlet algorithm. Assuming we can at each moment compute a potential $V(\mathbf{r})$ representing the interactions between particles, and that we have ion positions and velocities at time t, $\{\mathbf{R}_i(t); \mathbf{v}_i(t)\}$, the forces, the ion positions and ion velocities at the next timestep $t + \Delta t$ can be computed in the following way [42]:

$$\mathbf{F}_i(t) = -\nabla V(\mathbf{R}_i(t)) \tag{2.2}$$

$$\mathbf{R}_i(t+\Delta t) = \mathbf{R}_i(t) + \mathbf{v}_i(t)\Delta t + \frac{1}{2m_i}\mathbf{F}_i(t)\Delta t^2 \tag{2.3}$$

$$\mathbf{F}_i(t+\Delta t) = -\nabla V(\mathbf{R}_i(t+\Delta t)) \tag{2.4}$$

$$\mathbf{v}_i(t+\Delta t) = \mathbf{v}_i(t) + \frac{1}{2m_i}[\mathbf{F}_i(t) + \mathbf{F}_i(t+\Delta t)]\Delta t \tag{2.5}$$

In classical MD the inputs are the initial position and velocities of the molecules, as well as empirical potentials used to calculate forces between molecules. A famous example of such a potential is the Lennard-Jones potential, which approximates the interaction between two neutral atoms. Empirical potentials used in MD are usually more complex than this simple model, because they include parameters which have been fitted to experimental data, or to first-principles calculations. As well as modelling pair interactions potentials used in classical MD can include parameters for many-body interactions, and also parameters which control intramolecular degrees of freedom such as stretching and twisting.

Temperature Control

All MD in this work has been performed with a fixed number of atoms N in a box of a fixed volume V. In the microcanonical NVE ensemble, the temperature is not controlled and the total energy E is a constant of motion. Temperature is defined as by the average kinetic energy of the atoms:

$$KE_{\text{avg}} = \frac{3}{2}k_B T = \left\langle \frac{1}{2}mv^2 \right\rangle \tag{2.6}$$

thus the most simple way of controlling temperature is velocity rescaling – that is, if the instantaneous temperature T_{inst} defined above differs from the target temperature T the atomic velocities can be rescaled in the following way:

$$\mathbf{v}_{\text{new},i} = \lambda \, \mathbf{v}_i \tag{2.7}$$

where $\lambda = \sqrt{\frac{T}{T_{\text{inst}}}}$. The rescaling method is straightforward, however, in the limit where we rescale at every timestep, the statistical fluctuations of the microcanonical ensemble are not reproduced. In practice we can rescale at set time intervals, or when T_{inst} goes beyond a certain range of the targeted temperature. In this last case the rescaling will be applied often at the beginning of the simulation, but eventually the system will gather the right amount of potential energy so that its temperature does not fluctuate past the rescaling threshold. This is known as equilibrating the system. Indeed, starting from a correctly equilibrated configuration at a given temperature, we can begin dynamics with random velocities following the Maxwell-Boltzmann distribution at the correct temperature, and in principle run an NVE simulation which should result in a relatively constant temperature. In practice, even after thermalisation the system will eventually be dissipative due to numerical accuracy issues, and we can maintain the rescaling threshold which will effectively act at rare occasions. This is the protocol that has been applied throughout this work, and although there are much more sophisticated thermostats for MD, the NVE from a thermalised configuration followed by rare rescaling has proved to be sufficient in this case.

MD methods can be coupled to *ab-initio* calculations when the potential used in equation 2.2 is computed from first principles at each time step, using density functional theory. This is quite computation time demanding and cannot be used for large systems as with classical MD, but first principles methods allow for treatment of complex chemical events such as dissociation or forming of molecules. Furthermore, empirical potentials are often tuned to experimental results in a particular case, and can be inadequate when applied to different conditions. *Ab-initio* potentials are, in theory, adaptive to any chemical environment.

2.1.2 Density Functional Theory

Density Functional Theory (DFT) is widely used in condensed matter physics to calculate the band structure of solids and electronic properties. It is an *ab-initio*, or first-principles method because it follows from the Schrödinger equation, here given for N electrons:

$$H\Psi(\mathbf{r}_1, \cdots, \mathbf{r}_N) = \epsilon\Psi(\mathbf{r}_1, \cdots, \mathbf{r}_N) \tag{2.8}$$

Where H is the system Hamiltonian and $\Psi(\mathbf{r}_1, \cdots, \mathbf{r}_N)$ is the many electron wavefunction, with $\mathbf{r}_i$ the spacial coordinates. In this framework nuclei are considered classical, that is, only the electron wavefunction is calculated. The Hamiltonian is given as the sum of the kinetic energy, the external potential (including Coulomb interaction with the nuclei, here referred to as V_{ext}) and the Coulomb potential between electrons:

$$H = \sum_{i=1}^{N} \left[-\frac{\hbar^2 \nabla_i^2}{2m} + V_{\text{ext}}(\mathbf{r}_i) \right] + \frac{1}{4\pi\epsilon_0} \sum_{i>j} \frac{e^2}{\mathbf{r}_i - \mathbf{r}_j} \tag{2.9}$$

This can be solved approximately using the Hartree-Fock formalism by writing the many-electron wavefunction as a Slater determinant [42]:

$$\Psi(\mathbf{r}_1, \cdots, \mathbf{r}_N) \approx \Psi_{\text{HF}}(\mathbf{r}_1, \cdots, \mathbf{r}_N) = \frac{1}{\sqrt{N!}} \begin{vmatrix} \phi_1(\mathbf{r}_1) & \phi_2(\mathbf{r}_1) & \cdots & \phi_n(\mathbf{r}_1) \\ \phi_1(\mathbf{r}_2) & \phi_2(\mathbf{r}_2) & \cdots & \phi_n(\mathbf{r}_2) \\ \vdots & \vdots & \ddots & \vdots \\ \phi_1(\mathbf{r}_n) & \phi_2(\mathbf{r}_n) & \cdots & \phi_n(\mathbf{r}_n) \end{vmatrix} \tag{2.10}$$

Where ϕ_k are solutions to the single electron Hamiltonian. Taking the Slater determinant mixes the states while ensuring an anti-symmetric wavefunction. This method has the advantage that electron exchange is taken into account, however electron correlation is not fully described. Several post-Hartree–Fock methods exist to deal with this problem. These methods however are computationally expensive in that they require to keep track of the full many-body electron wavefunction.

Hohemberg and Kohn (H–K) [43] proved that the electron density uniquely determines the system Hamiltonian (and vice-versa), or in other words, that two different Hamiltonians cannot have the same ground state density for a system of N electrons. This is the basis for density functional theory (DFT). The Hohemberg and Kohn theorems also state that the energy is a unique functional of the electron density $E[n] = E_{\text{known}}[n] + E_{\text{XC}}[n]$, which is minimised when $n(\mathbf{r})$ is the ground state density.

We can define the electronic density by:

$$n(\mathbf{r}) = \int \mathrm{d}\mathbf{r}_2 \cdots \int \mathrm{d}\mathbf{r}_N |\Psi(\mathbf{r}, \mathbf{r}_2, \cdots, \mathbf{r}_N)| \tag{2.11}$$

The great advantage is that instead of solving for $\Psi(\mathbf{r}_1, \cdots, \mathbf{r}_N)$ depending on $3N$ variables, we now solve for $n(\mathbf{r})$, the electron density, which depends only on the three spacial variables. This means that using DFT as opposed to Hartree-Fock decreases the computation time significantly to treat many electron systems. We

arrive at an effective independent-particle Schrödinger equation, which we write here in Hartree atomic units[1]

$$\left[-\frac{\nabla^2}{2} - \sum_i \frac{Z_i}{|\mathbf{r}-\mathbf{R}_i|} + \int \frac{n(\mathbf{r}')}{|\mathbf{r}-\mathbf{r}'|} d^3r' + V_{\mathrm{XC}}[n](\mathbf{r})\right] \psi_k(\mathbf{r}) = \epsilon_k \psi_k(\mathbf{r}) \tag{2.12}$$

where the first term is the kinetic energy, the second term is the Coulomb potential between the electrons and the nuclei, and the third term is the electron-electron interaction. This is an independent particle representation which has the same electron density as the many electron wavefunction, however the orbitals $\psi_k(\mathbf{r})$ do not correspond to the 'real' electrons, which is why there is an extra term $V_{\mathrm{XC}}[n]$. This is the so-called exchange correlation potential, that is the energy coming from the fact that the electrons are not in fact independent particles. We note that the Hamiltonian depends on the electron density, which itself depends on the atomic orbitals:

$$n(\mathbf{r}) = \sum_{k=1}^{N} |\psi_k(\mathbf{r})|^2 \tag{2.13}$$

Equations 2.12 and 2.13 are thus solved self-consistently.

Although the H–K theorem states that it exists, the unique energy functional is not known, and in particular the exchange-correlation potential and energy terms:

$$V_{\mathrm{XC}}[n] = \frac{\delta}{\delta n(\mathbf{r})} E_{\mathrm{XC}}[n] \tag{2.14}$$

where $\frac{\delta}{\delta n(\mathbf{r})}$ expresses the functional derivative. Physically, this exchange correlation term accounts for the interaction between electrons as quantum particles. Various approximations for the energy functional exist, the most widely used being the Local Density Approximation (LDA), and Generalised Gradient Approximation (GGA):

- LDA makes the approximation that even if the electron density is not uniform in space, we can take the system to be a sum of small cells each with a uniform electron density. In the case of a homogeneous electron gas it is known that the exchange correlation energy per electron depends only on the mean value of the density, we write it as $e_{\mathrm{xc}}^{\mathrm{HEG}}(\bar{n})$. By replacing the mean density $\bar{n}$ with the local density $n(\mathbf{r})$ and summing over the volume we get the exchange correlation term:

$$E_{\mathrm{xc}}^{\mathrm{LDA}}[n] = \int n(\mathbf{r}) e_{\mathrm{xc}}^{\mathrm{HEG}}(n(\mathbf{r})) d^3r \tag{2.15}$$

[1] distances are in Bohr, masses are in electron mass units, charges in electron charges and the energy is in Hartrees.

- GGA is a correction to LDA. Because a real electron system is not homogeneous we need to take into account the density variations through functional dependencies on the gradient of the density:

$$E_{\mathrm{xc}}^{\mathrm{GGA}}[n] = E_{\mathrm{xc}}^{\mathrm{LDA}}[n] + \int e_{\mathrm{xc}}^{\mathrm{GGA}}(n(\mathbf{r}), \nabla n(\mathbf{r}))d^3r \tag{2.16}$$

  there are several expressions possible for $e_{\mathrm{xc}}^{\mathrm{GGA}}(n(\mathbf{r}), \nabla n(\mathbf{r}))$. For this work the Perdew, Burke and Ernzerhof (PBE) GGA functional was used [44].

To gain computation time, usually only the valence electrons are taken into account when performing DFT. This is through a method where the core electrons are approximated as a static potential around the ion position, called the pseudo-potential. This potential is a simplified version of the real core-electron potential which is identical to it on the 'outside', that is, after a certain distance away from the ion position. With the pseudo-potential method, equation 2.12 includes only valence electron wavefunctions, the ionic charge Z_i refers to the total charge of the nucleus *and* core electrons, and the pseudo-potential term is added [45].

Plane waves and periodic boundary conditions

When dealing with periodic systems such as crystals, DFT is usually based on a plane-waves basis set, whereby the electron wavefunctions are Bloch waves:

$$\psi(\mathbf{r}) = e^{i\mathbf{k}\cdot\mathbf{r}}u(\mathbf{r}) \tag{2.17}$$

where the plane wave is multiplied by the function $u(\mathbf{r})$ which has the same periodicity as the crystal. This proves to be efficient for periodic systems as from the Bloch theorem all states may be described in the first Brillouin zone in reciprocal space. This reciprocal space is sampled by the use of a k-point grid, which can be more or less dense depending on the required precision. If precision is required to calculate energies and electronic structure, the plane-wave basis can be expanded (increase of the 'cut-off' energy of the plane waves) and more k-points can be sampled. The size of Brillouin zone corresponding to a supercell is small in the case where the supercell is large. Thus in this work and many other AIMD studies, large supercells mean that only the highest symmetry point, called the Γ point, is enough to correctly sample the reciprocal space. Throughout this work the plane waves basis set was used, with single Γ k-point sampling.

Born–Oppenheimer MD

Standard DFT assumes the Born–Oppenheimer approximation, which states that the motion of the nuclei can be separated from that of the electrons. Thus

the electron are said to follow the nuclei adiabatically, that is they remain in their ground state as the atomic nuclei are moving. The approximation is valid due to the great difference in mass between the nuclei and the electrons. Forces may be obtained as minus the derivative of the energy, which according to the Hellmann–Feynmann theorem is the same as the derivative of the expectation value of the system Hamiltonian. Thus for each component of $\mathbf{R} := \{X, Y, Z\}$

$$F_X = -\frac{\partial E}{\partial X} = -\left\langle \psi \left| \frac{\partial \hat{H}}{\partial X} \right| \psi \right\rangle \tag{2.18}$$

Thus, during Born–Oppenheimer MD, the self-consistent DFT energy is calculated at each time-step, corresponding forces on ions are computed using 2.18, and the positions are updated according to the Verlet algorithm in equations 2.2.

2.1.3 Car-Parrinello Molecular Dynamics

Car and Parrinello proposed a molecular dynamics method which couples the ionic and electronic degrees of freedom at each time step, with both parts following classical dynamics [46]. In comparison with the previous MD method, where a full self-consistent calculation of the ground-state electronic orbitals is required at each step, the Car-Parrinello (CP) method lets the electronic wavefunctions evolve according to the equations of motion simultaneously with the ions. The method propagates ions of masses M_n positions $\mathbf{R}_n$, and electron wavefunctions ψ_k, according to the classical Lagrangian [42]

$$L(\{\psi_k\}, \{\mathbf{R}_n\}) = \mu \sum_k \dot{\psi}_k^2 + \sum_n \frac{M_n}{2} \dot{\mathbf{R}}_n^2 - E_{\text{tot}}[\{\psi_k\}, \{\mathbf{R}_n\}] + \sum_{kl} \Lambda_{kl} \left(\langle \psi_k | \psi_l \rangle - \delta_{k,l} \right) \tag{2.19}$$

In this equation μ is some small mass-like parameter, referred to as the fictitious electron mass, E_{tot} is calculated using the energy functional, and Λ_{kl} is the Lagrange multiplier matrix ensuring that the atomic orbitals ψ_k are orthonormal. From equation 2.19 we can write the following equations of motion:

$$\mu \ddot{\psi}_k = -\frac{\partial E_{\text{tot}}}{\partial \psi_k} + 2 \sum_l \Lambda_{kl} \psi_l(\mathbf{r}) \tag{2.20}$$

$$M_n \ddot{\mathbf{R}}_n = -\frac{\partial E_{\text{tot}}}{\partial \mathbf{R}_n} + \sum_{kl} \Lambda_{kl} \frac{\partial \langle \psi_k | \psi_l \rangle}{\partial \mathbf{R}_n} \tag{2.21}$$

Using these equations and the Verlet algorithm we propagate the electronic wavefunctions according to classical dynamics at the same time as the ions.

The important parameter here is μ. This is a mass parameter for the electronic degrees of freedom, which needs to be chosen small enough for the electrons to fol-

low this ionic motion adiabatically. The problem is that the smaller the chosen μ, the smaller the vibrational frequencies of the electronic degrees of freedom in the motion and so, the smaller the time step needs to be to get accurate trajectories. The choice of the fictitious mass μ is thus a compromise between adiabaticity and computation time. CP molecular dynamics is faster than the approach presented in the previous section because the actual ground state is not computed through a time consuming self-consistent cycle at every time step. However, the time step itself needs to be a lot smaller as the fictitious electronic motion needs to be accurately sampled. So, in most cases the CP technique proves to be equivalently as time-consuming as the ground state calculation approach.

The electron mass parameter μ is somewhat arbitrary, and results in fictitious electron dynamics which needs to be monitored throughout the simulation. If the electrons are not following ions adiabatically the fictitious kinetic energy of the electrons will rise because of an irreversible transfer of energy from ions to electrons, so watching this energy is a good way to control the simulation for loss of adiabaticity. Taking the total energy of the system H as the sum of the kinetic energies and the energy functional value, we write:

$$H = K_f + K_I + E[n] \tag{2.22}$$

where K_f denotes the fictitious electron kinetic energy, K_I the ionic kinetic energy, and $E[n]$ the energy due the instantaneous electron density. H has no physical meaning, because K_f is fictive, but it is conserved during the motion. However $H_I = K_I + E[n]$ should also be conserved, so we require $K_f \ll H_I$, that is we require that K_f does not rise to be comparable to the other energy values of the system. The monitoring of the CP MD simulation is thus done by checking that K_f does not rise too rapidly, and also that there is no significant drift in H, the constant of motion [47].

2.1.4 Applying an Electric Field via The Modern Theory of Polarisation

To perform AIMD calculations in an electric field it would seem that we only need to add an electric potential into the calculation of the force. However we have:

$$\vec{\mathcal{E}} = -\nabla V_{\mathcal{E}}(\mathbf{r}) \tag{2.23}$$

which means that to apply a constant electric field in a given direction we need a linear potential, which is not periodic. The problem is that in our framework the Hamiltonian needs to have the same periodicity as the system. We can therefore only apply saw-like potentials, which have the right periodicity but which represent unrealistic, discontinuous electric fields. The solution is to include an electric field term in the energy functional. We obtain the new energy functional [48]:

$$E^{\mathcal{E}}[\{\psi_k\}] = E[\{\psi_k\}] - \Omega\mathcal{E}P[\{\psi_k\}] \tag{2.24}$$

where Ω is the unit cell volume, and $P[\{\psi_k\}]$ refers to the polarisation in the direction of the field, as given by the modern theory of polarisation explained briefly below. The sole dependency on the electronic density is lost because the polarisation is calculated using a quantum phase of the wavefunction, requiring information which cannot be obtained from the density alone.

The macroscopic polarisation, also referred to as polarisation density $\mathbf{P}$, is a vector quantity which expresses the electric dipole moment per unit volume of a material. This notion is useful to describe the response of materials to an electric field, such as inducing a switch of polarisation in ferroelectric materials. The microscopic description of polarisation is not as obvious. The historical Clausius-Mossotti model defines the macroscopic polarisation $\mathbf{P}_{\mathrm{CM}}$ in a periodic solid as the sum of the dipole moments in a given cell divided by the volume of the cell. This definition implies that we can use the electronic density $n(\mathbf{r})$ to find areas of more positive or more negative charge densities to define dipole moments within a unit cell. In reality this is problematic because even if there are well defined areas of higher and lower charge density in a material, the choice of the unit cell is arbitrary and can lead to different values of $\mathbf{P}$. This point is illustrated in figure 2.1.

The modern theory of polarisation is a framework which provides a consistent microscopic description of polarisation [49]. In this theory, the polarisation is not described in terms of charge density but in terms of charge flow, through a quantum phase of the wavefunction called the Berry phase. It can be noted that

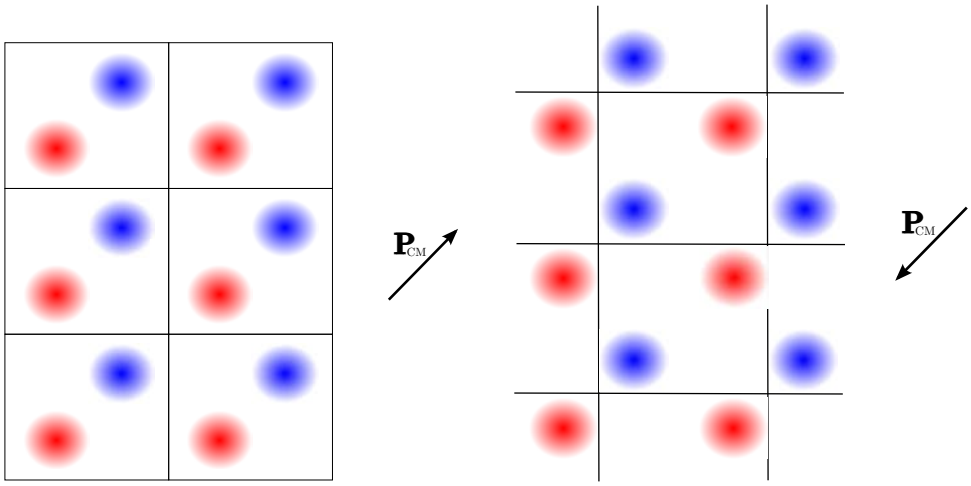

Figure 2.1: *Illustration explaining why the Clausius-Mossetti model is misleading. We see that for the same periodic electron density we can arrive at different polarisations. The red spots represent zones of low electron density and the blue spots represent higher electron density. In real systems the electronic density is continuous making this definition of polarisation impossible to apply.*

experimentally, the polarisation is almost never measured directly but arrived at by measuring values which are derivatives of the polarisation, such as the permittivity or the piezoelectric tensor. For ferroelectric materials, the value measured experimentally is $2\mathbf{P}$, the change in polarisation during the switch between $-\mathbf{P}$ and $\mathbf{P}$. The polarisation is then deduced by symmetry. In this respect the modern theory of polarisation draws a parallel between experiment and microscopic theory. The main idea is that the meaningful value is not the 'absolute' macroscopic polarisation $\mathbf{P}$, but the *change* in polarisation $\Delta\mathbf{P}$ occurring during the adiabatic turning on of an external electric field. The change in polarisation is defined in terms of the current across a unit cell induced by the switching on of a field:

$$\Delta\mathbf{P} = \int \mathrm{d}t \, \frac{1}{V_{\mathrm{cell}}} \int_{\mathrm{cell}} \mathrm{d}\mathbf{r} \, \mathbf{j}(\mathbf{r}, t) \tag{2.25}$$

Where the integral is over one cell volume, and $\mathbf{j}(\mathbf{r}, t)$ is the charge flow across the cell. In a quantum mechanical description of the electronic system, information about current flow is retained in the phase of the wavefunction. This information however is not present in the electronic density $n(\mathbf{r})$ which only depends on the modulus of the wavefunction.

The Berry phase formalism [50] uses the Bloch states

$$\psi_{n\mathbf{q}}(\mathbf{r}) = e^{i\mathbf{q}\cdot\mathbf{r}} u_{n\mathbf{q}}(\mathbf{r}) \tag{2.26}$$

which are eigenfunctions of the one electron Hamiltonian

$$H = \frac{\hat{\mathbf{p}}}{2m} + V(\mathbf{r}) \tag{2.27}$$

This Hamiltonian has a reciprocal space equivalent, with eigenfunctions in $\mathbf{q}$ space $|u_{n\mathbf{q}}\rangle$:

$$H(\mathbf{q}) = e^{-i\mathbf{q}\cdot\mathbf{r}} H e^{i\mathbf{q}\cdot\mathbf{r}} = \frac{(\hat{\mathbf{p}} + \hbar\hat{\mathbf{q}})^2}{2m} + V(\mathbf{r}) \tag{2.28}$$

We introduce the vector known as 'Berry connection' or 'gauge potential'

$$\mathbf{A}(\mathbf{q}) = i\langle u_{n\mathbf{q}}|\nabla_{\mathbf{q}}|u_{n\mathbf{q}}\rangle \tag{2.29}$$

whose integral over a closed manifold, for example the Brillouin zone, is called the Berry phase. This phase shift is inaccessible from the electronic density alone. Applying perturbation theory, during the adiabatic switching on of the field the wavefunctions corrected to first order are given by:

$$|u_{n\mathbf{q}}\rangle - i\hbar \sum_{n' \neq n} \frac{|u_{n'}\rangle\langle u_{n'}|\partial u_n/\partial t\rangle}{E_n - E_{n'}} \tag{2.30}$$

Now applying the first order correction and the quantum mechanical definition of current, equation 2.25 becomes

$$\frac{\partial \mathbf{P}}{\partial t} = \mathbf{j} = e \sum_n \frac{\mathbf{q}}{(2\pi)^3} \int_{\mathrm{BZ}} i \left\{ \left\langle \frac{\partial u_n}{\partial \mathbf{q}} \middle| \frac{\partial u_n}{\partial t} \right\rangle - \left\langle \frac{\partial u_n}{\partial t} \middle| \frac{\partial u_n}{\partial \mathbf{q}} \right\rangle \right\} \tag{2.31}$$

(full derivation in reference [50]). We integrate over time to get the electronic contribution to the polarisation, and add the ionic contribution:

$$\mathbf{P} = \mathbf{P}_{\mathrm{el}} + \mathbf{P}_{\mathrm{ion}} \tag{2.32}$$

$$= \frac{e}{(2\pi)^3} \mathrm{Im} \sum_n \int \mathrm{d}\mathbf{q} \langle u_{n\mathbf{q}}|\nabla_{\mathbf{q}}|u_{n\mathbf{q}}\rangle + \frac{e}{\Omega} \sum_i Z_i^{\mathrm{ion}} \mathbf{R}_i \tag{2.33}$$

This gives the polarisation needed in the new functional 2.24. Computing the Berry phase requires the wavefunctions and so the energy is no longer a functional of the density alone, which increases computation time. Typically when applying a field in this way using a fully converged ground state calculation at each time step, as in Born-Oppenheimer MD, the computation time increased by about an order of magnitude due to the functional having to be evaluated at each iteration of the self-consistent cycle in order to be minimised. Using Car-Parrinello MD, the time only increased about threefold.

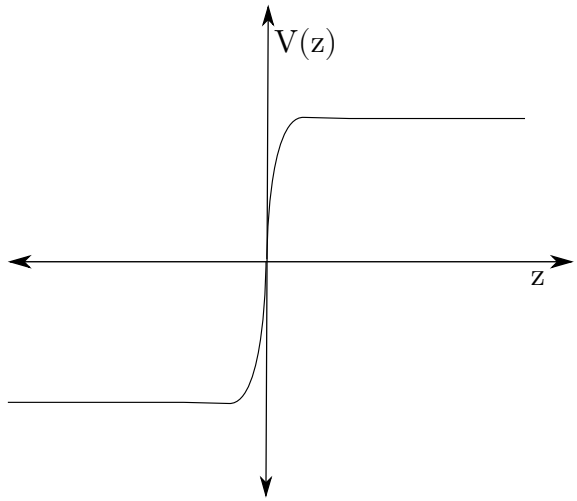

Figure 2.2: *Representation of the potential step at an interface.*

2.2 Accessing the Electric field

In a general context for any charge distribution, Poisson's equation holds, and more specifically in the 1D case for a charge distribution $\rho(z)$ we have:

$$\frac{\partial^2 V}{\partial z^2} = -4\pi\rho(z) \tag{2.34}$$

In atomic units, where $V(z)$ is the electrostatic potential.

We place ourselves in the case where there is an interface. We have a constant value of the potential at $-\infty$ and another constant value at $+\infty$ (eg: a potential barrier between two semiconductors, or a semiconductor/vacuum interface. See figure 2.2). We then have the condition:

$$\frac{\partial V}{\partial z}(-\infty) = \frac{\partial V}{\partial z}(\infty) = 0 \tag{2.35}$$

In this case we can give the corresponding expression for the 1D electrostatic potential (and check that its second derivative gives back equation 2.34):

$$V(z) = -2\pi \int_{-\infty}^{+\infty} \mathrm{d}z' \, |z - z'| \, \rho(z') \tag{2.36}$$

$$\frac{\partial V}{\partial z} = -2\pi \int_{-\infty}^{+\infty} \mathrm{d}z' \frac{\partial}{\partial z} |z - z'| \, \rho(z') \tag{2.37}$$

$$= -2\pi \int_{-\infty}^{+\infty} \mathrm{d}z' \left[\Theta(z - z') - \Theta(z' - z)\right] \rho(z') \tag{2.38}$$

$$= -2\pi \int_{-\infty}^{z} \mathrm{d}z' \rho(z') + 2\pi \int_{z}^{+\infty} \mathrm{d}z' \rho(z') \tag{2.39}$$

$$\frac{\partial^2 V}{\partial z^2} = -4\pi\rho(z) \tag{2.40}$$

Finally we can express the electric field in terms of the electrostatic potential and in terms of the charge:

$$E(z) = -\frac{\partial V}{\partial z} = 2\pi \int_{-\infty}^{z} \mathrm{d}z' \rho(z') - 2\pi \int_{z}^{+\infty} \mathrm{d}z' \rho(z') \tag{2.41}$$

2.2.1 Application to a model surface

To simulate an MgO surface, we use a supercell with slab geometry. The (100) direction is the z direction, and the slab is a stacking of 6 MgO layers followed by an equivalent distance of vacuum. During what follows we will look at the planar averages of the charge and electric field. For a physical quantity $f(x, y, z)$ the planar average is:

$$\bar{f}(z) = \frac{1}{\Omega_{\parallel}} \int_{\parallel} f(x, y, z) \mathrm{d}x \mathrm{d}y \tag{2.42}$$

Where $\Omega_{\parallel}$ is the surface area of the unit cell, and the integration is done along the directions parallel to the surface.

We first obtain the total charge along z. Available to us is the electron charge density $\rho_e(x, y, z)$ and the ionic potential $V_I(x, y, z) = \sum V_{\text{pseudo}}$. We can then plot $\bar{\rho}_e(z)$ the planar average of the electron density. We can define a 'pseudo' ionic charge:

$$\rho_I(x, y, z) = \nabla^2 V_I \tag{2.43}$$

and plot the planar average $\bar{\rho}_I(z)$. The electron and pseudo ionic charges are plotted in figure 2.3.

We define the macroscopic average of a physical value by filtering $\bar{f}(z)$ through a one-dimensional convolution [51]:

$$\bar{\bar{f}}(z) = \frac{1}{b} \int_{z-\frac{b}{2}}^{z+\frac{b}{2}} \bar{f}(z') \mathrm{d}z' \tag{2.44}$$

Where b corresponds to the periodicity in the z direction, in this case the spacing between planes which corresponds to the lattice parameter a. Using this we can obtain a flat value in the bulk and have a clear indication of where the interface lies. This is how we can relate the specific case to the general 1D picture presented above.

We can now define a total 'macroscopic' charge with which we will calculate the electric field. In figure 2.4 we can see the sum of the macroscopic electronic and pseudo-ionic charges. There is an excess of positive charge on the inner side of the interface and an excess of negative charge on the outer side. This is known

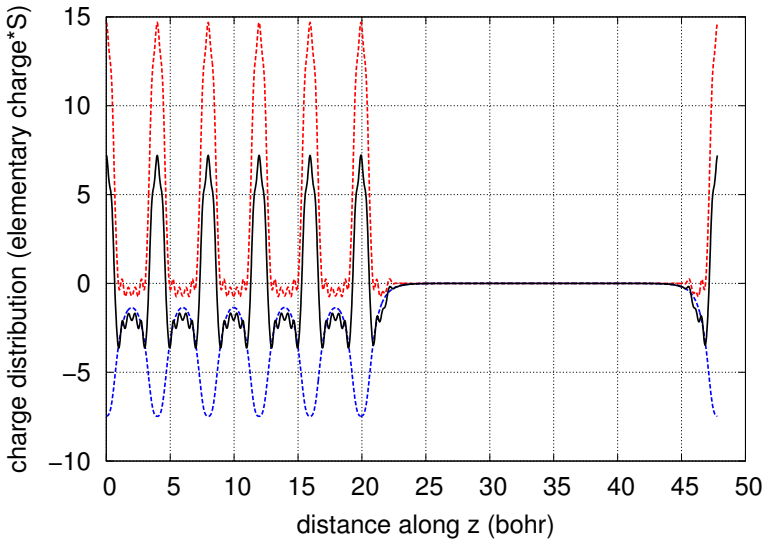

Figure 2.3: *Planar average of charges at the MgO(100)/vacuum interface. The red (blue) dotted line represents the planar average of the ionic charges, $\bar{\rho}_I(z)$ (electronic charges, $\bar{\rho}_e(z)$). The black line is the sum of the two, $\bar{\rho}(z)$, the total charge. There are six layers of MgO stacked along z, as can be seen in the profile, with the surface layer being at 20 Bohr. This lateral profile is dominated by the ocillations in the bulk, and properties of the surface layer are difficult to see.*

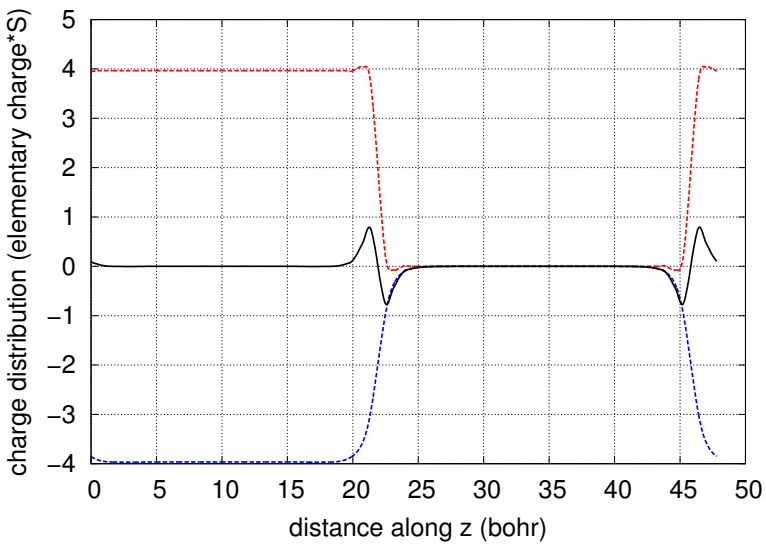

Figure 2.4: *Macroscopic average of charges at the MgO(100)/vacuum interface. The red (blue) dotted line represents the macroscopic average of the ionic charges, $\bar{\bar{\rho}}_I(z)$ (electronic charges, $\bar{\bar{\rho}}_e(z)$). The black line is the sum of the two, $\bar{\bar{\rho}}(z)$, the total macroscopic charge. There are six layers of MgO stacked along z, with the surface layer being at 20 Bohr. This lateral profile no longer displays the ocillations in the bulk, so that the surface dipole becomes apparent.*

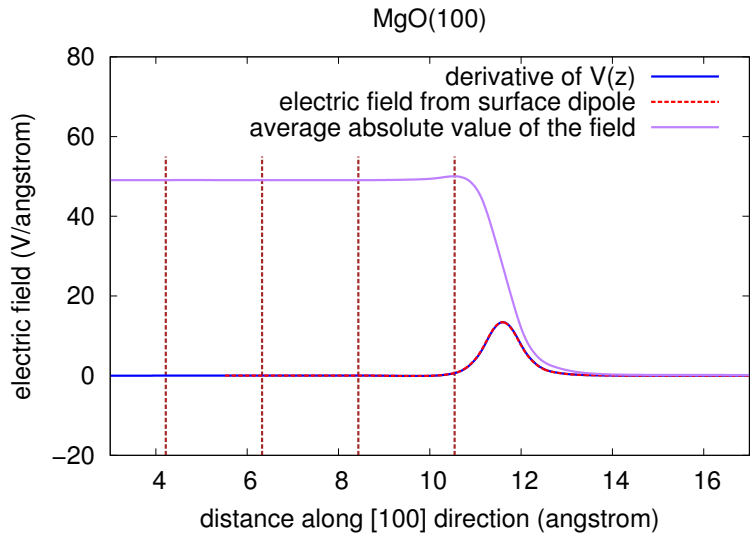

Figure 2.5: *Electric field at the MgO(100)/vacuum interface. The layers of MgO are reprensented by brown lines. The purple line is the macroscopic average of the absolute value of the electric field. The blue line is the derivative of the macroscopic electrostatic potential, and the red line is the integral of the macroscopic charge distribution. As expected, these two profiles are equal.*

as the surface dipole. We can now numerically calculate the value of the electric field in the z direction using equation 2.41, replacing the $\pm\infty$ limits with z values around the interface in which the average charge is zero. The result is shown in figure 2.5, converted in units of V/Å . In this approach we have made apparent the surface dipole and thus the intuitive origin of this electric field.

In practice the field can also be obtained by taking the negative gradient of the electrostatic potential:

$$\mathbf{E}(\mathbf{r}) = -\nabla V(\mathbf{r}) \tag{2.45}$$

The electric field is a vector field, with the three components:

$$E_x = -\frac{\partial V}{\partial x}, \quad E_y = -\frac{\partial V}{\partial y}, \quad E_z = -\frac{\partial V}{\partial z} \tag{2.46}$$

Here we can note that the derivative commutes with the aforementioned planar and macroscopic averaging techniques. Therefore, in practice, we can apply the macroscopic average on the electrostatic potential and then get the z component of the field, or obtain the full vector field and then apply the averages on the z component.

In this work, z component profiles are presented in the surface normal direction, and profiles of the absolute value of the field are also presented. Figure 2.5 shows that at the surface vicinity the electric field is largely in the surface normal

direction. Fields close to atoms are extremely high, and often not comparable to fields applied to a system for example in electrochemical setups. The profile at the electric double layer for example, has rarely been presented, and the question of coarse graining to obtain macroscopic electric field profiles from microscopic charge distribution is still not completely solved.

2.3 Enhanced Sampling Techniques

The AIMD framework requires a large amount of computational resources as a trade-off for accuracy in the description of polarisation and making and breaking of bonds in complex environments, such as the oxide/water interface which is studied in this work. However this means that within the available computational resources today, systems studied in this framework may contain at most several hundreds of atoms, with trajectory lengths of several tens of pico-seconds. These small sizes and time-scales make it impossible to correctly sample the thermodynamics of a system, without resorting to some clever tricks known globally as enhanced sampling techniques. Many of these techniques are available in the literature, we focus here only on the ones used in this work – metadynamics and umbrella sampling. The choice of the reaction coordinate is also important, as is outlined below.

2.3.1 Parametrisation of the Free Energy Landscape

A free energy landscape can be described in one-dimension if the reaction going from state A to state B has a clear reaction coordinate. The reaction coordinate can be defined in terms of the positions of the atoms in the system; it could be a physical distance between atoms, an angle, torsional angle, or any combination of these things. However such a reaction coordinate is not always obvious to find, and in complex cases can lead to restricting the system to follow a strict path in configuration space, which may not necessarily reflect the path of lowest free energy.

Path collective variables (pathCV) are a way to parametrise the free energy landscape according to configurations along a reaction path, and using these variables we can also define a second reaction coordinate in which the system may stray from the path. If we call the set of coordinates describing a state in the transition $\mathbf{R}$, the vector describing the path is a set of $\mathbf{R}_k$ where the first 'frame' $\mathbf{R}_1 = \mathbf{R}_A$ is the initial state and $\mathbf{R}_N = \mathbf{R}_B$ is the final state. From this definition we can introduce variables s and z [52]:

$$s(\mathbf{R}) = \frac{1}{P-1} \frac{\sum_{k=1}^{N} (k-1) e^{-\lambda \left(\mathbf{R}-\mathbf{R}_k\right)^2}}{\sum_{k=1}^{N} e^{-\lambda \left(\mathbf{R}-\mathbf{R}_k\right)^2}} \tag{2.47}$$

$$z(\mathbf{R}) = -\frac{1}{\lambda} \log\left(\sum_{k=1}^{N} e^{-\lambda \left(\mathbf{R}-\mathbf{R}_k\right)^2} \right) \tag{2.48}$$

where $s(\mathbf{R})$ is the progress the system has made in the direction of the path and $z(\mathbf{R})$ can be seen as the distance strayed from the path. Using the variables s and z, we can represent the high dimensional ensemble of atomic configurations $\mathbf{R}(t)$ in two dimensions. $(\mathbf{R} - \mathbf{R}_k)^2$ is effectively a mean squared displacement, and λ is chosen such that it is comparable to the inverse of this (see ref. [52] for more details). Other metrics can also be used in place of the mean squared displacement in the definition of s and z. In the present work the metric used is the same as in [53], and defined in terms of coordination numbers. Thus for atomic configurations $\mathbf{R}_1, \mathbf{R}_2, \ldots, \mathbf{R}_N$ defining the reaction path, we define a distance between the atomic configuration at a given time $\mathbf{R}(t)$ and the atomic configuration on the kth frame $\mathbf{R}_k$ as:

$$D(\mathbf{R}(t), \mathbf{R}_k) = \sum_{I,S} [C_{I,S}(t) - C^k_{I,S}]^2 \tag{2.49}$$

with $C_{I,S}(t)$ ($C^k_{I,S}$) referring to the coordination number between atom I and all atoms of type S at time t (at frame k). $C_{I,S}$ is the following switching function:

$$C_{I,S} = \sum_{J \in S} \left[1 - \left(\frac{R_{IJ}(t)}{R^0_{SS'}} \right)^N \right] \Big/ \left[1 - \left(\frac{R_{IJ}(t)}{R^0_{SS'}} \right)^M \right] \tag{2.50}$$

where R_{IJ} is the distance between atoms I and J, $R^0_{SS'}$ refers to the characteristic bond length between atoms of type S and S'. Full details of the parameters are given in the appendix. Figure 2.6 shows an example where $N = 2$ (there are two frames) with frame 1 referring to formamide and frame 2 referring to carbon monoxide and ammonia. The nearest integer coordination numbers are given in the figure to illustrate how this definition of path variables can be applied.

Using D we can define the two orthogonal variables s and z:

$$s(t) = \frac{\sum_{k=1}^{N} k e^{-\lambda D\left(\mathbf{R}(t), \mathbf{R}_k\right)}}{\sum_{k=1}^{N} e^{-\lambda D\left(\mathbf{R}(t), \mathbf{R}_k\right)}} \tag{2.51}$$

$$z(t) = -\frac{1}{\lambda} \log\left(\sum_{k=1}^{N} e^{-\lambda D\left(\mathbf{R}(t), \mathbf{R}_k\right)} \right) \tag{2.52}$$

Describing the system in this way means we can efficiently sample the configuration space using enhanced sampling techniques such as metadynamics (metaD) and umbrella sampling (US) which are briefly explained below. The use of this metric enables us to map separate simulations to the same configuration space – for example, the near surface simulation can be directly compared to the bulk simulation, or the bulk to the bulk with an external electric field, as will be demonstrated in chapter 4.

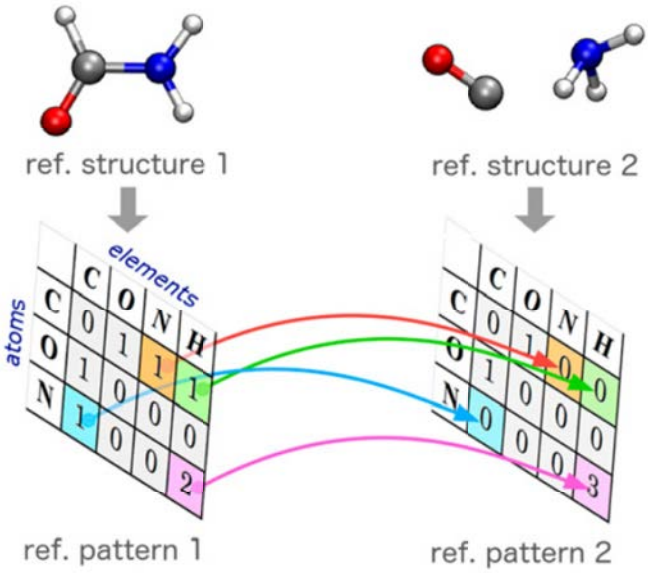

Figure 2.6: *Illustration of the type of collective variables used in this work. Figure from [53] where the reaction studied is the decomposition of formamide to caron monoxide and ammonia. The matrix element which change to define one structure and another are clearly shown.*

2.3.2 Metadynamics

Metadynamics was introduced by Laio and Parinello [54], as a means to "escape the free energy minima" (to quote the article's title). The method not only enables a molecular dynamics simulation to be accelerated in a certain direction of the free energy landscape, but also finds the most likely reaction pathways according to the chosen reaction coordinate, and returns the free energy landscape itself as a result.

We call the set of coordinates describing a system $\mathbf{R}$, and the corresponding coordinate in the collective variable $s(\mathbf{R})$. The probability distribution can be defined as the following:

$$P(s) = \frac{e^{-\beta F(s)}}{\int e^{-\beta F(s)} \mathrm{d}s} \tag{2.53}$$

where $\beta = \frac{1}{k_B T}$ with T the temperature of the simulation and $F(s)$ referring to the free energy. In an ideally infinite equilibrium simulation we have ergodicity and $P(s)$ can simply be obtained from a histogram of the system's evolution along s. We can then write the free energy $F(s)$

$$F(s) = -k_B T \ln P(s) \tag{2.54}$$

We can also write the free energy

$$F(s) = \frac{1}{\beta} \ln\left(\int e^{-\beta V(\mathbf{R})} \delta(s - s(\mathbf{R})) \mathrm{d}\mathbf{R} \right) \tag{2.55}$$

with $V(\mathbf{R})$ the potential.

In the real case however, and especially for AIMD, the simulation is not long enough for a barrier to be crossed even once and the system would remain 'stuck' in the energy minimum where the simulation was started. We thus add a time dependent potential $F_G(s, t)$ which serves to 'push' the system out of its minima, and which, if properly constructed, will provide a good estimate of the underlying free energy landscape, i.e.

$$\lim_{t \to \infty} F_G(s, t) \approx F(s) \tag{2.56}$$

This property is the main justification for metadynamics. The method proposed by Laio and Parinello consists of updating $F_G(s, t)$ by adding Gaussian functions at regular intervals in t. Thus we have

$$F_G(s, t) = -w \sum_{t' \leq t} \exp\left(- \frac{|s - s_{t'}|^2}{2\sigma^2} \right) \tag{2.57}$$

where w is the height of the Gaussian and σ is the width. We see that the current free energy term at a time t is a sum of the previous Gaussians deposited, each centered around the system's collective variable coordinate at times t'. This results in a constrained dynamics, where extra forces are added to the system and effectively the underlying free energy landscape is 'filled up', as one might fill a cavity with sand or with water. These forces are such that the system is less likely to visit a certain part of the landscape again after it has already been there, and eventually the system is pushed out of its initial minimum. Metadynamics is always best explained visually, and the 'filling up' of the landscape is illustrated in figure 2.7.

However, metadynamics is not perfect in every situation, and for this work it proved to exhibit some convergence issues, namely that the 'flatness' displayed in figure 2.7 was never achieved. A variant of metadynamics called well-tempered metadynamics was tried, in which the gaussians added with equation 2.57 are weighted according to how much bias has already been added at a certain point of the free energy space. This means adding smaller and smaller gaussians which should result in some form of convergence. However, maybe due to the complex collective variables, adequate convergence could still not be determined to the level of accuracy required for this work, and the umbrella sampling method needed to

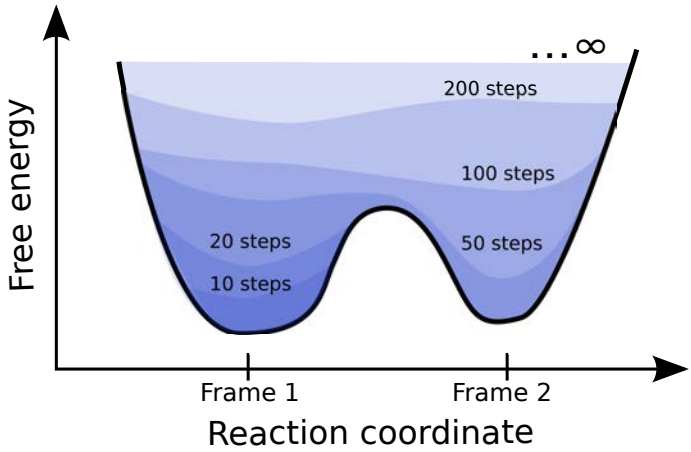

Figure 2.7: *Illustration of metadynamics. The free energy lanscape is gradually filled up, and can be obtained from the accumulation of gaussian biases called 'hills'.*

be used to attain the desired precision in the free energy landscape.

2.3.3 Umbrella Sampling

Umbrella sampling (US) consists of conducting a series of constrained dynamics centered along the reaction pathway in the free energy landscapes. As mentioned before, the histogram of the dynamics is directly related to the probability of presence, which can in turn give the free energy landscape, however in a short simulation the system may never cross a barrier and explore the total configuration space. Umbrella sampling consists of carrying out a constrained dynamics run in which the system is more likely to visit those regions of the space which are higher in free energy. We can constrain the system with the variables described in section 2.3.1, for example. The "umbrellas" are so called because often they are quadratic biasing potentials in configuration space, $V(s, z)$, described in this way:

$$V_i(s, z) = \kappa_{s,i}(s - s_i)^2 + \kappa_{z,i}(z - z_i)^2 \tag{2.58}$$

The index i refers to the ith umbrella, and the parameters $\kappa_{s,i}$ and $\kappa_{z,i}$ can be chosen to constrain the dynamics more or less around the point (s_i, z_i). An illustration of such an umbrella sampling run compared to an unbiased run is given in figure 2.8. For each US run the resulting histograms can be weighted by the weighting function:

$$w_i(s, z) = e^{-\beta V_i(s,z)} \tag{2.59}$$

to obtain corresponding local free energy surfaces (FES). However each FES obtained in this way has an arbitrary energy shift, which needs to be taken into account when we want to combine several US runs. Thus it is necessary to have overlap between adjacent US runs to be able to combine them. The weighted

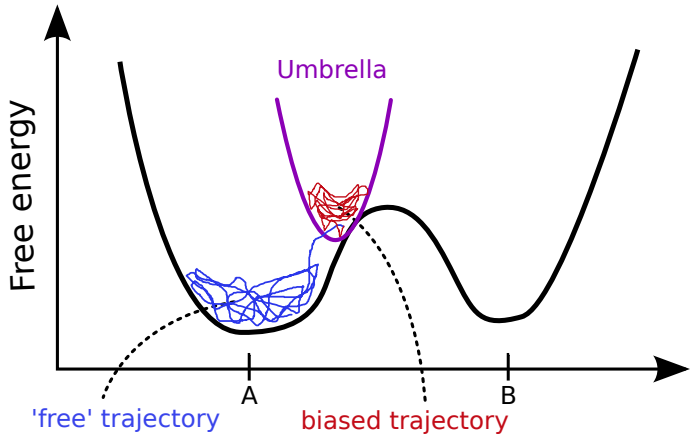

Figure 2.8: *Illustration of an umbrella sampling run (red trajectory) compared to an unbiased run (blue trajectory). Both trajectories have the same starting point, however in the unbiased case the system prefers to stay near the free energy minimum. Adding the umbrella enables us to sample which are less likely to be reached in a 'free' run.*

histogram analysis method (WHAM) is an efficient algorithm used to combine the partially overlapping histograms from US runs. Full details can be found in reference [55], and a working code used to perform WHAM can be downloaded at [56]. For this work a homemade code was used, which was tested against [56] in the quadratic umbrellas case, but which includes the possibility to add a linear term to the quadratic potential, and indeed to include any discrete biasing potential, such as for example an existing estimate for a free energy landscape as can be obtained from the "hills" in the metadynamics run. The new biasing potential thus combines the umbrella described by equation 2.58 and any other time independent biasing potential we may want to add. We will call this new biasing potential $V_{i,\text{bias}(s,z)}$ for each umbrella i. The WHAM algorithm consists in solving self-consistently for the unbiased probability of presence histograms $P(s,z)$ and the free energy shifts $F_i(s,z)$ [31]:

$$P(s,z) = \frac{\sum_{i=1}^{M} n_i(s,z)}{\sum_{i=1}^{M} n_i(s,z)\, e^{\beta\left(F_i(s,z)-V_{i,\text{bias}}\right)}} \tag{2.60}$$

$$F_i(s,z) = -k_B T \ln\left(\sum_{s,z\ \text{bins}} P(s,z)\, e^{-\beta V_{i,\text{bias}}(s,z)}\right) \tag{2.61}$$

In practice, the equations are iterated until convergence is reached.

Chapter 3

The Electric Field at the Surface of MgO

3.1 Introduction and Context

The impressive amount of works dedicated to the interfaces between water and oxide surfaces is motivated by their relevance to many different areas [57]: environmental sciences, electrochemistry [58, 59], catalysis and biochemistry [60]. Oxide surfaces in pre-biotic chemistry are of importance as these kind of mineral surfaces were abundant on the early earth and could have favoured certain reactions. Among other things, oxide surfaces are particularly interesting in their interaction with water. From previous works, it appears that one or more water layers at the interface have different static and dynamical properties from bulk water, although the thickness of such a region depends crucially on the surface structure and charge, and on the presence of dissolved ions. Such complexity calls for settled models of prototypical water/oxide interfaces.

Magnesium oxide (MgO) is a good candidate for this study because MgO shows a simple atomic and electronic structure that is well established in dry conditions, both theoretically and experimentally [61]. Furthermore, it can be seen as a gateway mineral to more complex minerals which are undoubtedly relevant to prebiotic hypotheses, such as clay minerals. The behaviour at the MgO(001)/water interface however is not as well-known as in dry conditions. The shape of MgO crystallites changes from cubic to octahedral when they are exposed to water [62]. The dissolution process of MgO(001) is rather fast in acidic solutions and deeply modifies the surface morphology [63], in a process dominated by kinetics. In contrast, at low water coverage (up to a monolayer) and for time lapses of order of a few hours, water adsorption on MgO(001) is dominated by thermodynamics. The isolated H_2O molecule spontaneously dissociates on low-coordinated surface

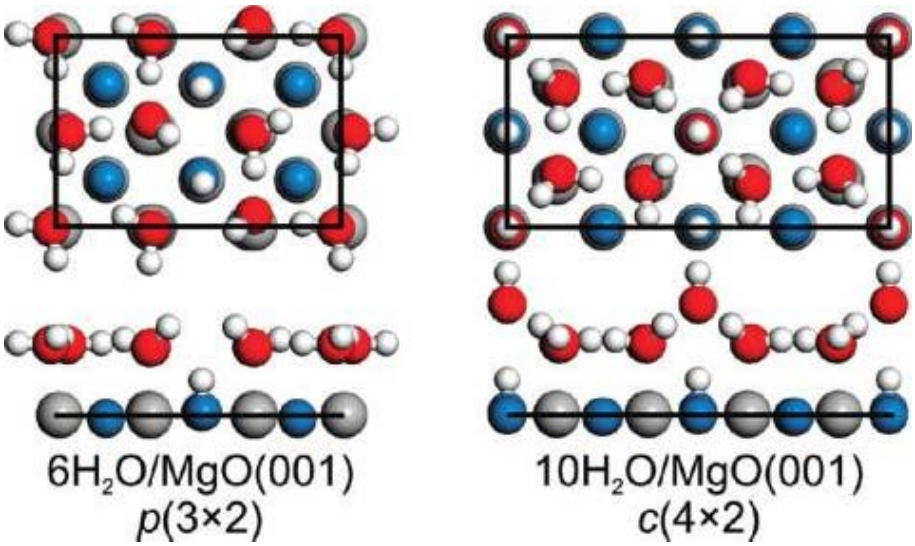

Figure 3.1: *Illustration of two theoretically stable configurations for the water monolayer on MgO(001). Taken from [68]. Oxygen atoms are blue for the surface atoms and red for the water molecule atoms, magnesium is in grey, and hydrogen atoms are in white. The p(3×2) configuration corresponds to UHV conditions under 185K while the c(4×2) configuration corresponds to 185-235K in UHV conditions. For this work the p(3×2) configuration was used as a starting point.*

sites, such as steps and kinks, but not on the flat (001) terrace [64], at odds with other alkali-earth oxides like CaO and BaO. However, hydrogen-bonded water ad-molecules on MgO(001) can dissociate, giving rise to characteristic hydroxyl groups consisting of a surface O and a proton coming from the ad-molecule [65]. This theoretical picture is corroborated by several experimental observations of the progressive onset of water dissociation as a function of the increasing water coverage [66, 67]. In the limit of a complete water monolayer on MgO(001), several ordered reconstructions were observed as a function of temperature [68] (see figure 3.1). All of them feature a variable proportion of hydroxyl groups resulting from the dissociation of some water ad-molecules, a picture that was originally proposed for the (2×3)-reconstructed water monolayer on MgO(001) on the basis of first-principles simulations [69]. The use of Density Functional Theory reconciled theory with experiments, as empirical force fields, most of which do not allow for water dissociation, were not able to provide an explanation for these reconstructions [70].

For water coverage above one monolayer, the experimental observations are rather scarce. Although many studies indicate that water organizes into very ordered layers close to the surface, a precise knowledge of the extent and the detailed characteristics of such organization as a function of the surface morphology is still fragmentary. The enthalpy of adsorption of water on MgO varied significantly from 1/2 to 3 monolayers, which was attributed to a stronger interaction

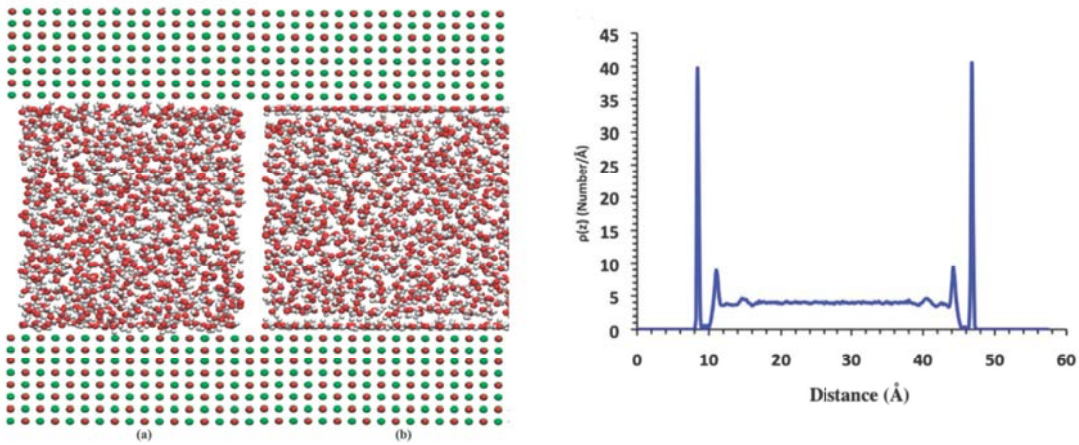

Figure 3.2: *Figures taken from [73]. Force-field simulation of the MgO(001)/water interface. The left panel shows snapshots of the starting configuration and during the dynamics. Oxygen atoms are red, magnesium atoms are green and hydrogen is white. The right panel shows the lateral density profile.*

between the first layer and the surface than between the next water ad-layers [71]. On the theoretical side, several simulations considered higher water coverage than one monolayer, but most of them used empirical models. The structural and dynamical properties of hydrated MgO nanoparticles were investigated through molecular dynamics using empirical interatomic potentials [72]. While highly ordered water layers appeared at the interface with the flat (001) surface, water coordination number, residence times and other properties were affected by the presence of corners and edges on surfaces with higher Miller indices. A significant ordering of water molecules, which are almost parallel to the surface in the two layers close to MgO(001), was found through molecular dynamics using a Born-Mayer-Buckingham interatomic potential for MgO and a flexible model for water [73] (see figure 3.2). Translational and orientational order parameters recovered their values for bulk water at about 3-4 layers from the surface. These features correlated with changes in the vibrational density of states of water. All the previous simulations were based on classical force fields and did not take into account water dissociation nor the influence it could have on the structure and the dynamical properties of the next water layers. An exception was provided by a first-principles study of the interface between ice and MgO(001) [74]. However, the authors considered only four H_2O layers on top of a $\sqrt{2} \times \sqrt{2}$ surface unit cell and conducted structural optimization at 0 K. The system dimension and the absence of dynamics hindered the comparison with experimental data as well as any discussion of the extent of water ordering.

As far as the surface electric field is concerned, Kelvin probe microscopy can be used to determine the surface work function with a lateral resolution of the order

of few nm [75]. Other local probes of the surface electric field are ad-molecules themselves, such as carbon monoxide. The shift of its vibrational frequency with respect to the gas phase is connected to the local charge and electric field of the cation sites on the surface [76]. However, these probes cannot easily be used at the water/oxide interface. Furthermore, there are very few studies that have attempted to calculate the electrostatic properties of a water/oxide interface in order to make the link between coarse-grained Electric Double Layer (EDL) theories and the reality of the local electric field. This is largely due to problems arising from interacting periodic replicas, which can be overcome when there is vacuum in the supercell [77], but become harder to work with when the supercell is 'filled' with water. For this reason studies reporting values of the electric field at an oxide interface require the surface to be neutral to minimise interactions between periodic replicas. Vlcek *et al.* [23] reported fields of about 6 V/Å at the SnO_2/water interface using static *ab-initio* calculations. D'Ercole *et al.* [78] provide electrostatic potential maps of defects at MgO and CaO surfaces, and the resulting field values are of several V/Å extending 2 Å to 3 Å from the position of the surface atom. In what follows electric field profiles are calculated *ab-initio* on various MgO interfaces.

In section 3.2 the electric field on top of bare MgO surfaces is calculated. In section 3.4, the study is extended to the MgO(001)/water interface, with full explicit solvent. The electric field at the interface is shown, as well as the influence of the MgO(001) surface on the water density profile and the extent of molecular dissociation from the surface layer into the bulk. Snapshots of each simulation box are given in figure 3.3 for clarity, and complete computational details are given in appendix A. Proton transfer at the surface is discussed in section 3.4.1 and a model for mimicking the surface electric field is suggested and tested in section 3.5.

3.2 Static Results on Bare MgO

3.2.1 MgO(001)

The electric field was obtained as outlined in section 2.2.1, and the corresponding potential and field plots are shown in figure 3.4, for the MgO(001)/vacuum interface. For clarity, the potential is shown as felt by the electrons – negative in the slab and positive in the vacuum. From analysis of the electrostatic potential we can calculate the work function, by calculating the vacuum level of the potential in a slab calculation, and taking the difference of this value with the highest occupied level in a reference bulk MgO calculation. In this case the work function

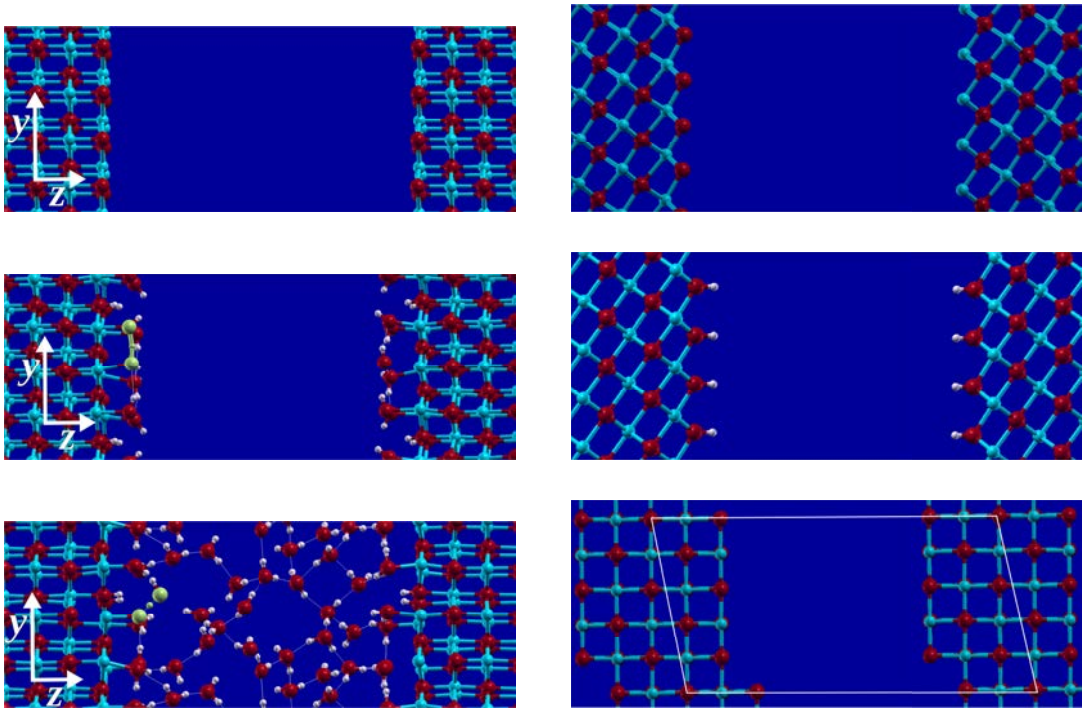

Figure 3.3: *Snapshots of the MgO interfaces studied in this chapter. Mg atoms are in blue, O in red, and H in white. The left column shows the 001 interfaces: MgO(001)/vacuum at the top, MgO(001)+1ML in the center, and MgO(001)/water on the bottom. When water is present an example of a proton transfer event is highlighted in green. The right column shows the MgO(111) bare and hydroxylated interfaces (respectively top and center), and the bottom left is the vicinal surface MgO(015). In this last image the unit cell outline is shown.*

was calculated to be 5.19 eV, which is within 5% of the reported experimental value for the work function of the MgO(001) surface, 4.94 eV [79], thus validating our value of the field and coarse-graining method. The broken symmetry in the surface normal direction results in a local asymmetry in the charge distribution at the interface – the electrons spill out into the vacuum and consequently there is an excess of positive charge just under the surface. This results in a strong surface dipole which is specific to each surface and contributes to the variation of the work function, and also results in an electric field [80].

As shown in figure 3.4, the electric field at the MgO(001)/vacuum interface is intense and permeates beyond the surface layer, although it is highly localised. There is a window extending to about 3 Å from the surface atoms in which the field is high enough to influence potential adsorbates, their structure and reactivity. Although this view differs from the classical view of the electric field on top of an ionic solid, this approach is consistent with both average electrostatic properties of the surface (such as the work function described above) and with local electrostatics at the Ångstrom scale. Figure 3.5 shows non-averaged profiles of the z component of the field directly on top of the surface Mg^{2+} and O^{2-} ions. Only points beyond the pseudo-potential cutoff radii are included. The behaviour is as expected, negative field on top of O and positive field on top of Mg, both decaying exponentially. However there is overall a clear imbalance towards the positive z-direction due to the surface dipole, which is reflected in the positive value of the sum. Figure 3.6 shows the z component $E_z(x, y, z_0)$, with z_0 at a height of 2 Å from the surface, which corresponds to the adsorption height for water. The plot again shows the influence of the surface ions, with nevertheless a field imbalance towards the positive z axis. In each of figures 3.4 to 3.6, the arrow shows the average value of the field at 2 Å above the surface. In all cases this value is between 0.5 V/Å and 1.5 V/Å. The difference in value is due to the averaging methods: in figure 3.4 the planar average and macroscopic average are both applied, for figure 3.5 the average profile directly above each type of ion is taken, without macroscopic average filtering, as for figure 3.6 the average is only taken from one slice of the electric field.

3.2.2 MgO(111) and MgO(015)

Figure 3.7 shows two other MgO surface profiles which were also calculated and coarse grained accordingly. The MgO(111) direction is polar as it consists of alternation layers of Mg^{2+} and O^{2-}, so it is unstable in reality. Thus in a calculation with periodic boundary condition a dipole is created across the supercell. Nonetheless, the electric field can be calculated at the surface and we can see that

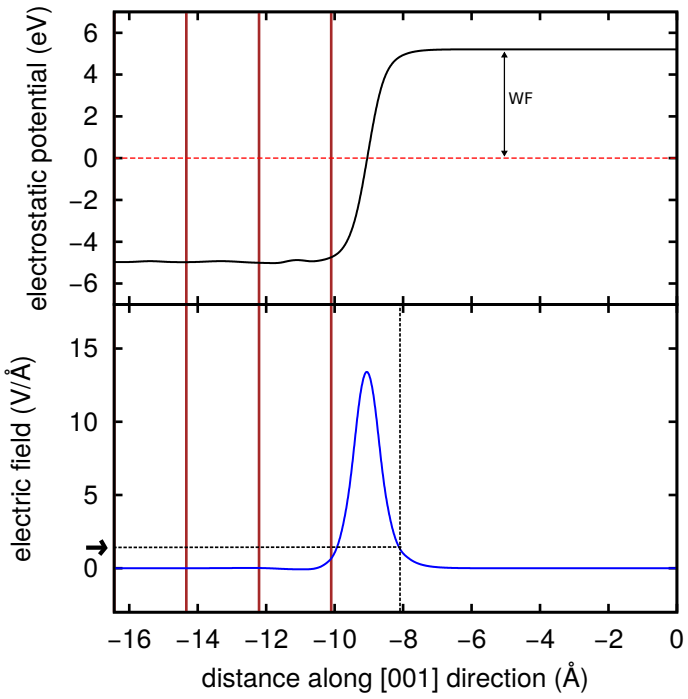

Figure 3.4: *The average z electrostatic potential as felt by the electrons, and the electric field profile at the surface of a bare MgO(001) surface. The MgO planes are represented by vertical lines, and the highest occupied level is set at zero, as shown by the red dotted line. The work function can be calculated as the difference between the potential in the vacuum and the highest occupied level in the bulk. The small arrow shows the electric field at 2 Åfrom the surface, which is a reasonable distance for water adsorption.*

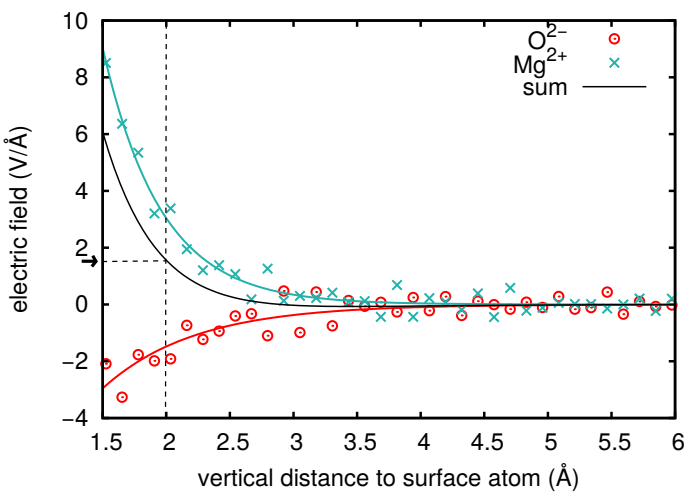

Figure 3.5: *z-component of the electric field along the [001] direction, directly on top of each type of surface ion. The lines are exponential fits to the data. The small arrow shows the electric field at 2 Åfrom the surface, which is a reasonable distance for water adsorption.*

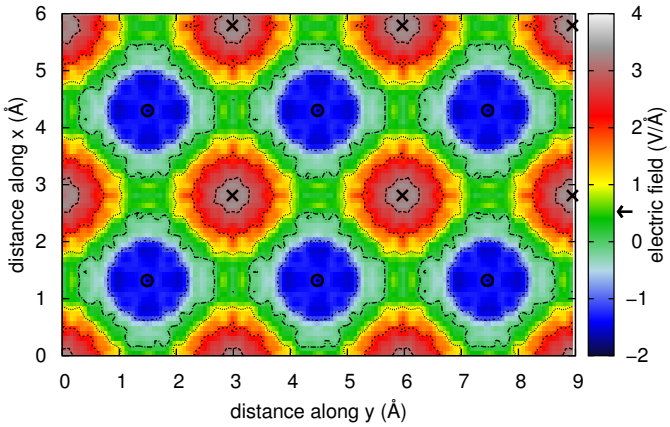

Figure 3.6: *z-component of the electric field in an xy plane at 2.0 Å from the surface layer of MgO(001). Lines are 1.0 V/Å apart. Underlying atomic postions are labeled with crosses for Mg and circles for O. The arrow on the colourbar indicates the average value of the z-component of the field in this plane.*

surprisingly, although it is very high locally, the field seems less intense than on the MgO(001) surface. We can include a dipole correction in the empty part of the cell which is calculated and applied self-consistently to cancel out the artificial dipole between the slabs. As seen in the figure, the field in the vacuum goes to zero as it should, apart from in the area where the dipole is added, which is an artifact of the simulation. There is an electric field however inside the slab, but this is a physically relevant field which would exist in such a thin film, and in the limit of an infinitely thick slab the field would go to zero. In reality surfaces in the MgO(111) direction are fully hydroxylated, or exhibit certain reconstructions, to maintain neutrality at the interface [81]. The potential and field profiles are also calculated in this case, as shown in figure 3.8.

The MgO(015) direction is an example of a vicinal surface, because it is in fact an average orientation when looking at a monoatomic (001) step with a width of 5 atoms (see bottom left panel of figure 3.3). Vicinal or stepped surfaces are though to have the highest reactivity, due to undercoordinated atoms being key sites for adsorption and dissociation of molecules [82], and have been shown to promote proton transfer [83]. The profiles are shown in figure 3.9. We notice that this is in fact a vicinal thin film, which is not something that would be stable in reality. The relaxation is very large, making the macroscopic averaging method difficult to apply correctly. Indeed, even if vicinal surfaces are good candidates for investigating the reactivity of real mineral surfaces, in this framework the computational cost would be too high to investigate one properly, as the unit cell would have to be quite large to get proper relaxation events and to simulate vicinal steps.

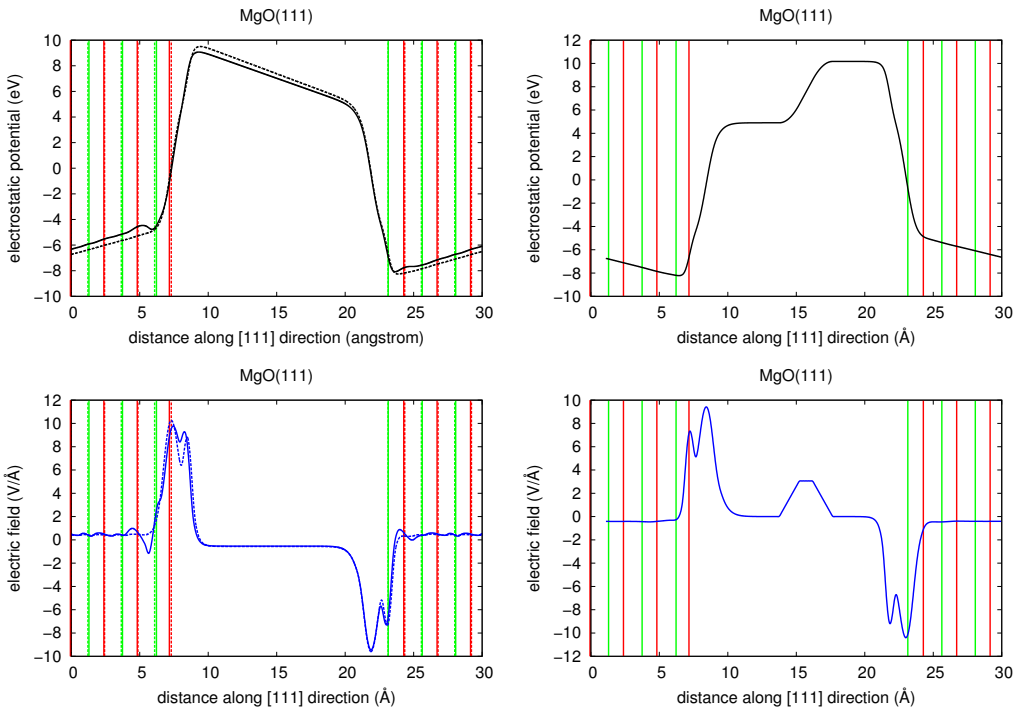

Figure 3.7: *Surface potential and field for MgO(111), in the case of the polar surface, with (right) and without (left) the dipole correction included. The vertical lines show Mg planes in green and O planes in red. The dotted lines show the rigid case, while the full lines show the relaxed case.*

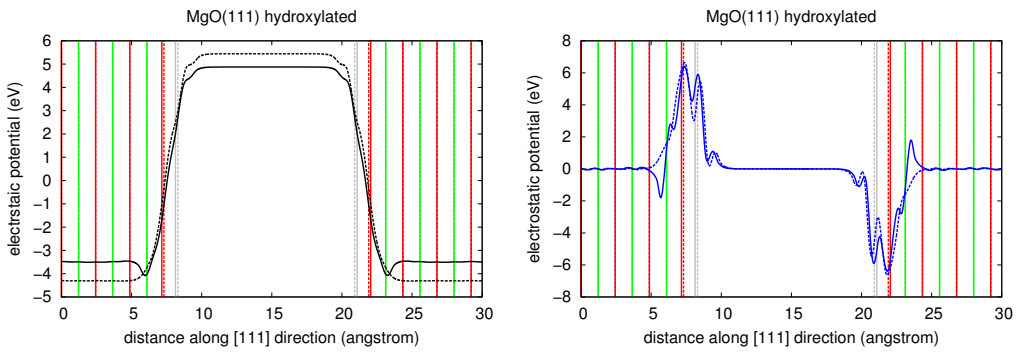

Figure 3.8: *Surface potential and field for MgO(111)+OH. The vertical lines show Mg planes in green and O planes in red, with the position of the adsorbed hydrogens shown in grey. The dotted lines show the rigid case, while the full lines show the relaxed case.*

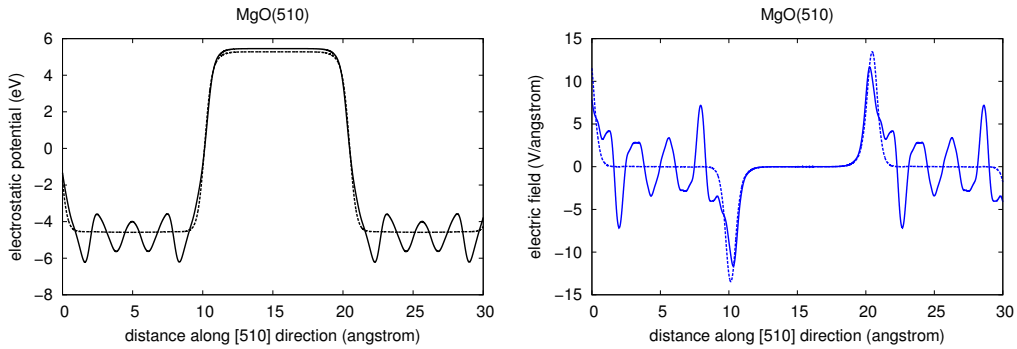

Figure 3.9: *Surface potential and field profiles for MgO(015). [015] planes are not shown, because they are too close together in the rigid case, and not well defined in the relaxed case. The dotted lines show the rigid profiles, while the full lines show the relaxed ones.*

The MgO(001) surface is experimentally flat and stable, as well as relatively simple to synthesise, and it exhibits the highest electric field of the three surfaces discussed above. Furthermore the behaviour of the first layer of water on MgO(001) has been characterised experimentally and in calculations, as outlined in the next section. Thus the natural choice was to investigate this first monolayer and to later observe the effect of the surface electric field on bulk water. The MgO(111) surface was not further investigated in this particular work but could be in the future, as could the similar brucite ($Mg(OH)_2$) surface. Indeed, recent work suggests that brucite appears at the surface of MgO crystals when in prolonged contact with water in certain conditions [84].

3.3 One monolayer of H_2O on MgO(001)

A monolayer of water (1ML) on MgO(001) is known to exist in several configurations depending on temperature and pressure [68]. For this study we chose to use the (2×3) reconstruction, which is stable between 185 K and 235 K in UHV conditions. In this reconstruction two out of six water molecules are dissociated as shown in figure 3.10. Initially the six water molecules were placed on top of MgO(001) and the positions allowed to relax. This resulted in spontaneous dissociation of two water molecules, with no energy barrier, in a configuration which was slightly different from the one in figure 3.10, but which exhibits the same number of OH groups on the surface and has the same symmetry (2×3 with a glide-plane). Nevertheless the configuration chosen is the one in figure 3.10 because it is accepted as the most stable configuration in the literature and because its energy was lowest. It is likely that several meta-stable analogues of this configuration exist, especially at non-zero temperatures, but due to the small size of the simulation box we chose for the following to remain with the most stable configu-

ration seen experimentally, even later on when several layers of water were added.

Figure 3.12 shows the electric field profile in the 1ML case. A first peak occurs within the adsorbed layer at the height of the adsorbed H^+ ions, and the second peak seems analogous to that in the bare surface case, *i.e.* intense, highly localised, but permeating a few Ångstrom beyond the surface. This peak is not as intense as in the bare surface case, which is a sign of screening by the H_2O molecules. Figure 3.13 shows the profile in the *xy* plane at a height of 4 Å from the surface, so about 2 Å from the adsorbed monolayer. At this height the underlying surface structure is not longer 'visible' in the field profile, and is instead screened by the less ordered adsorbed monolayer. We notice zones of positive and negative z fields corresponding to local water dipoles, as well as small scale oscillations which would probably become irrelevant when taking into account the dynamics of the system. Some of these oscillations are probably also noise in the electric field, which being a gradient is more numerically noisy than the potential or charge density. Such complexity calls for a coarse-grained description of the electric field, especially when we consider its effect on the structural and dynamical properties of the water above the first ad-layer.For the case of the water/MgO interface with more than a water ad-layer, we will thus retain the profile along z: $\bar{E}_z(z)$.

Figure 3.11 shows selected vibrations taken from a simulation of the adsorbed monolayer at 300 K. The vibration frequency spectra were obtained from taking a Fourier transform of the selected OH bond lengths as a function of time. A velocity autocorrelation function of all atoms could also be used to be able to directly compare such a spectrum to experimental data, however in this case the statistics were not sufficient to obtain discernible peaks, and it was preferable to isolate specific bonds and apply the autocorrelation function method to get specific vibration modes. Pre-selecting the characteristic OH bonds enables us to check which frequency contributions come from the surface OH groups. The blue peak corresponds to the OH in vacuum frequency at about 3900cm^{-1} and the green peak corresponds to the OHs which are directly adsorbed. We see that these are shifted towards smaller frequencies due to the higher coordination of the oxygen atoms, and the peak isn't as sharp because of the increased interaction with surrounding oxygen atoms.

3.4 Dynamic Results on the MgO/water Interface at 300K

Starting from the (2×3) monolayer reconstruction, 22 water molecules were added to the simulation cell to 'fill up' the vacuum between the slabs, resulting

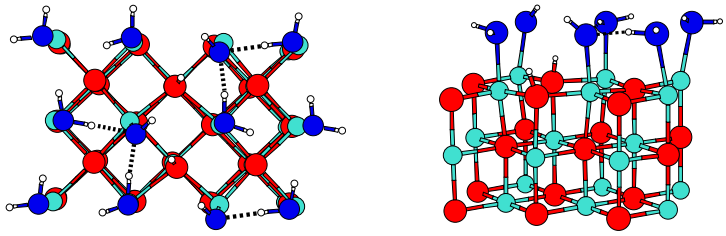

Figure 3.10: *Top view and side views of the unit surface of the (2×3) reconstruction of water on MgO. The Mg atoms are turquoise and the oxygen atoms belonging to the slab are red, while the oxygen atoms of the water monolayer are shown in blue.*

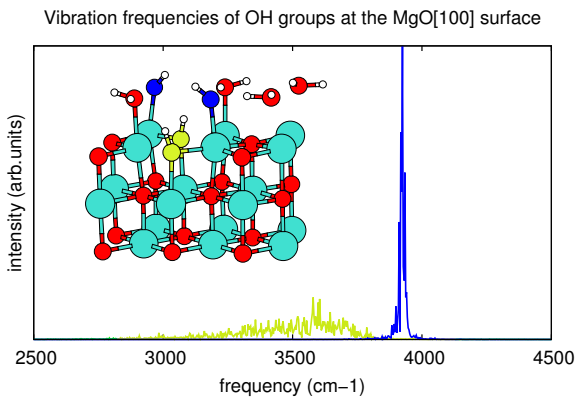

Figure 3.11: *Selected characteristic OH vibration modes for the single adsorbed monolayer of water on MgO(001). The peaks were obtained from a Fourier transform of the length as a function of time of the two types of OH bonds shown in blue and green on the figure.*

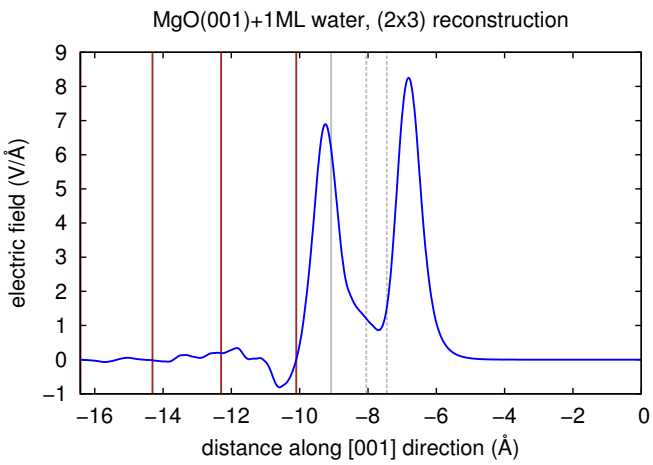

Figure 3.12: *Electric field profile of MgO(001) with a monolayer of water adsorbed, in a (2 × 3) reconstruction with partial dissociation. The vertical lines represent the MgO planes (brown), the average position of the adsorbed H^+ ions (solid grey) and the upper and lower bounds of the positions of the adsorbed water molecules and OH^- ions (dotted grey).*

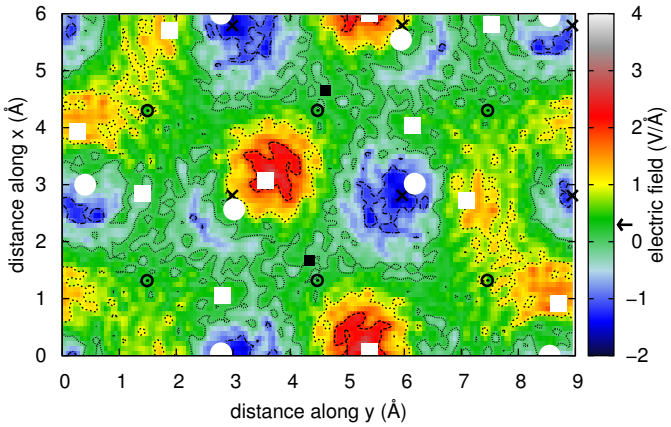

Figure 3.13: *z-component of the electric field in an xy plane at 4.0 Å from the surface layer of MgO(001). Lines are 1.0 V/Å apart. Underlying atomic postions are labeled with crosses for Mg and circles for O, and squares for H. White circles and squares show the positions of the oxygen and hydrogen atoms in the adsorbed layer. Black squares show the chemisorbed hydrogen atoms. The arrow on the colourbar indicates the average value of the z-component of the field in this plane.*

in a simulation consisting of 7 MgO layers in the [001] direction followed by 34 water molecules, 4 of which are dissociated on the surface (2 on each side). Before starting the simulation, the 22 water molecules were placed randomly in a box without MgO and AIMD was performed at 300 K for a few picoseconds. From this simulation, the initial positions were placed in between the MgO slabs, and the AIMD simulation was started with several subsequent rescaling steps of increasing temperature. Eventually the target temperature of 300 K was reached, and statistics were taken from after the simulation had had time to thermalize.

The electrostatic potential was saved every 30 timesteps, for analysis of the electric field throughout the simulation. The electric field profile was obtained as outlined in section 2.2, by averaging the derivative of the potential along x and y, and by filtering out the small range oscillations. However, although the $a/2$ averaging window is appropriate to smooth out oscillations within the MgO slab, the water in between the slabs does not exhibit $a/2$ periodicity along z. A second filter has been applied in order to smooth out oscillations due to liquid water. This filter was chosen based on the first peak in the oxygen-oxygen pair correlation function using a filter window of 2.5 Å. Other filters were also trialled and it was found that the profile is not very sensitive to the precise size of the window in the liquid, provided the filter window was between 2.3 Å 2.8 Å. The resulting profiles after planar averaging are shown in figure 3.14.

Figure 3.15 shows the electric field profile, density of water, and proton hopping events in 13 ps of simulation at 300 K. The field and density are averages

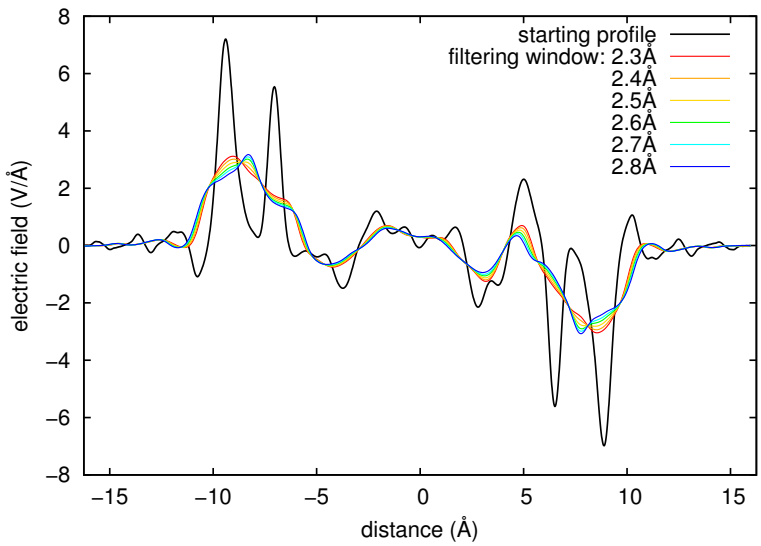

Figure 3.14: *Results of macroscopic averaging on the surface normal component of the electric field on the MgO(001)/water interface. In black, the planar average and macroscopic average with interlayer distance as the filter window. The colour lines are various applications of a second filter window based on characteristic water-water distances.*

taken over the time of the simulation, and the number of proton hops refers to the number of times an oxygen atom has exchanged one of its two nearest neighbour hydrogens. The figure shows that the electric field at the interface remains intense despite screening by the first layer and subsequent layers of water molecules. When comparing this profile to the 1ML profile in figure 3.12, there are two main differences: the loss of the double peak and the decrease of field intensity. These differences are both mostly due to the smoothing mentioned above, as without smoothing the z component of the field remains largely unchanged from the single monolayer case. Oscillations of the field in between the slabs are the result of local water dipoles and one would expect that over a long enough simulation or for a large enough box the field in the water far away from the surface would average to zero. The simulation is on small time and length scales which does not give access to the macroscopic values in bulk water; however when the oxygen-oxygen pair correlation function is calculated (see figure 3.16), we can say that water beyond the first layer is 'bulk-like' in that the O-O distances remain very similar to those in the bulk water reference.

The second graph in figure 3.15 shows oxygen atom and hydrogen atom presence along z. The oxygen atoms belonging to the MgO slab have been omitted for clarity. The first peak of hydrogen presence occurs just above the surface and corresponds to the hydrogen atoms adsorbed directly on the surface. These remain close to their initial positions throughout the simulation and do not re-associate

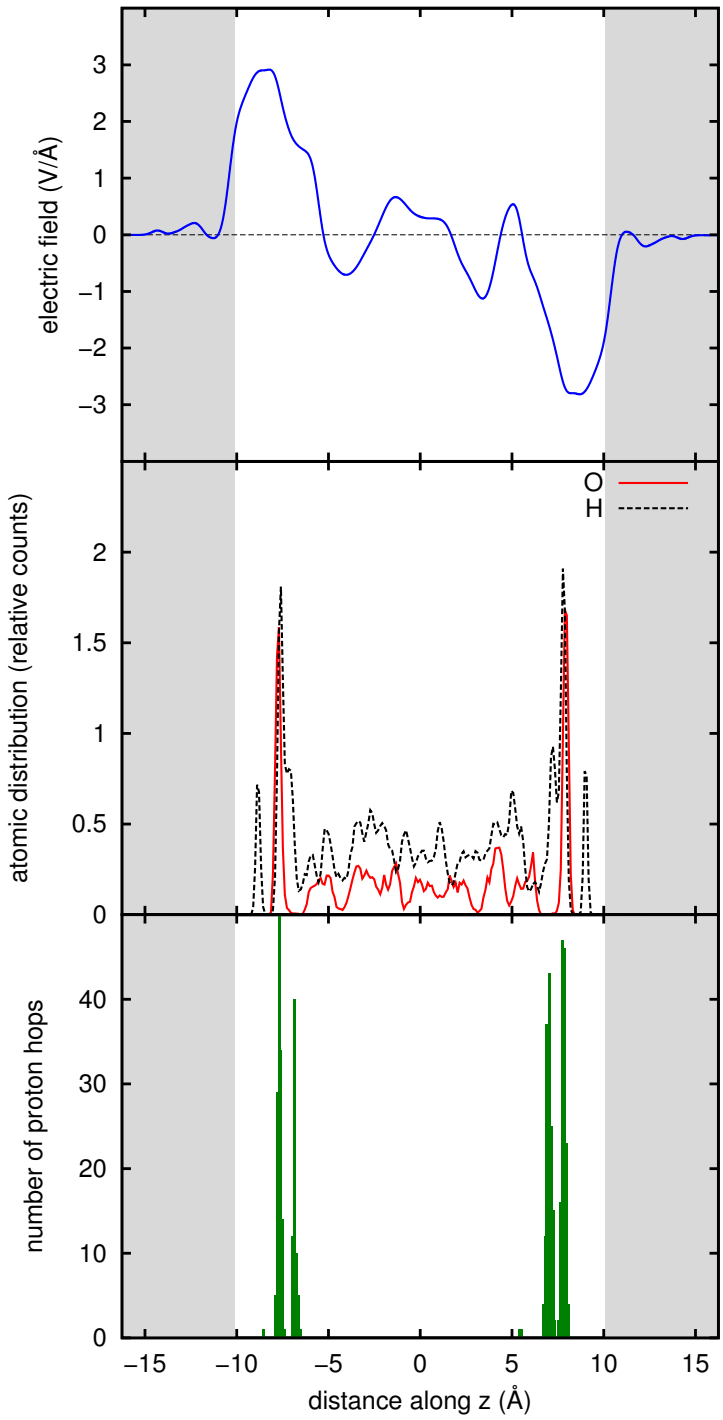

Figure 3.15: *The average electric field profile (blue), atomic distribution porfiles (red and black) and proton hop counts (green) in the simulation box. Shaded areas correspond to the position of the MgO slabs, to clearly show the position of the interfaces, at* $\pm z_s$ *(*z_s*=10.1Å).*

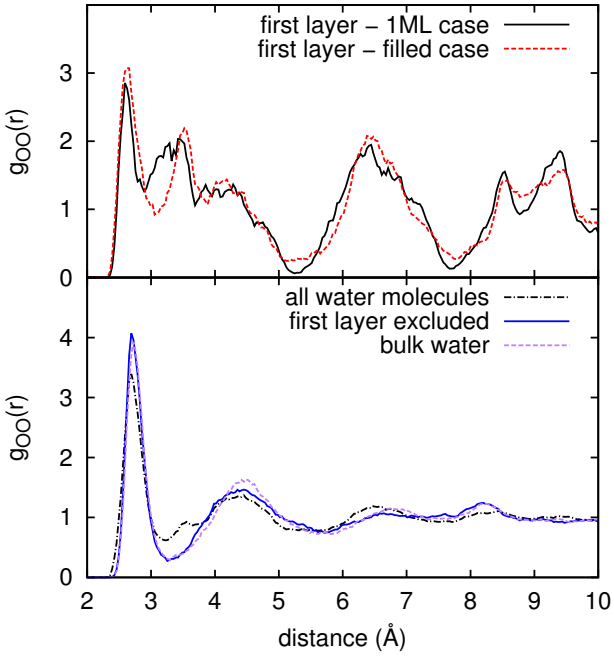

Figure 3.16: *O-O pair correlation function in the interfacial water. The top panel compares the O-O distances in the first layer only - the black line for the single adsorbed monolayer simulation, and the red line in the filled case. The second panel compares O-O distances in the filled water simulation (black dashed and blue lines) with O-O distances in a reference simulation of bulk water (purple line).*

with a water molecule. The second peak shows high oxygen and hydrogen presence, which reflects the stability of the first layer – throughout the simulation, the 6 adsorbed water molecules on each side do not diffuse towards the $z \approx 0$ region, where there is on average a lower water density. The stability of this first layer is further shown when looking at the oxygen-oxygen pair correlation function in the top part of figure 3.16. The structure of the monolayer remains largely unchanged when more water molecules are added, with a strong collapse of the second neighbour peak compared to liquid water. This type of structuring on MgO(001) has been proposed to resemble a high density ice phase [85], and could be attributed to a template effect. However, interestingly, similar structural properties have been seen in simulations where there is little or no templating, such as on BaF_2 in which the first layer exhibits an O-O pair correlation function resembling that of high density liquid water [21]. The high density water layer adsorbed on MgO(001) is followed directly by a depleted zone, something that has already been reported in studies of water on other oxide surfaces [14, 86] and even on graphene and h-BN [20, 87]. In the case of oxides, the initial affinity of the surface for water seems reversed after one layer of coverage – a 'hydrophilic' surface can become 'hydrophobic' once wet [86].

3.4.1 Surface-assisted proton transfer

The green histogram in figure 3.15 was obtained by counting the number of times an oxygen atom had a switch in one of its two nearest neighbour hydrogen atoms, thus counting the number of proton transfer, or 'proton hopping' events. In the (2×3) reconstruction shown in figure 3.10, proton transfer is susceptible to occur, simply because the high density of the adsorbed layer means that the oxygen atoms are near enough to each other, and also because the layer is partly dissociated which means there are OH groups free to receive the hopping proton from a neighbouring water molecule. Thus it is possible to imagine further metastable configurations from figure 3.10, and these were observed frequently in our 300K simulation. Such frequent proton transfer at an oxide surface has also been observed in simulations of ZnO [88]. There are two peaks on each side of the histogram. The peak closest to the surface counts the proton transfers within the adsorbed layer, parallel to the surface. The second peak is less intense, and corresponds to hydrogen bonds in the z direction. As shown in the third snapshot in figure 3.3 this corresponds to proton transfer events between the first adsorbed layer and the second layer. It has been recently shown that strong external electric fields promote molecular dissociation and proton hopping in bulk water [29], ice [89, 90], liquid methanol [32], as well as a strong chemical reactivity in molecular mixtures[2]. In this case we notice that proton transfer occurs in the first and second layers above the surface corresponding to the zones of highest electric field.

Proton transfer in water has also been shown to be correlated to short oxygen-oxygen distance. For instance in the simplest case, the Zundel ion, there is a threshold of oxygen-oxygen distance under which the excess proton prefers to lie in the centre of the two oxygen atoms. In the DFT framework this distance is found to be 2.5 Å although more precise treatments of the problem finds this distance to be closer to 2.4 Å [91]. Classically, proton transfer is expected to occur when the oxygen atoms are closer than this minimum distance, apart from processes of tunnelling, where a quantum treatment of the proton is needed [92]. Figure 3.17 shows distributions of the oxygen-oxygen distances for hydrogen bonded water molecules, in the first and second layers, and in the other water molecules. With regard to proton transfer, it is important to note that the O-O distances concerned are those which are below the threshold mentioned above. It is clear that there are more very short O-O distances near the surfaces than in the middle of the simulation box. The layers nearest the surfaces have more than 10% of their O-O distances below the DFT proton-hopping threshold, while those in the next slice have between 5% and 10%. Although some bulk water properties seem to be recovered just after the first layer, the heightened density seems to permeate

through to the second layer and promote proton transfer. Although proton transfer is more likely when there are more O-O distances well below the threshold, this is not the only driving force for the transfer. Thus the percentage of O-O distances lying below the threshold is not linearly representative of the number of hops.

The average shortening time during which an O-O distance stays below 2.5 Å is also found to be correlated with proximity to the surface – with averages of 33, 29, and 21 fs in the first and second layers, and in the bulk, respectively. In this particular study, the proton transfer results in a net transfer of OH^- ions, as these are initially present on the surface. This type of transfer has been shown to depend strongly on the local coordination of the OH^-, namely OH^- ions which receive three hydrogen bonds are more likely to diffuse than those of a higher coordinance [93]. OH^- ions on the MgO(001) surface receive two hydrogen bonds from water molecules in the monolayer, and can receive a third from the water molecules above. These are in effect undercoordinated, which probably promotes the transfer of the OH^- when it is near the surface. Once the OH^- is solvated it is not longer undercoordinated with respect to hydrogen bonding. To summarise, there are several ways in which the surface assists proton transfer: the presence of undercoordinated OH^- ions, shorter O-O distances, and a high electric field environment. Possible perspectives include a finer analysis of how these factors are correlated to each other and how they quantitatively affect proton transfer.

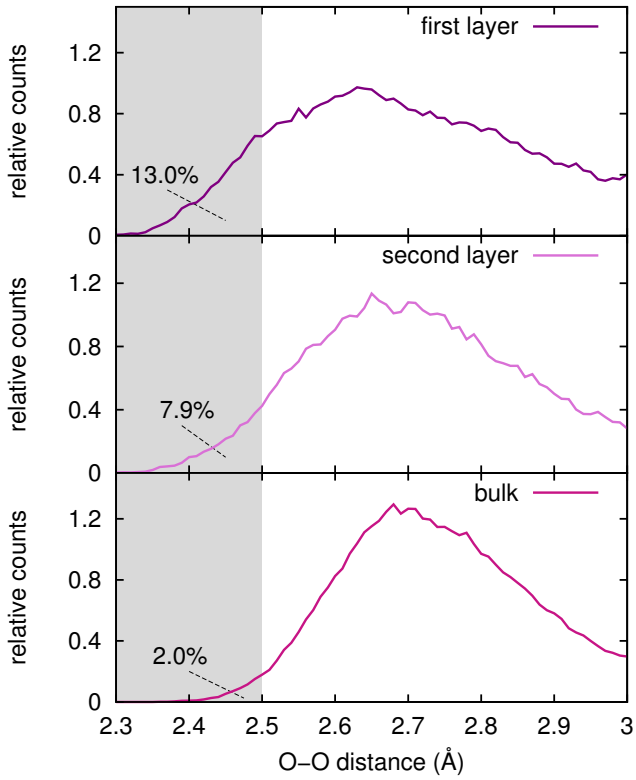

Figure 3.17: *Distributions of the Oxygen-Oxygen distances in the water between the slabs, by layer. The first layer refers to the water molecules within 2Å of the surface on either side of the slab, while the second layer refers to those between 2Å and 4Å away from the surface. The distribution referring to the remaining water molecules is labelled as 'bulk'. An area has been shaded to represent the proton transfer threshold, below which proton transfer may happen. The percentages show how much of each distribution is below this threshold.*

3.5 Mimicking the Surface Electric Field

Starting from the potential profiles in section 3.2, an effective potential can be constructed mimicking certain aspects of the mineral surface. The implementation of such a potential is described below, followed by preliminary results on a test system consisting of confined water.

3.5.1 Description and implementation

The potential chosen has the following expression:

$$V_{\text{applied}}(z) = -V_0 \left[f(-A(z - z_0))^k + f(A(z + z_0 - l))^k \right] \tag{3.1}$$

where $f(z)$ is the sigmoid function:

$$f(z) = \frac{1}{1 + e^{-z}} \tag{3.2}$$

The parameters in equation 3.1 were fitted to the planar, macroscopic average of the intrinsic MgO(100) electrostatic potential, as we can see in figure 3.18. V_0 corresponds to the height of the potential in Rydberg, z_0 to the position of the peak in electric field, which is a little above the position of the surface atoms. l is the length of the simulation box in the z direction. A and k are parameters adjusting the slope of the potential in the surface regions. The resulting function is one which can be applied with PBCs as long as $z_0 < \frac{l}{2}$, and mimics the macroscopic electrostatic potential of a slab which is centered around 0 and $2z_0$ wide in the z direction. In this particular case the parameters were found to be $V_0 = 0.714$ Ry, $k = 0.5$, and if we use fractional coordinates we set $z_0 = 0.24$, $l = 1$ and $A = 130$. These parameters could easily be adjusted to change for example slab thickness, or strength of the field at the surface.

3.5.2 Tests and Remarks

Tests were performed to verify the implemented potential and forces. To do this a hydrogen atom was placed in the potential and its z coordinate was varied, with a DFT ground state calculated for each z coordinate. In this simple one-atom system the ionic and electronic components of the energy and of the force could be computed independently. Figure 3.19 shows the forces obtained. To check for consistency between forces and energy, the derivative of the energy was obtained with respect to the position. These values are also plotted in the figure and we can see the variation in energy is consistent with the force.

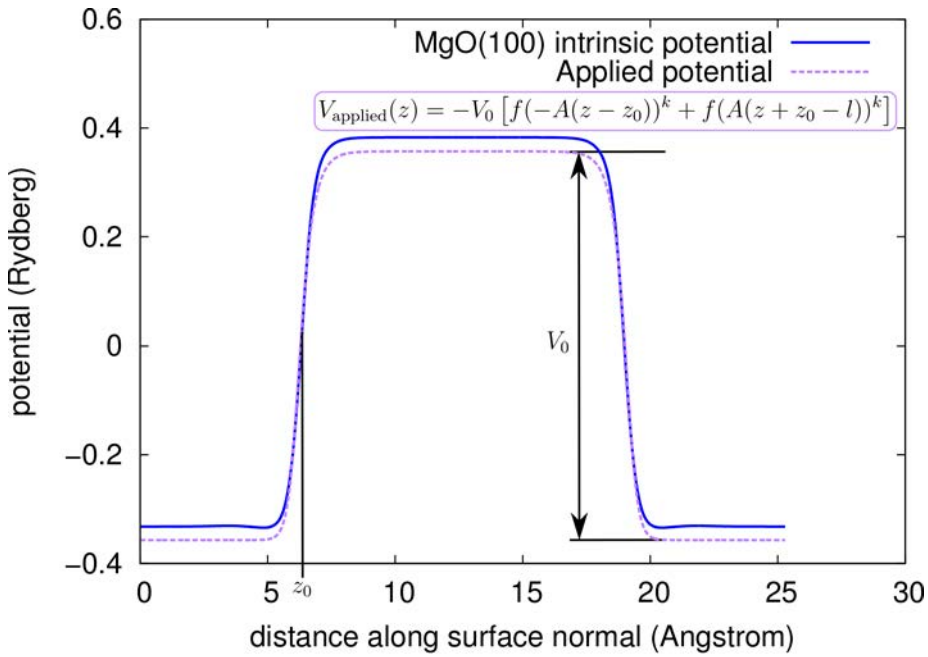

Figure 3.18: *Comparison of the surface potential of MgO(100) and our applied potential, along with an illustration of the parameters of the potential*

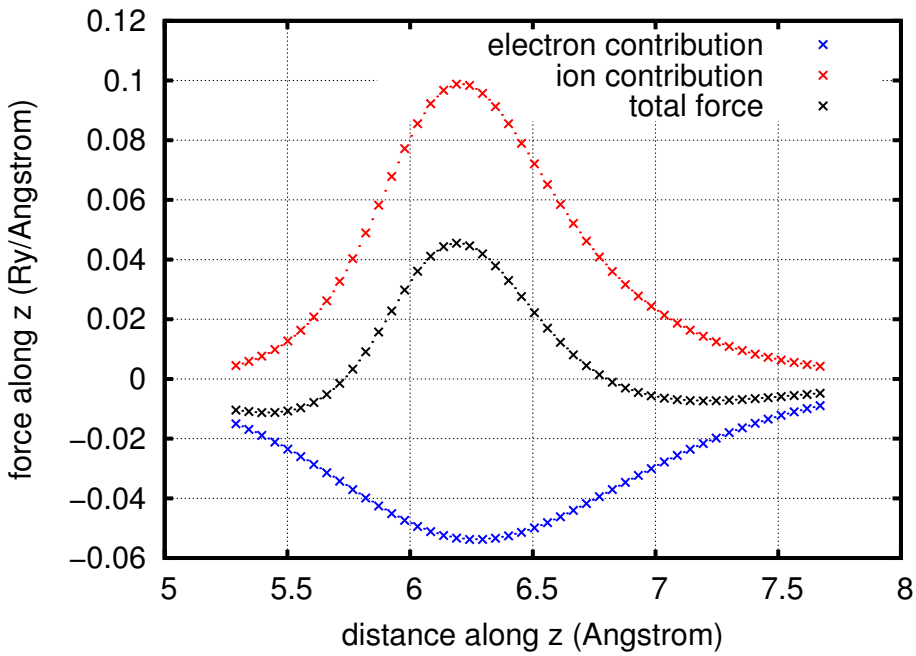

Figure 3.19: *Tests on the potential within the interfacial region. The corresponding energy derivatives are shown as dots.*

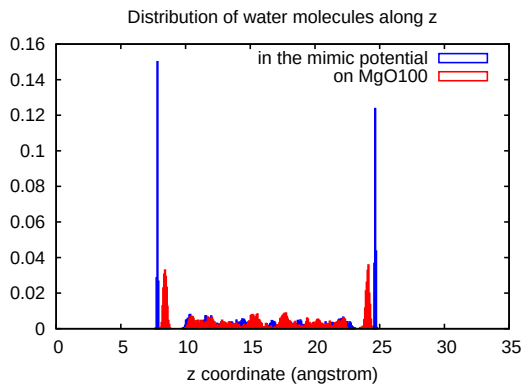

Figure 3.20: *z distributions in both cases*

We see that, as expected, the forces due to the electrons in the field are opposite to the ionic forces. The zone of interest is above 6.5 Å as the 'virtual slab' is located symmetrically about zero and extends to about 6 Å. The sum of the two components show the total force on the hydrogen atom in the field. There is a change in the direction of the total force at a point which corresponds to about 1 Å above the surface. This point of zero force would seem to coincide with the 2D confinement corresponding to the 1st water-layer adsorbed on MgO. We expect the potential to mimic the surface at least in the confinement of a layer of atoms during MD as long as these atoms do not have enough kinetic energy to cross this confinement barrier.

3.5.3 Results

Simulations were run which are identical to those in section 3.4, except that the MgO atoms were replaced with the mimic potential. The starting configuration included the 2×3 reconstruction shown previously. When relaxing the system the dissociated water molecules reassociated, and then rearranged to include not 6, but 7 molecules in the first layer. At 300K the water is indeed confined to this potential. Figure 3.20 shows the z distribution of oxygen atoms in the case of the real surface compared to the virtual surface case. The z distribution seems to be reproduced qualitatively but the confinement to the first layer is dramatically increased.

To attempt to reproduce the surface correctly, several possible effects were investigated. Firstly, the effect of the screening from the first layer of water molecules was studied by comparing the electrostatic profiles of the isolated parts of the system (MgO100 bare, the first water layer) to the electrostatic profile of the system as a whole (MgO100 + 1ML water). This is shown in figure 3.21. We see that the effect of screening is only slight, and cannot completely lift the discrepancy

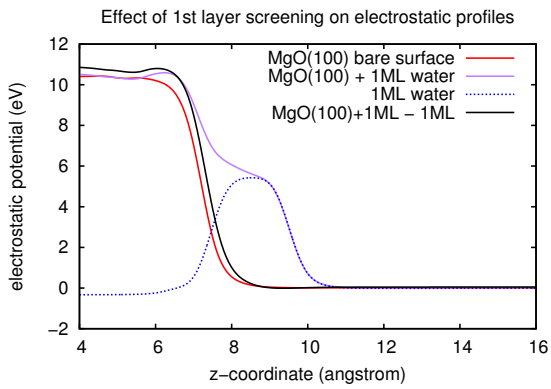

Figure 3.21: *Electrostatic potential profiles on MgO(001), showing the interface with vacuum and with one monolayer. The profile corresponding to the monolayer alone is also shown, and the black line represents the screening effect due to the addition of a water monolayer. This effect seems small (difference between the red and black line).*

between the confinement on the real surface and is the potential implemented to mimic the surface.

This approach would greatly reduce the computation time needed, if indeed the density oscillations of liquid water on top of a mineral surface were well reproduced, because the atoms of the mineral would not need to be explicitly included in the simulation. Such a potential could perhaps be moved to a forcefield MD simulation to simulate larger scale isolated 'thin films', however it is not certain that this would work – as discussed previously, the confinement seems to come from the difference in electronic and ionic force contributions, which is not something directly calculated in forcefield MD, although polarisable models may well reproduce this confinement with a purely electrostatic barrier. Furthermore, proton exchange cannot be reproduced in this case, as the surface OH groups are no longer present. One would need to include ionic pairs such as NaOH or HCl to observe proton exchange in this system on AIMD timescale. Nevertheless this simplistic way of representing the surface could be worth investigating further as a means of modeling reactions happening in near-surface or confined water.

3.6 Conclusion

Non-polar, defectless surfaces, such as our model MgO(001) one, may exhibit high electric fields at distances of up to 3 Å. When a single monolayer of water molecules is added, the electric field is less intense but still present, and furthermore the zone of high field seems to be broadened to about 5 Å from the original surface. In a way, this first layer of water serves to spread the high-field interfacial

region. Upon adding several layers of water, and after a coarse graining of the field, the 5 Å window above the surface in which the electric field is high (1 - 3 V/Å) remains. There is a clear difference between the water molecules belonging to the first layer, which keep close to their initial configuration, and the other water molecules which are free to diffuse. The atomic density profiles show a depleted zone just above the adsorbed layer, and the O-O pair correlation function is similar to that of bulk water once the first adsorbed layer is not taken into account. An attempt was made to simulate a surface field without including the surface atoms explicitly – so far the simulations seem to reproduce the layering of the water molecules adjacent to the surface, at least qualitatively. Further investigation of this virtual surface is needed to determine its efficacy on near-surface processes. Proton transfer occurs at the MgO(001)/water interface, and this is observed at significant rates on AIMD-accessible timescales. Our results show that proton transfer occurs in the zone close to the surface where the electric field is strongest. This can be partly explained by a higher proportion of small O-O distances in those zones.

In perspective, this part of the study suggests that local electric fields at the surface of dry and wet oxides and minerals are sufficiently intense, even in clean, flat, and apolar surfaces as MgO(001), to promote molecular dissociations, and thus to modify the free energy landscape of surface chemical reactions, with important consequences in geochemistry.

Chapter 4

Surface Effects on a Pre-biotic Reaction

In this chapter the free energy landscape of a pre-biotic reaction is computed in solution and at the MgO(001)/water interface. The reaction chosen is $CO+H_2O \longleftrightarrow HCOOH$, which is one of the simplest possible reactions in this context, as it requires only the addition of a carbon monoxide molecule in our simulation cell. Formic acid is the shortest carboxylic acid, and thus it is a potential precursor for lipids and sugars, as well as amino acids and bases. All solvent and surface atoms are taken explicitly into account, and using metadynamics outlined in section 2.3.2, transition pathways were found with no *a priori* knowledge of the transition states. Umbrella sampling was used to compute free energy landscapes to about 5 kcal/mol accuracy. The reaction was also studied in solution with an external applied electric field of 0.3 V/Å, in order to estimate and compare the effect of the surface electric field in the free energy landscape.

4.1 Introduction and Context

The Miller-Urey experiment in 1953 [1] was a turning point in the field of pre-biotic chemistry by showing that amino acids and sugars can be synthesised abiotically from compounds which could have been available in earth's early atmosphere. Proposed precursors include small molecules such as H_2, N_2, CO, CO_2, H_2O, NH_3, and CH_4 [4], with various hypotheses of how these could have combined in the early earth, or indeed on asteroids or other planets. Molecules such as hydrogen cyanide, formamide and formic acid may have then been intermediate molecules on the road to both amino acids and sugars, thus being common ancestors to both the RNA and protein world views [53]. In this context, electric fields have been shown to greatly impact reaction pathways and free energy landscapes [94]. In parallel, mineral surfaces are expected to have an im-

portant catalytic role in pre-biotic chemistry, and indeed can exhibit spontaneous electric fields of the order of V/Å [23, 22]. Thus in this study we aim to study a relevant pre-biotic reaction, CO + $H_2O \longleftrightarrow$ HCOOH, at a model mineral interface, MgO(001)/water, and evaluate the impact of the surface electric field on the free energy landscape.

Reactions involving formic acid have been widely studied due to its importance in industrial processes. Formic acid is a known intermediate sate in the water-gas shift reaction, which generates hydrogen from water to be used in fuel cells [95], and has many uses in the food industry due to its low toxicity and as it is a by-product of acetic acid formation. The decomposition of formic acid has been studied both experimentally [96] and computationally [97, 98, 99] and globally it is agreed that the relative stabilities of the reactants and products depend on solvent density and temperature. However, computational investigations to date have never fully taken the solvent into account explicitly. Furthermore, the presence of Alumina and Magnesia have been shown to catalyse this reaction in industrial processes [100]. In this study we also show simulations of a reaction yielding formic acid, at the MgO(001) surface in solution.

It is known that an applied electric potential can modify reaction rates. Oriented electric fields at an STM tip have recently been shown to accelerate the formation of carbon-carbon bonds [27], thus expanding the field of electrostatic catalysis to beyond redox systems. Enzyme catalysis has been shown to depend strongly on the high electric fields generated at the catalytic sites, which are also on the order of V/Å [33]. In this study we look at the effect of applying a strong electric field, chosen at 0.3 V/Å, just below the dissociation threshold of water [29]. Mineral/water interfaces are also high electric field environments and in this work we attempt to elucidate the electric field contribution of the surface to the free energy landscape of the targeted reaction.

4.2 Preliminary Study of the Configuration Space

The collective variables used are those described in section 2.3.1, based on coordination number of specific atoms in the targeted reaction. The coordination numbers are shown to nearest integer values in figure 4.1, with colours highlighting the parts of the matrix which are expected to change during the reaction. In reality these integer values are not ideal in solution, as the atoms are also coordinated to the solvent. Thus the actual coordination values used in the simulations are those outlined in tables 4.1. To obtain these numbers equilibrium simulations were run of CO in water and HCOOH in water, while recording the coordination

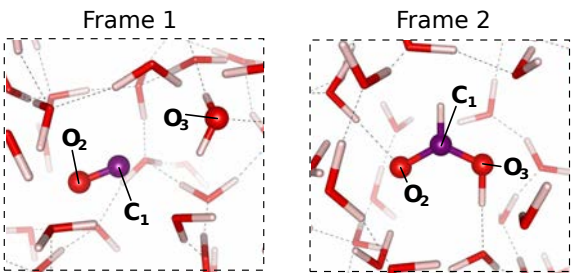

	C	O	H
C_1	0	1	0
O_2	1	0	0
O_3	0	0	2

	C	O	H
C_1	0	2	1
O_2	1	0	0
O_3	1	0	1

Figure 4.1: *Illustration of the path variables. The matrix entries which are modified during the metadynamics run are highlighted. The snapshots show the system in the CO+H_2O state (left) and in the HCOOH state (right). Oxygen atoms are drawn red, hydrogen white, and the carbon atom is drawn in purple. The atoms represented as bigger spheres are those selected to react in metadynamics, and their labels correspond to the rows of the tables.*

numbers throughout the simulations. The values shown in the table correspond to the average values of these equilibrium runs.

We can notice that although when looking at the integer values some of the matrix elements do not seem to change at all, this is no longer the case when fractional coordination numbers are taken into account. A clear example is the row corresponding to the second oxygen label O_2, which remains coordinated to one carbon atom throughout the simulations. When looking at integer coordination numbers, this row does not seem to be modified in the matrix, however with fractional coordinations from the solvent there is an increase to coordination of this atoms to other oxygens and especially hydrogens. This shows the greater interaction which formic acid has with water as compared to carbon monoxide. Indeed, first attempts at modeling this reaction using a smaller matrix, omitting the row in question, resulted in less efficient metadynamics, that is more hills were added before the first reaction occurred. The finer effects of these topological variables are not fully understood yet and for the moment each specific case needs to be set up via trial and error. The specific coordination in table 4.1 numbers depend on the cutoff used which is specified for this case in the appendix.

Figure 4.2 shows an example of a metadynamics run, to illustrate the relationship between collective variable (CV) space and configuration space. The basin on the left corresponds to frame 1, CO+H_2O. The basin on the right corresponds to formic acid. Frame 2 is located at around $s = 2, z = 0$ in CV space, however the

	C	O	H
C_1	0.000	1.190	0.196
O_2	0.940	0.252	0.194
O_3	0.011	0.433	2.577

	C	O	H
C_1	0.000	1.942	1.166
O_2	0.909	0.460	0.533
O_3	0.858	0.477	1.285

Table 4.1: *Tables representing the transition from CO+H_2O (left) to HCOOH (right).*

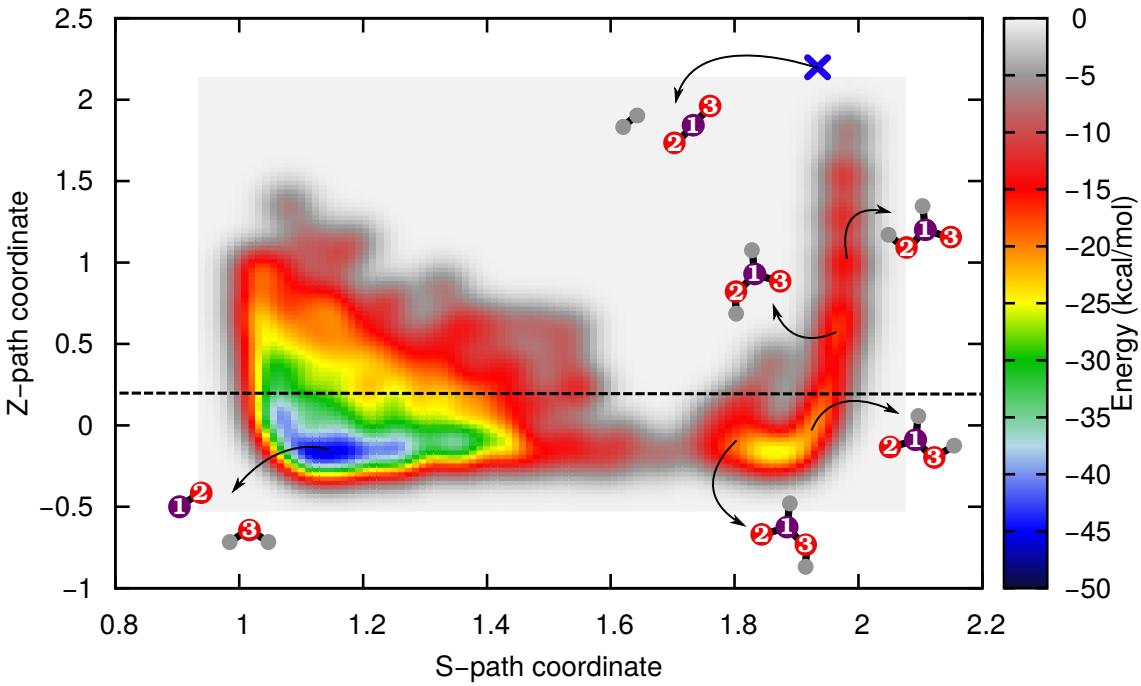

Figure 4.2: *Example of an unconverged FES from a metadynamics run. Schematic configurations are shown corresponding to approximate locations of CO+H_2O, HCOOH-cis and HCOOH-trans, as well as configuration isomers which are an artifact of the labelling of the atoms. We can see that the cis and trans configurations occurring above the line are equivalent to those below the line.*

formic acid basin extends to higher z. This corresponds to isomers of formic acid, not only structural isomers but also permutation isomers which are an artifact of the labelling of the atoms, as shown schematically in figure 4.2. In theory the entire basin could be sampled, but in practice this takes too long and instead a quadratic wall is applied along the z path CV. The wall chosen in this study was then fixed at $z_W = 0.2$, as illustrated in the figure. The wall does not leave out any important parts of the transition, which occurs at low values of z. The figure also includes the position in s, z of the CO_2+H_2 state not investigated in this work. It was attained on some trial runs and the corresponding basin was not clearly separate from the HCOOH basin. Furthermore, it is too high along z to be correctly investigated using the same CVs.

Here it is important to note two things about the chosen CVs. Firstly, the rows of the tables in figure 4.1 and tables 4.1 refer to specific atoms in the simulation, which have been given indices in the representation, whereas the columns refer to species of atoms, and include coordination to all other atoms in the box. This means that the choice of O_3 is arbitrary, and also that the corresponding water molecule plays the role of both solvent and reactant. In practice the water molecule was chosen as the closest to the C atom in the starting configuration. Secondly, hydrogen atoms not being explicitly indexed in the CV is an advantage as they stay 'free' to be exchanged and participate in the reaction, which proved important especially in the case of the electric field. This however means that the decarboxylation pathway HCOOH $\longleftrightarrow$ CO_2+H_2 could not be adequately studied as the free energy basins are too close in the CV space, and much higher in z than our chosen wall. An example of a CO_2+H_2 configuration, and it's corresponding location in sz space, is shown in figure 4.2 to illustrate this. Furthermore, since the hydrogen atoms are not specifically indexed in the frames of the collective variables, once the state CO_2+H_2 is achieved, the metadynamics would not have been effective in splitting the H_2 molecule. The choice of the variable is thus a trade-off between free proton exchange regardless of the hydrogen labels, and accessing the CO_2+H_2 state.

A marked advantage of this definition for the path variables is that they are defined in exactly the same way in all simulations, including the MgO surface case. Thus for what follows table 4.1 was used to define frames 1 and 2, and all reactions are mapped onto the s, z space identical to that shown in figure 4.2. In each case the simulation procedure involved exploratory metadynamics to obtain a reaction pathway, and a first estimation of the free energy landscape, umbrella sampling runs along the path, and some commitor analysis to find a transition state.

4.3 Simulation Procedure

1. **Exploratory metadynamics:** The first step in finding the free energy profile of the reaction is an exploratory one. The simulation cells are set up with 34 water molecules and 1 carbon monoxide molecule, with the parameters outlines in the appendix. We perform metadynamics using the path collective variables described above. The metadynamics is left to run until the system is pushed to react, and then left further until the 'backwards' reaction is observed, and we have a transition from frame 2 to frame 1. Once this has occurred we have a first estimatefor the free energy landscape, as well as a reaction mechanism. This estimate can be improved by using the newly found reaction pathway to perform umbrella sampling simulations.

2. **Umbrella Sampling:** Umbrella sampling was performed with quadratic potentials in s and z, centred along the reaction pathway found in the exploratory step. The bias from the metadynamics step is also applied on top of the umbrella potentials. Adding this bias is in principle "flattening" the landscape, and improves the efficiency of the umbrella sampling. Each umbrella sampling simulation in the bulk was run for 5 ps, discarding the first pico-second as equilibration time. Due to being computationally expensive, the surface simulations were run for 2.5ps. The statistics was found to be almost as good for these shorter runs, with the difference in precision reflected by the larger error bars for the data in the surface simulations. The weighted histogram analysis method was applied to obtain free energy profiles. Using the homemade code for the WHAM, data from unconstrained runs was able to contribute to the overall statistics. The unconstrained runs correspond to 'starting' and 'ending' configurations, and were also useful for analysis such as the angular distribution of the molecular dipoles in the field.

3. **Uncertainty estimates:** All uncertainties estimated in the following come from checking the ergodicity of the umbrella sampling simulations. For each umbrella run the data was split into two 2 ps blocks and the WHAM was applied to both sets independently. The value at the energy minima and height of the barrier was then taken as the average of the two, with an uncertainty taken as the difference between the two 2 ps data sets. Similarly for the surface simulation, the data was split into two 1 ps sets.

4. **Finding the transition state:** To find suitable transition states, configurations were taken from the initial exploratory metadynamics, and left to evolve freely given an initial temperature, with random velocities following

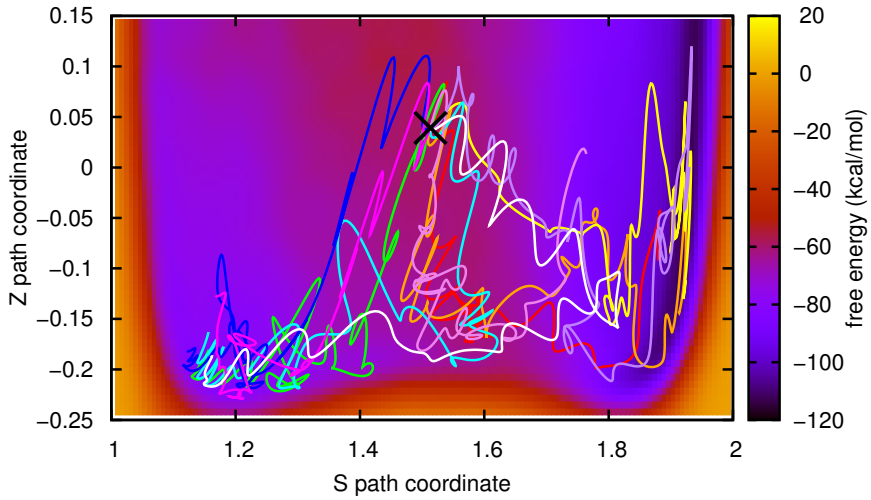

Figure 4.3: *Example of ten unbiased trajectories starting from a putative transition state. The metadynamics estimate of the underlying free energy landscape is shown. The cross corresponds to the starting point in s, z space of the trajectories.*

the Maxwell-Boltzmann distribution. Ten replicas were initialised to test each configuration, and if about half of those ended up in the CO+H_2O state, and the other half in the HCOOH state, then the configuration was assumed to be a transition state. An example of ten trajectories starting from the same putative transition state is shown in figure 4.3. We can see that each trajectory is unique and that in this case five end up in the CO+H_2O basin, while the other five end up in the HCOOH state. The messy aspect of these trajectories is typical of this kind of analysis — although the starting positions are identical, the starting velocities are randomised resulting in wildly different trajectories.

4.4 Temperature and Electric Field Effects

Simulations in the bulk liquid were run at two temperatures (300K and 400K) and at two electric field strengths (0 and 0.3 V/Å), making a total of four bulk liquid simulations. The free energy profiles at 300K and 400K are shown in figures 4.4 and 4.5 respectively. The results are summarised using only the *s*-coordinate in figure 4.6. We can see that the temperature seems to have little effect on the stability of the product, with respect to the CO+H_2O. We expect lowering of the barrier with increased temperature since experimentally, the synthesis of formic acid without catalysts requires hydrothermal conditions [97], however this effect

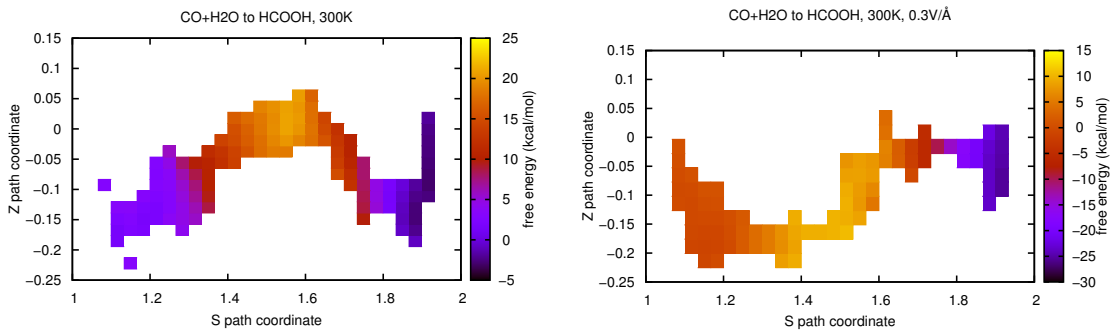

Figure 4.4: *Free energy landscapes obtained for the simulations performed at 300K. The basin close to S = 1 corresponds to CO+H_2O whereas the basin around S = 2 corresponds to the HCOOH state. The difference in the shape on the sampled landscape corresponds to topological differences in the path taken with and without an electric field.*

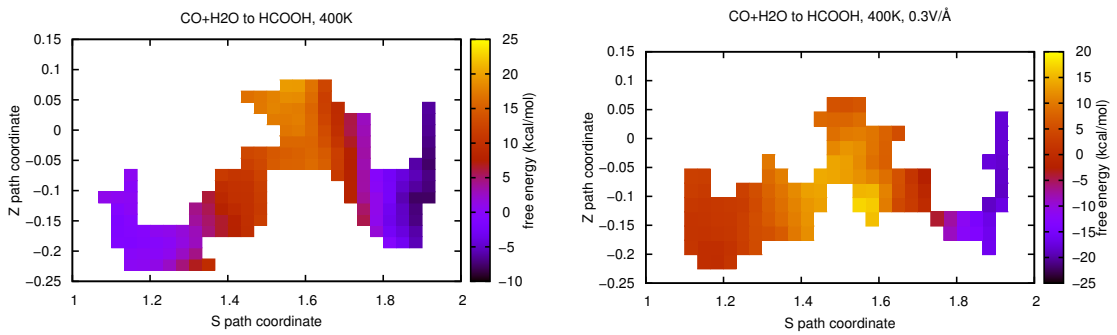

Figure 4.5: *Free energy landscapes obtained for the simulations performed at 400K. As in figure 4.4, the two basins can be observed. Again, the field induces a change in the path and a deepening of the HCOOH basin.*

may be within our error estimate. Application of an electric field has a significant effect at both temperatures. The barrier is lowered by about 7 kcal/mol and formic acid is stabilised by the field. The effect of the field is more significant at 300K than at 400K, indicating that the contribution to the free energy may be entropic in nature, a point which will be discussed later on. When looking at orientations taken from the unconstrained equilibrium runs shown in figure 4.7, we see that the main difference between the two temperatures is that at 300K carbon monoxide is orientated by the field whereas at 400K the thermal agitation seems to overcome this preferred alignment. For formic acid the orientation is affected by the field at both temperatures to a similar degree. This can be explained by the dipole moment of formic acid, which is about an order of magnitude higher than the dipole moment of carbon monoxide in the gas phase.

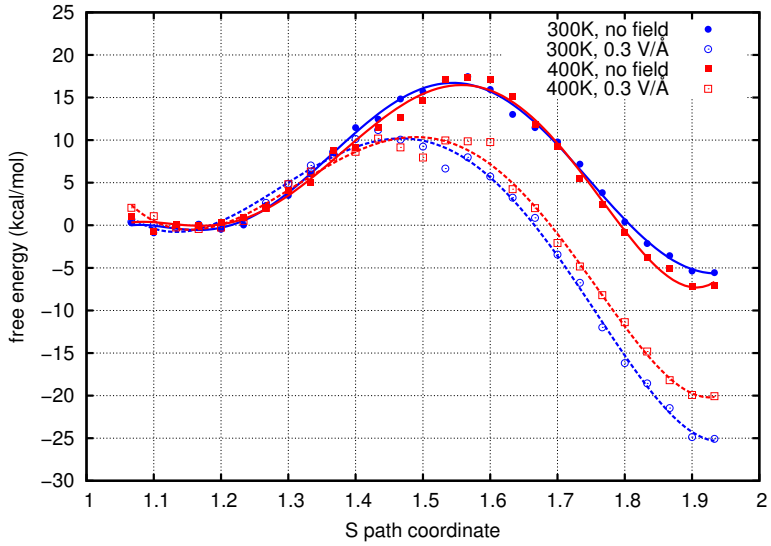

Figure 4.6: *Comparison of free energy profiles for the reaction at 300K and 400K; with and without and electric field, and on the surface. The values are given relative the the CO+H_2O state in each case. Data points correspond to the average free energy for each s-value from the graphs in figures 4.4 and 4.5. Polynomial fits are drawn as a guide to the eye.*

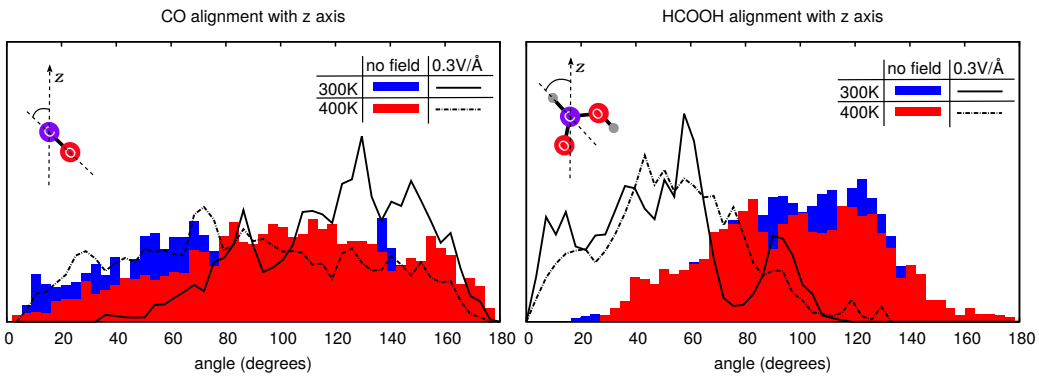

Figure 4.7: *Molecular alignment with the z axis in the equilibrium simulations, at 300K and 400K, with and without an applied electric field. Insets show how the angle with the z axis is defined for each molecule.*

4.5 Effect of the Mineral Surface

Presence of a mineral surface is known to modify reaction pathways and free energy. More specifically, MgO(001) strongly affects the propylene partial oxidation by Ag_3 [101], as well as modifying the barriers in reactions of N_2 and H_2 on Zr_2Pd_2 clusters [102]. Pyrite surfaces have been shown to modify the energetics of hydrolysis and formation of peptides [103]. In these examples the interaction between the reactants and the surface may not be due to direct adsorption, but rather due to electrostatic effects. Water itself has recently been shown to have very different dielectric properties in confinement up to 1 nm [24]. Here we investigate the targeted reaction at a well-characterised oxide surface — MgO(001) — in order to compare surface effects to bulk electric field effects, the hypothesis being that the electrostatic field coming from the surface may manifest itself on the kinetics and thermodynamics of the reaction.

The metadynamics simulation was thus run in the vicinity of the MgO(001) surface. The same simulation box was used as in chapter 3, however dimensions were doubled in the x direction to allow for better solvation of carbon monoxide and of formic acid. A snapshot of the simualtion box is shown in figure 4.8. Compared to the MgO+water system, one CO molecule was added near each side of the slab. A free simulation was run at 400K for a few picoseconds and both CO molecules were found to remain within 3 Å of the surface. The first CO was then used to apply metadynamics and obtain a reaction. The second CO was left 'free' to increase statistics of CO at the surface and as a control. Throughout the runs the unbiased CO was never found to spontaneously react, which is not surprising considering the free energy barrier, but was also found the remain close to its initial z coordinate while diffusing freely along x and y. This suggests that molecules may be loosely bound to the surface vicinity without specific adsorption on the surface, at least for short timescales.

For the metadynamics run, all solvent atoms were included to participate in the coordination tables shown in 4.1, as well as the surface atoms. This means that the surface and solvent participation was not pre-determined by the metadynamics run. Several trial runs enabled us to determine that a good choice of the reacting water molecule is one in the second layer, just above the adsorbed water monolayer. The final FES from the metadynamics + umbrella sampling run is shown in figure 4.9, and figure 4.10 summarises the barrier and stability changes in all 400K simulations.

The striking feature of the free energy landscape is the stabilisation of the

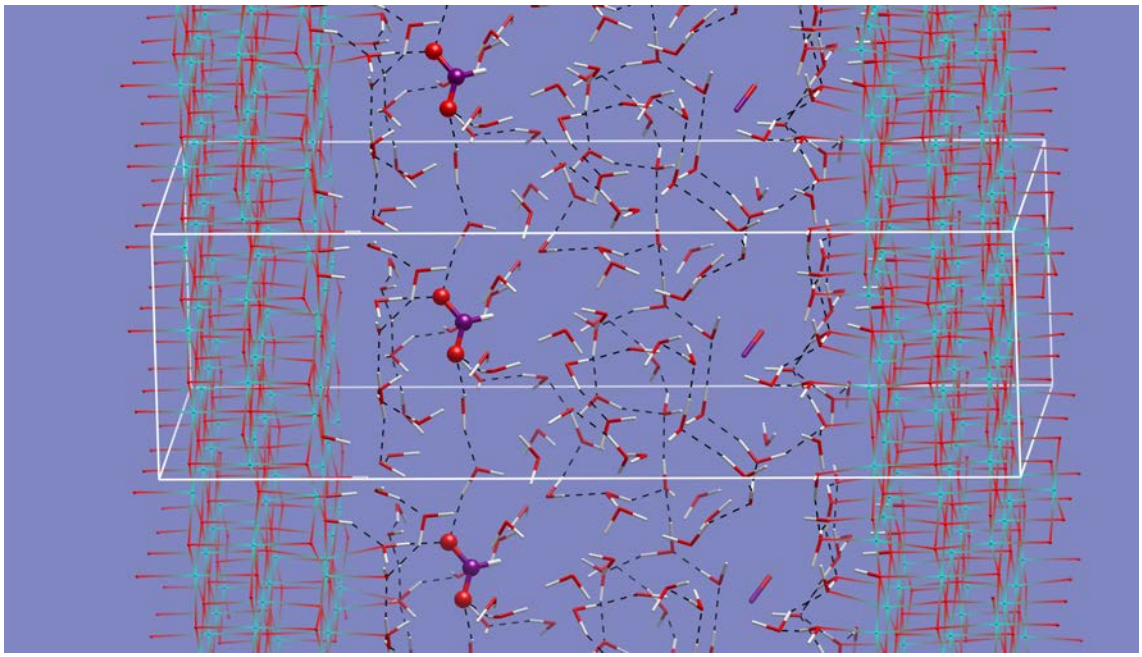

Figure 4.8: *Snapshot of the simulation box. The MgO bonds are shown as turquoise and red lines. The oxygen atoms are red, hydrogen is white, and carbon purple. The atoms selected for the reaction are shown as larger spheres. The unit cell is shown in white, and several periodic replicas are also shown. In this snapshot we see the hydrogen bonded formate ion, oriented by the surface.*

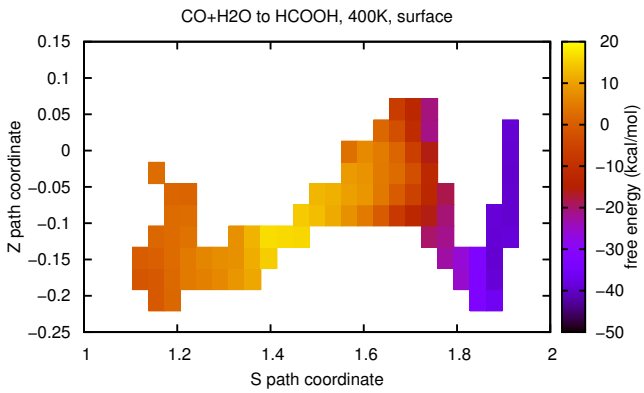

Figure 4.9: *Free energy landscape obtained for the simulations performed at 400K, on the MgO(001) surface. The CO+H_2O basin is observable on the left, while the right side corresponds to the HCOOH state. As in figures 4.4 and 4.5, a deepening of the basin corresponding to formic acid is observed compared to the bulk case.*

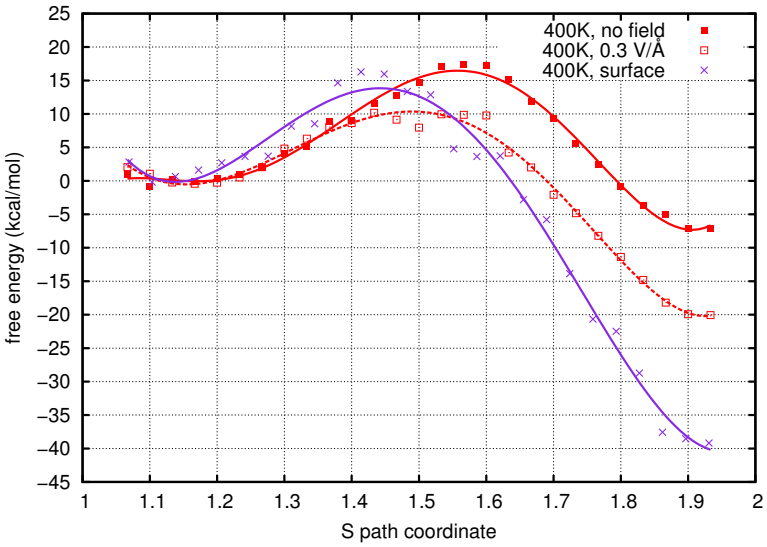

Figure 4.10: *Comparison of free energy profiles for the reaction at 400K; with and without and electric field, and on the surface. The values are given relative to the CO+H_2O state in each case. Data points correspond to the average free energy for each s-value from the graphs in figures 4.5 and 4.9. Polynomial fits are drawn as a guide to the eye.*

product by 40 kcal/mol compared to the bulk, no field case. This means that over long enough times the equilibrium concentration of the product with respect to the reactant is strongly shifted in the surface vicinity. When comparing to the effect of a field, we can say that the stabilisation of the product is also observed near the surface. Furthermore, the barrier appears slightly lowered, although the lowering is close to our error estimate. Clearly an electric field alone cannot reproduce all surface effects, such as for example local pH. However when looking at the orientation of the formic acid molecule in the equilibrium run (figure 4.11) we can see that the preferred orientation is similar to that in bulk electric field. The z axis refers to the surface normal, and as outlined in chapter 3, so the observed orientation of the molecule on the surface is consistent with the direction of the surface field. Thus, further analysis is needed in order to gauge the effect of the field and how it compares to other effects such as local pH.

4.6 Further Analysis

Once the free energy landscape is obtained, further analysis can be done on the trajectories of the umbrella sampling runs. Statistics of the free runs corresponding to frame 1 and frame 2, as well as the umbrella run corresponding to the transition state, are analysed below.

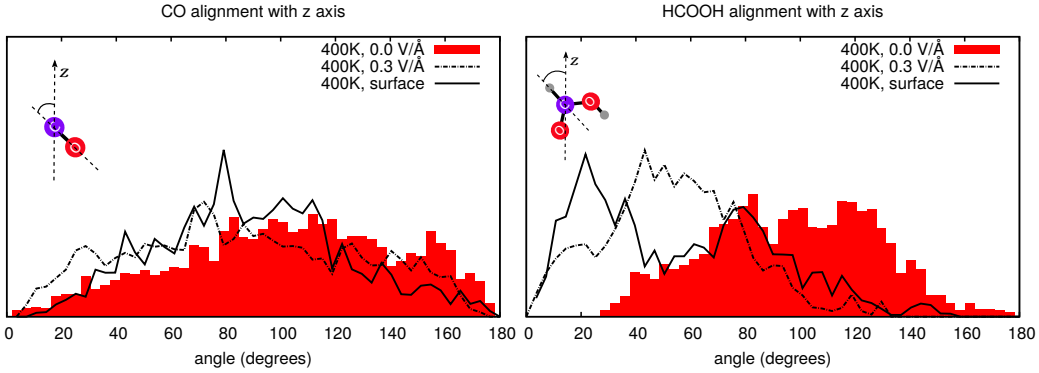

Figure 4.11: *Molecular alignment with the z axis in the equilibrium simulations, at 400K comparing the electric field effect to the surface.*

Simulation	ΔF	ΔE	$-T\Delta S$	$\Delta U_{\text{dip,gas}}$
300K - 0.0V/Å	-5.0	-13.8	8.8	0.0
300K - 0.3V/Å	-22.9	-7.4	-15.5	-9.0
400K - 0.0V/Å	-5.1	-2.8	-2.3	0.0
400K - 0.3V/Å	-16.9	-5.2	-11.7	-9.0
400K - surface	-38.4	-14.4	-24	-8.4

Table 4.2: *Table showing the energy contributions to the free energy difference between the two states. All values are in kcal/mol. The last column is an estimate of the energy contribution due to alignment of the dipole moment in the field. For these estimates, tabulated gas-phase dipole moments are used – μ_{CO} = 0.122 D, μ_{HCOOH} = 1.415 D, μ_{HCOO^-} = 1.337 D.*

4.6.1 Entropic vs Enthalpic Contributions

The enthalpic contributions can be calculated from the Kohn-Sham energies at each configuration during the simulation, as the cell volume does not vary. This enables us to deduce the entropy contribution. We simply have:

$$\Delta F = \Delta E - T\Delta S \tag{4.1}$$

Where ΔF is the difference in the free energy, ΔE is the Kohn-Sham energy of the system, which in our case at constant pressure and volume is equivalent to the enthalpy, and $-T\Delta S$ is the entropic contribution to the free energy. The results are shown in figure 4.12, with error bars for the free energy obtained as explained in section 4.3, those for the enthalpy obtained by comparing two independent 2 ps data sets. The error bars for the entropic contributions are propagated accordingly. The left panel shows the energy differences between the reactant states and transition states, while the right panel shows the energy difference between the reactant and product states.

First of all we see that the similarity in the 300K and 400K free energy profiles

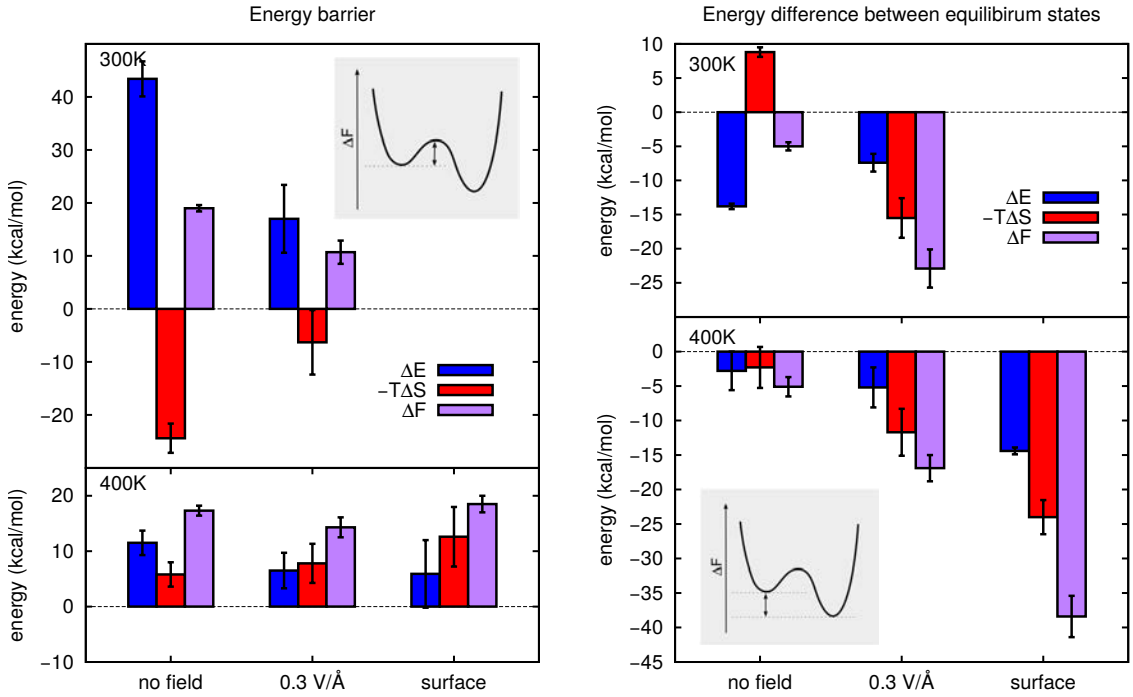

Figure 4.12: *Enthalpic and entropic contributions to the free energy. On the left, the barrier height is represented while on the right, the difference in the free energies of the two stable states is represented. The values are also summarised in tables 4.3 and 4.2.*

Simulation	ΔF_B	ΔE_B	$-T\Delta S_B$
300K - 0.0V/Å	19.0	43.4	-24.4
300K - 0.3V/Å	10.7	17.0	-6.3
400K - 0.0V/Å	17.3	11.5	5.8
400K - 0.3V/Å	14.3	6.5	7.8
400K - surface	18.5	5.9	12.6

Table 4.3: *Table showing the energy contributions to the free energy barrier of the reaction. All values are in kcal/mol*

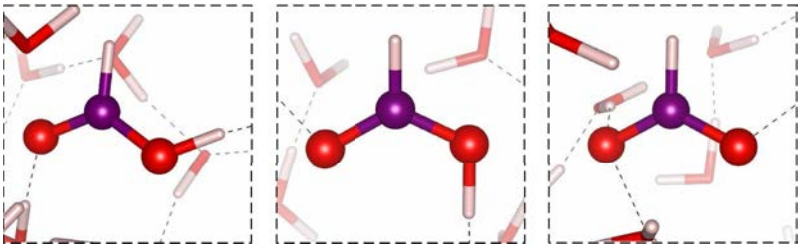

Figure 4.13: *The two isomers of formic acid observed in the simulations, as well as the formate ion which was also observed.*

is due to vastly different energy contributions. This serves to explain why the electric field does not act to the same extent in both simulations. Secondly we notice that the product stabilisation is mostly entropic in the electric field case, and both entropic and enthalpic on the surface. It is difficult to say at this stage if the contributions are due to the surface electric field, and to what extent solvent molecules contribute. To estimate the energy contribution coming from dipole moments aligned in the field, tabulated values of the moments were used in the nominal 0.3V/Åfield. We can note that this value corresponds to the applied field in the bulk case, but is only a very rough estimate of the average field felt by the molecules in the second layer due to the surface. A more exact estimation of this field is under way. The corresponding energies are tabulated in table 4.3, and the values seem compatible the strong enthalpic stabilisation of formic acid by the field. Entropic contributions are more difficult to estimate and work is ongoing to justify entropic contributions to the free energy data presented here.

4.6.2 Transition States and Isomers

Figure 4.13 shows the two isomers of formic acid, here referred to as 'cis' for when both hydrogens are on the same side of the CO single bond in the molecular plane, 'trans' when they are on opposite sides. A representation of the solvated formate ion is also shown. During the equilibrated runs the molecule was found to switch between isomers through proton exchange mechanisms with the solvent. Table 4.4 shows the population rates for isomers after thermalisation was achieved. In the zero field case the cis isomer is stable, whereas once a field is applied the molecule prefers the trans isomer or formate ion. In the near surface case the preferred state is clearly the formate ion. This could be due in part to the surface electric field (as the ion seems aligned with the z axis), but also in part to the local acidity of the surface. The point of zero charge of MgO is between 9.3 and 12 [37], making it acidic at neutral pH. Perspectives include setting up simulations with HCl and NaOH to simulation acidic and basic environments, respectively.

Simulation	cis-isomer	trans-isomer	formate ion
300K - 0.0V/Å	96%	0%	4%
300K - 0.3V/Å	1%	68%	31%
400K - 0.0V/Å	94%	0%	6%
400K - 0.3V/Å	4%	35%	61%
400K - surface	1%	12%	87%

Table 4.4: *Percentages of molecular species observed in the equilibrium simulation. In each case the OH bond was determined by a cut-off distance of 1.2 Å. At each timestep, for the species recognised as formic acid, the sign of the dot product between the OH and CH bonds was used to determine cis- or trans-isomer. If none of the nearest neighbour hydrogens was within 1.2 Å, excluding the one bonded to the carbon atom, then the species was categorised as a formate ion.*

Experimental results show that the decarboxylation pathway is favoured in solution [96], and computational results show that the cis conformer leads to decarboxylation rather than dehydration [94]. It follows that the cis-isomer should be more stable in solution, as found in this study. This also means that the isomer-specific selectivity induced by application of a field could have the double effect of not only stabilising the product but also selecting the dehydration pathway over decarboxylation. The surface simulation also reflects this trend as the trans isomer and formate ions are favoured. Experiments show that on MgO(111) formic acid is molecularly adsorbed at up to 200K, and that above this temperature the formate ion is stable on this surface [104]. This study also found similar results on NiO(111), indicating that qualitative generalisations could be made from one metal oxide surface to another.

Figures 4.14 and 4.15 show the observed transition states for the 300K and 400K simulations, with only the solvent molecules that take part in the reaction shown. In each case at least 4 different water molecules take part in the reaction, in a series of proton exchange events. In all cases the transition state involves at least one OH^-/H_3O^+ ion pair. In the no-field case, at both temperature, the OH^- ion and CO dipoles are anti-aligned, leading to the cis isomer, and when a field is applied the dipoles tend to align with each other, leading to the trans isomer. This is also true on the surface — figure 4.16 shows top views and side views and it is clear that the transition state has dipoles oriented parallel to the surface, and that the dipoles are aligned in the trans configuration. For clarity only water molecules participating directly in the transition are shown, as well as the adsorbed monolayer of water on MgO.

Due to the method used, the transition states shown here are representatives

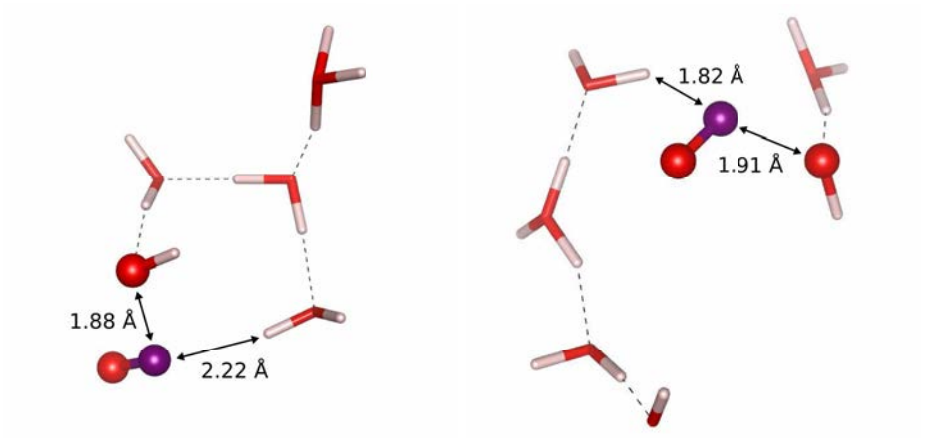

Figure 4.14: *Observed transition states at 300K, without an electric field (left) and with an electric field (right)*

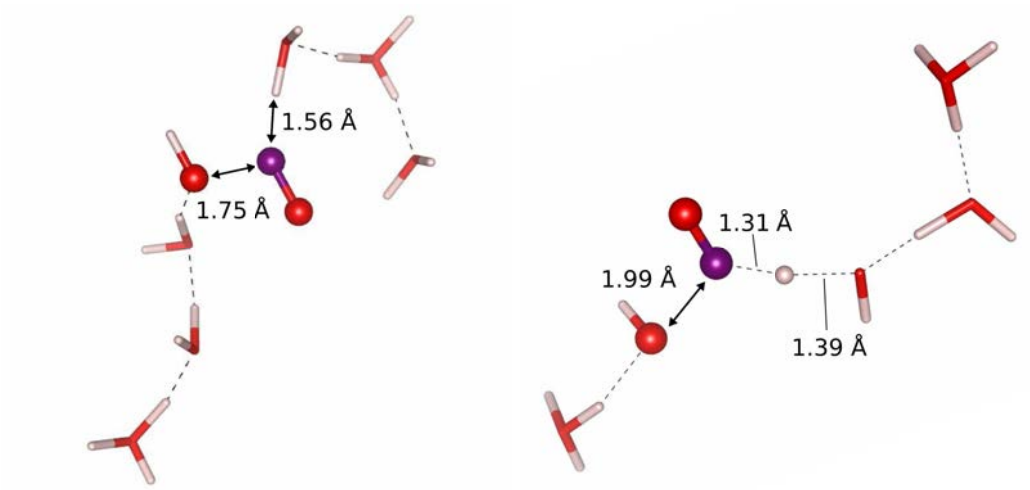

Figure 4.15: *Observed transition states at 400K, without an electric field (left) and with an electric field (right)*

taken from the first passage of the metadynamics, however one must acknowledge that other pathways are possible, and should be investigated in more precise commitor analysis. The advantage of the methods and collective variables used is that specific configurations of the reaction path are not known *a priori*.

4.7 Conclusion

The free energy landscape of this simple reaction is greatly affected by the presence of an electric field, and by the presence of the MgO surface. The surface and electric field exhibit some similarities in their effects on the reaction, such as orientation of the molecules, similar transition states and similar selection of the trans-isomer over the cis-isomer. On the surface and in the field, the product (formic acid) is significantly more stable than in the bulk, by about 7 kcal/mol

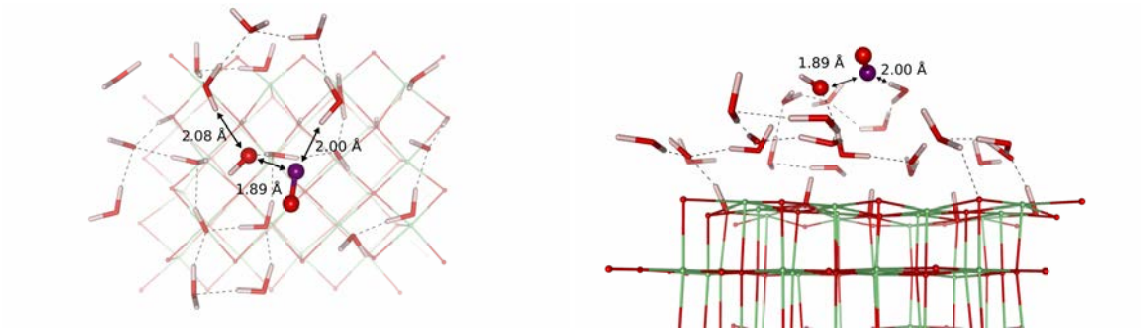

Figure 4.16: *Observed transition state at 400K on the MgO surface*

in the field, and by 40 kcal/mol on the surface. We conclude that the surface electric field is probably significant in the overall catalytic activity of the surface, and that catalysis may occur in near surface conditions without direct adsorption needing to take place. Perspectives include a finer analysis of the hydrogen bonding network of the solvent, and its contribution the the free energy landscape. The local pH effects could also be investigated by running simulations with ion pairs such as HCl or NaOH. Finally, such a simulation could be reproduced in the potential mimicking the surface electric field (chapter 3) to see if the field alone can reproduce the stabilisation of the product.

Chapter 5

Conclusions and Perspectives

Several conclusions may be made from this work. Firstly, it is clear that the electric field at various surfaces of MgO is high and localised. This probably applies to other oxide surface, as well as other mineral surfaces in general. The specific impact of this field has rarely to date been investigated at the atomic scale. Indeed, it seems that the electric field one usually talks about is a macroscopic value, and the averaging methods discussed in the first chapter have been used in the second chapter to attain a meaningful field from microscopic charge densities. The fields at the atomic scale are extremely high and are as felt by the valence electrons in the proximity of other atoms. The point of view presented here is thus different from, but not incompatible with, usual definitions of the surface electric field, for example coming from a charged surface as in the electric double layer theory. Indeed, on our model surface there is a residual field in the surface normal direction in the vacuum, although the net charge on the surface is zero. To regain the full electric double layer from atomistic simulations is unattainable with present computing power, especially in the *ab initio* framework, but also when using force fields — the second layer can be up to micrometers thick. However by understanding the surface electric field in detail, models may be created in which explicit surface atoms are not needed. One of the perspectives coming from this work would be to go further into setting up an electrostatic potential which correctly mimicks the surface electric field.

Formic acid is relevant in the prebiotic context outlined in the introduction, but also has applications in industry. In chapter 4 it was shown that one of the reaction pathways of formic acid can be strongly altered by both a homogeneous electric field, and the presence of the MgO(001) surface. The heavy computational cost of the simulation is a trade-off for the fact that all atoms were explicitly taken into account at the *abinitio* level, and this was necessary for this study to fully model chemical reactions and polarisability of atoms and molecules in a heterogeneous medium. The difference in stability of formic acid on the surface and

in the bulk is promising for prebiotic chemistry research. Here we demonstrate explicitly that the near surface environment strongly modifies several aspects of the reaction, in ways that cannot be explained by chemical arguments alone, for example specific adsorbtion to the surface. Rather the confinement, orientation and polarisation of the solvent molecules seem to play an important part, as the isomer selection and orientiation of the product molecule seems analogous to the effect of an applied electric field. Effects due to the local pH of the surface have not yet been investigated. Although the unit cell is neutral, MgO has a PZC of about 10 [37], meaning that at neutral pH the surface is acidic. It would be worth calculating the free energy landscape of the same reactions at acidic and basic pH to see if the effects are similar to applying an external field, or to surface effects. Because of the small size of the box, a realistic pH cannot be obtained however, qualitative results may be obtained, and such calculations are ongoing.

Perspectives coming from this work include modelling more complex prebiotic reactions at mineral surfaces. Due to heavy computational demands of such simulations, polarisable and reactive force-fields would need to be used, or alternatively, if the surface electric field proves to be a general proxy for surface reactivity, simple electrostatic models could replace the surface atoms, while the reactive atoms could still be treated at the DFT level. Obtaining well converged free energy landscapes could then be useful for modelling prebiotic processes on a longer timescale. Furthermore, generalising near-surface chemistry could have a strong impact in the prebiotic field. Questions raised about the first forms of metabolism rely on surface chemistry being drastically different from aqueous solution chemistry [105, 106], and surfaces have a probable role in not only increasing concentration of potential biomolecules, but also catalysing polymerisation. Any confirmation that surface proximity can also modify kinetics and thermodynamics of reactions, as well as stabilising certain species, could hint to significantly different chemistry at interfaces and have a real impact on origin of life studies.

Appendices

Appendix A

Simulation Details

A.1 Computational Details

All simulations presented in this work were performed with Quantum Espresso [41] version 4.3.2 or later. A home-modified version of the Plumed 1.3 plugin [107] was used to perform metadynamics and umbrella sampling.

A.1.1 AIMD with Quantum Espresso

Parameters for the DFT calculations using the plane waves code of the Quantum Espresso package are as follows:
time-step = 8.0 a.u. (Ry) = 0.388 fs
cut-off for wavefunction = 35 Ry
cut-off for charge density = 280 Ry
gaussian smearing for Brillouin zone integration = 0.01 Ry
the Grimme correction was applied for van-der-Walls interactions [108] (keyword: london=.TRUE.)
Charge density Broyden mixing, with local density dependant Thomas-Fermi screening (keyword: mixing_ mode='local_TF')
mixing factor for self consistency (keyword: mixing_beta = 0.5)
k-point sampling only done at the Γ point.

Parameters for the Car-Parrinello simulations are as follows:
time-step = 4.0 a.u. (Ha) = 0.0968 fs
same cut-offs as for the PW calculations
dimensions for the grid of ultrasoft pseudopotentials (square box): nr1b = nr2b = nr3b = 20
Grimme correction as in the PW calculations
effective electron mass = 300.0 a.u.
electron mass cut-off = 4.0 Ry

Γ k-point sampling as in the PW simulations.

Dynamics:
The verlet algorithm was used (keyword ion_dynamics = 'verlet')
with velocity rescaling. For 300K the tolerance was ± 50K, and for 400K the tolerance was set to ± 60K (keywords tempw and tolp)

Pseudopotentials:
All Pseudopotentials used in this work are ultrasoft pseudopotentials. They can be downloaded at the Qantum Espresso website [41].
Mg.pbe-mt_fhi.UPF
O.pbe-rkkjus.UPF
C.pbe-rkkjus.UPF
H.pbe-rkkjus.UPF

A.1.2 Metadynamics and Umbrella Sampling with the Plumed Plugin

The modified version of the plumed plugin was made to include the path collective variables based on coordination number. Questions about this code should be adressed to Fabio Pietrucci — fabio.pietrucci@impmc.upmc.fr.

The chosen cut-off for the coordination numbers are:
R^0_{CC} : 3.40 bohr
R^0_{CO} : 3.40 bohr
R^0_{CH} : 2.83 bohr
R^0_{OO} : 2.83 bohr
R^0_{OH} : 2.65 bohr
Parameters in the switching function 2.50 are $N = 6$, $M = 12$.

Hills deposited during the metadynamics are 0.02 Rydberg high, and have dimensions in s, z space of $0.03, 0.025$. The rate of deposition is once every 100 timesteps in the CP case, and every 25 timesteps in the PW case, meaning every 9.68 fs in both cases.

Umbrella sampling was performed by adding quadratic upper and lower walls to the s and z coordinates. The umbrella positions and steepness were set manually in each case, depending on the path and on the areas which required more statistics. Every simulation ended up requiring 30 to 40 umbrellas. The process was tedious and could eventually be automatised. Full details of each umbrella

sampling run is not given here, contact saralaporte@gmail.com should you require any further details.

A.2 System Descriptions

MgO(001) The optimal theoretical lattice parameter for MgO was found to be a = 4.22 Å. The MgO(001) slab is 12.66 Å thick with 7 MgO layers in the z direction, with the central layer clamped at bulk atomic positions, followed by 19.83 Å of vacuum or water. This distance between the periodic replicas of the slab was chosen by checking energy convergence so as to avoid interaction between replicas, and optimised with respect to total energy when 34 water molecules where added. The x and y dimensions of the supercell were chosen to match the (2×3) reconstruction of the known water ad-layer on MgO(001). The dimensions of the supercell are thus $(\frac{2}{\sqrt{2}} \times \frac{3}{\sqrt{2}} \times 7.7)a$ or $(5.97 \times 8.95 \times 32.49)$ Å.

Bulk water + CO (to formic acid) The bulk liquid supercells are cubes of 10.051 Å long, each initially with 34 water molecules and one carbon monoxide molecule, setting the density to 1g/cm^3. For simulations in an electric field, the field was applied via the modern theory of polarisation, see chapter 2.

MgO(001) + water + CO (to formic acid) The supercells used to simulate the surface consisted of MgO layers arranged in a slab geometry, 6 layers of MgO in the (100) direction (here chosen as the z direction) followed by liquid water. The dimensions of the box are (11.94×8.94×32.49) Å. Between the slabs there are a total of 66 water molecules and 2 carbon monoxide molecules.

Bibliography

[1] S. L. Miller, "A production of amino acids under possible primitive earth conditions," *Science*, vol. 117, no. 3046, pp. pp. 528–529, 1953. http://www.jstor.org/stable/1680569

[2] A. M. Saitta and F. Saija, "Miller experiments in atomistic computer simulations," *Proceedings of the National Academy of Sciences*, 2014. http://www.pnas.org/content/early/2014/09/03/1402894111.abstract

[3] J. Peretó, J. L. Bada, and A. Lazcano, "Charles darwin and the origin of life," *Origins of Life and Evolution of Biospheres*, vol. 39, no. 5, pp. 395–406, 2009. http://dx.doi.org/10.1007/s11084-009-9172-7

[4] T. A. E. Jakschitz and B. M. Rode, "Chemical evolution from simple inorganic compounds to chiral peptides," *Chem. Soc. Rev.*, vol. 41, pp. 5484–5489, 2012. http://dx.doi.org/10.1039/C2CS35073D

[5] H. J. Cleaves, "Prebiotic chemistry: Geochemical context and reaction screening," *Life*, vol. 3, no. 2, p. 331, 2013. http://www.mdpi.com/2075-1729/3/2/331

[6] C. Meinert, I. Myrgorodska, P. de Marcellus, T. Buhse, L. Nahon, S. V. Hoffmann, L. L. S. d'Hendecourt, and U. J. Meierhenrich, "Ribose and related sugars from ultraviolet irradiation of interstellar ice analogs," *Science*, vol. 352, no. 6282, pp. 208–212, 2016. http://science.sciencemag.org/content/352/6282/208

[7] K. Altwegg, H. Balsiger, A. Bar-Nun, J.-J. Berthelier, A. Bieler, P. Bochsler, C. Briois, U. Calmonte, M. R. Combi, H. Cottin, J. De Keyser, F. Dhooghe, B. Fiethe, S. A. Fuselier, S. Gasc, T. I. Gombosi, K. C. Hansen, M. Haessig, A. Jäckel, E. Kopp, A. Korth, L. Le Roy, U. Mall, B. Marty, O. Mousis, T. Owen, H. Rème, M. Rubin, T. Sémon, C.-Y. Tzou, J. Hunter Waite, and P. Wurz, "Prebiotic chemicals|amino acid and phosphorus|in the coma of comet 67p/churyumov-gerasimenko," *Science Advances*, vol. 2, no. 5, 2016. http://advances.sciencemag.org/content/2/5/e1600285

[8] Z. Martins, M. C. Price, N. Goldman, M. A. Sephton, and M. J. Burchell, "Shock synthesis of amino acids from impacting cometary and icy planet surface analogues," *Nature Geosci*, vol. 6, pp. 1045–1049, 2013.

[9] A. Roldan, N. Hollingsworth, A. Roffey, H. Islam, J. B. M. Goodall, C. R. A. Catlow, J. A. Darr, W. Bras, G. Sankar, K. B. Holt, G. Hogarth, and N. H. de Leeuw, "Bio-inspired CO_2 conversion by iron sulfide catalysts under sustainable conditions," *Chem. Commun.*, vol. 51, pp. 7501–7504, 2015. http://dx.doi.org/10.1039/C5CC02078F

[10] L. Orgel, "Polymerization on the rocks: Theoretical introduction," *Origins of life and evolution of the biosphere*, vol. 28, no. 3, pp. 227–234, 1998. http://dx.doi.org/10.1023/A%3A1006595411403

[11] J.-F. Lambert, "Adsorption and polymerization of amino acids on mineral surfaces: A review," *Origins of Life and Evolution of Biospheres*, vol. 38, no. 3, pp. 211–242, 2008. http://dx.doi.org/10.1007/s11084-008-9128-3

[12] A. Motta, M.-P. Gaigeot, and D. Costa, "Aimd evidence of inner sphere adsorption of glycine on a stepped (101) boehmite alooh surface," *The Journal of Physical Chemistry C*, vol. 116, no. 44, pp. 23 418–23 427, 2012. http://pubs.acs.org/doi/abs/10.1021/jp307565p

[13] T. Saarenketo, "Electrical properties of water in clay and silty soils," *Journal of Applied Geophysics*, vol. 40, no. 1{3, pp. 73 – 88, 1998. http://www.sciencedirect.com/science/article/pii/S0926985198000172

[14] S. J. Cox, Z. Raza, S. M. Kathmann, B. Slater, and A. Michaelides, "The microscopic features of heterogeneous ice nucleation may affect the macroscopic morphology of atmospheric ice crystals," *Faraday Discuss.*, vol. 167, pp. 389–403, 2013. http://dx.doi.org/10.1039/C3FD00059A

[15] S. Civiš, R. Szabla, B. M. Szyja, D. Smykowski, O. Ivanek, A. Knížek, P. Kubelík, J. Šponer, M. Ferus, and J. E. Šponer, "Tio2-catalyzed synthesis of sugars from formaldehyde in extraterrestrial impacts on the early earth," *Scientific Reports*, vol. 6, p. 23199, 2016.

[16] N. N. Nair, E. Schreiner, and D. Marx, "Glycine at the pyrite–water interface: The role of surface defects," *Journal of the American Chemical Society*, vol. 128, no. 42, pp. 13 815–13 826, 2006, pMID: 17044710. http://dx.doi.org/10.1021/ja063295a

[17] G. Wächtershäuser, "Groundworks for an evolutionary biochemistry: The iron-sulphur world," *Progress in Biophysics and Molecular Biology*, vol. 58,

no. 2, pp. 85 – 201, 1992. http://www.sciencedirect.com/science/article/pii/007961079290022X

[18] S. F. Mason, "Origins of biomolecular handedness," *Nature*, vol. 311, pp. 19–23, 1984.

[19] P. G. Gopal, R. L. Schneider, and K. L. Watters, "Evidence for production of surface formate upon direct reaction of {CO} with alumina and magnesia," *Journal of Catalysis*, vol. 105, no. 2, pp. 366 – 372, 1987. http://www.sciencedirect.com/science/article/pii/0021951787900662

[20] G. Cicero, J. C. Grossman, E. Schwegler, F. Gygi, and G. Galli, "Water confined in nanotubes and between graphene sheets: A first principle study," *Journal of the American Chemical Society*, vol. 130, no. 6, pp. 1871–1878, 2008. http://pubs.acs.org/doi/abs/10.1021/ja074418%2B

[21] S. Kaya, D. Schlesinger, S. Yamamoto, J. T. Newberg, H. Bluhm, H. Ogasawara, T. Kendelewicz, G. E. Brown, L. G. M. Pettersson, and A. Nilsson, "Highly compressed two-dimensional form of water at ambient conditions," *Sci. Rep.*, vol. 3, 2015. http://www.nature.com/srep/2013/130115/srep01074/abs/srep01074.html#supplementary-information

[22] S. Laporte, F. Finocchi, L. Paulatto, M. Blanchard, E. Balan, F. Guyot, and A. M. Saitta, "Strong electric fields at a prototypical oxide/water interface probed by ab initio molecular dynamics: Mgo(001)," *Phys. Chem. Chem. Phys.*, vol. 17, pp. 20 382–20 390, 2015. http://dx.doi.org/10.1039/C5CP02097B

[23] L. Vlcek, Z. Zhang, M. L. Machesky, P. Fenter, J. Rosenqvist, D. J. Wesolowski, L. M. Anovitz, M. Predota, and P. T. Cummings, "Electric double layer at metal oxide surfaces: Static properties of the cassiterite-water interface," *Langmuir*, vol. 23, no. 9, pp. 4925–4937, 2007, pMID: 17381142. http://pubs.acs.org/doi/abs/10.1021/la063306d

[24] A. Schlaich, E. W. Knapp, and R. R. Netz, "Water dielectric effects in planar confinement," *Phys. Rev. Lett.*, vol. 117.

[25] O. Byl, J.-C. Liu, Y. Wang, W.-L. Yim, J. K. Johnson, and J. T. Yates, "Unusual hydrogen bonding in water-filled carbon nanotubes," *Journal of the American Chemical Society*, vol. 128, no. 37, pp. 12 090–12 097, 2006. http://pubs.acs.org/doi/abs/10.1021/ja057856u

[26] S. Han, M. Y. Choi, P. Kumar, and H. E. Stanley, "Phase transitions in confined water nanofilms," *Nat Phys*, vol. 6, pp. 685–689, 2009.

[27] A. C. Aragonès, N. L. Haworth, N. Darwish, S. Ciampi, N. J. Bloomfield, G. G. Wallace, I. Diez-Perez, and M. L. Coote, "Electrostatic catalysis of a diels-alder reaction," *Nature*, vol. 531, pp. 88–91, 2016.

[28] M. Osawa, M. Tsushima, H. Mogami, G. Samjeske, and A. Yamakata, "Structure of water at the electrified platinum–water interface: A study by surface-enhanced infrared absorption spectroscopy," *The Journal of Physical Chemistry C*, vol. 112, no. 11, pp. 4248–4256, 2008. http://pubs.acs.org/doi/abs/10.1021/jp710386g

[29] A. M. Saitta, F. Saija, and P. V. Giaquinta, "Ab initio," *Phys. Rev. Lett.*, vol. 108, p. 207801, May 2012. http://link.aps.org/doi/10.1103/PhysRevLett.108.207801

[30] H. J. Kreuzer, *Chemical Reactions in High Electric Fields*, ch. 19, pp. 268–286. http://pubs.acs.org/doi/abs/10.1021/bk-1992-0482.ch018

[31] G. Cassone, "Ab initio molecular dynamics simulations of h-bonded systems under an electric field," Ph.D. dissertation, Università degli Studi di Messina, Université Pierre et Marie Curie, 2016.

[32] G. Cassone, P. V. Giaquinta, F. Saija, and A. M. Saitta, "Liquid methanol under a static electric field," *The Journal of Chemical Physics*, vol. 142, no. 5, p. 054502, 2015. http://scitation.aip.org/content/aip/journal/jcp/142/5/10.1063/1.4907010

[33] S. D. Fried, S. Bagchi, and S. G. Boxer, "Extreme electric fields power catalysis in the active site of ketosteroid isomerase," *Science*, vol. 346, no. 6216, pp. 1510–1514, 2014. http://science.sciencemag.org/content/346/6216/1510

[34] Z. Hammadi, J.-P. Astier, R. Morin, and S. Veesler, "Protein crystallization induced by a localized voltage," *Crystal Growth & Design*, vol. 7, no. 8, pp. 1472–1475, 2007. http://pubs.acs.org/doi/abs/10.1021/cg070108r

[35] J. Lasne, A. Rosu-Finsen, A. Cassidy, M. R. S. McCoustra, and D. Field, "Spontaneous electric fields in solid carbon monoxide," *Phys. Chem. Chem. Phys.*, pp. 30 177–30 187, 2015. http://dx.doi.org/10.1039/C5CP04536C

[36] J. J. Lyklema, A. de Keizer, B. Bijsterbosch, G. Fleer, and M. C. S. (Eds.), *Solid-Liquid Interfaces*, ser. Fundamentals of Interface and Colloid Science 2. Elsevier, Academic Press, 1995. http://gen.lib.rus.ec/book/index.php?md5=145E94C05719008B3B7F73E2A5DA6E89

[37] M. Kosmulski, *Surface Charging and Points of Zero Charge*, ser. Surfactant Science. CRC Press, 2009. https://books.google.fr/books?id=ISm0HcKaSasC

[38] J. Cheng and M. Sprik, "The electric double layer at a rutile tio 2 water interface modelled using density functional theory based molecular dynamics simulation," *Journal of Physics: Condensed Matter*, vol. 26, no. 24, p. 244108, 2014. http://stacks.iop.org/0953-8984/26/i=24/a=244108

[39] R. Khatib and M. Sulpizi, *High Performance Computing in Science and Engineering '14: Transactions of the High Performance Computing Center, Stuttgart (HLRS) 2014*. Cham: Springer International Publishing, 2015, ch. The Fluorite/Water Interfaces: Structure and Spectroscopy from First Principles Simulations, pp. 179–190. http://dx.doi.org/10.1007/978-3-319-10810-0_13

[40] By Tosaka, wikimedia commons, CC BY 3.0. https://commons.wikimedia.org/w/index.php?curid=4484781

[41] P. Giannozzi, S. Baroni, N. Bonini, M. Calandra, R. Car, C. Cavazzoni, D. Ceresoli, G. L. Chiarotti, M. Cococcioni, I. Dabo, A. Dal Corso, S. de Gironcoli, S. Fabris, G. Fratesi, R. Gebauer, U. Gerstmann, C. Gougoussis, A. Kokalj, M. Lazzeri, L. Martin-Samos, N. Marzari, F. Mauri, R. Mazzarello, S. Paolini, A. Pasquarello, L. Paulatto, C. Sbraccia, S. Scandolo, G. Sclauzero, A. P. Seitsonen, A. Smogunov, P. Umari, and R. M. Wentzcovitch, "Quantum espresso: a modular and open-source software project for quantum simulations of materials," *Journal of Physics: Condensed Matter*, vol. 21, no. 39, p. 395502 (19pp), 2009. http://www.quantum-espresso.org

[42] J. M. Thijssen, *Computational Physics*, 2nd ed. Cambridge University Press, 2007.

[43] P. Hohenberg and W. Kohn, "Inhomogeneous electron gas," *Phys. Rev.*, vol. 136, pp. B864–B871, Nov 1964. http://link.aps.org/doi/10.1103/PhysRev.136.B864

[44] J. P. Perdew, K. Burke, and M. Ernzerhof, "Generalized gradient approximation made simple," *Phys. Rev. Lett.*, vol. 77, pp. 3865–3868, Oct 1996. http://link.aps.org/doi/10.1103/PhysRevLett.77.3865

[45] We used the pseudopotentials C.pbe-rrkjus.UPF, O.pbe-rrkjus.UPF and H.pbe-rrkjus.UPF from http://www.quantum-espresso.org.

[46] R. Car and M. Parrinello, "Unified approach for molecular dynamics and density-functional theory," *Phys. Rev. Lett.*, vol. 55, pp. 2471–2474, Nov 1985. http://link.aps.org/doi/10.1103/PhysRevLett.55.2471

[47] G. Pastore, E. Smargiassi, and F. Buda, "Theory of *ab initio* molecular-dynamics calculations," *Phys. Rev. A*, vol. 44, pp. 6334–6347, Nov 1991. http://link.aps.org/doi/10.1103/PhysRevA.44.6334

[48] P. Umari and A. Pasquarello, "Car-parinello molecular dynamics in a finite homogeneous electric field," in *AIP Conference Proceedings*, vol. 677, 2003, pp. 269–275.

[49] R. Resta and D. Vanderbilt, *Physics of Ferroelectrics: a Modern Perspective*. Springer-Verlag, 2007, ch. 2 — Theory of Polarization: A Modern Approach.

[50] D. Xiao, M.-C. Chang, and Q. Niu, "Berry phase effects on electronic properties," *Rev. Mod. Phys.*, vol. 82, pp. 1959–2007, Jul 2010. http://link.aps.org/doi/10.1103/RevModPhys.82.1959

[51] A. Ruini, "Dynamical charges at surfaces and interfaces their role in the schottky barrier problem," Ph.D. dissertation, SCUOLA INTERNAZIONALE SUPERIORE DI STUDI AVANZATI, 1997.

[52] D. Branduardi, F. L. Gervasio, and M. Parrinello, "From A to B in free energy space," *The Journal of Chemical Physics*, vol. 126, no. 5, 2007. http://scitation.aip.org/content/aip/journal/jcp/126/5/10.1063/1.2432340

[53] F. Pietrucci and A. M. Saitta, "Formamide reaction network in gas phase and solution via a unified theoretical approach: Toward a reconciliation of different prebiotic scenarios," *Proceedings of the National Academy of Sciences*, vol. 112, no. 49, pp. 15 030–15 035, 2015. http://www.pnas.org/content/112/49/15030.abstract

[54] A. Laio and M. Parrinello, "Escaping free-energy minima," *Proceedings of the National Academy of Sciences*, vol. 99, no. 20, pp. 12 562–12 566, 2002. http://www.pnas.org/content/99/20/12562.abstract

[55] S. Kumar, J. M. Rosenberg, D. Bouzida, R. H. Swendsen, and P. A. Kollman, "The weighted histogram analysis method for free-energy calculations on biomolecules. i. the method," *Journal of Computational Chemistry*, vol. 13, no. 8, pp. 1011–1021, 1992. http://dx.doi.org/10.1002/jcc.540130812

[56] A. Grossfield, "Wham: the weighted histogram analysis method." http://membrane.urmc.rochester.edu/content/wham

[57] G. E. Ewing, "Ambient thin film water on insulator surfaces," *Chemical Reviews*, vol. 106, no. 4, pp. 1511–1526, 2006. http://pubs.acs.org/doi/abs/10.1021/cr040369x

[58] A. Marshall, B. Børresen, G. Hagen, M. Tsypkin, and R. Tunold, "Preparation and characterisation of nanocrystalline Ir_xSn_1–xO_2 electrocatalytic powders," *Mater. Chem. Phys.*, vol. 94, no. 2-3, pp. 226 – 232, 2005. http://www.sciencedirect.com/science/article/pii/S0254058405002750

[59] J. Rossmeisl, Z.-W. Qu, H. Zhu, G.-J. Kroes, and J. Nørskov, "Electrolysis of water on oxide surfaces," *J. Elec. Chem.*, vol. 607, no. 1–2, pp. 83 – 89, 2007, theoretical and Computational Electrochemistry. http://www.sciencedirect.com/science/article/pii/S0022072806006371

[60] A. N. Cormack and A. Tilocca, "Structure and biological activity of glasses and ceramics," *Phil. Trans. R. Soc. A*, vol. 370, no. 1963, pp. 1271–1280, 2012.

[61] O. Robach, G. Renaud, and A. Barbier, "Very-high-quality mgo(001) surfaces: roughness, rumpling and relaxation," *Surface Science*, vol. 401, no. 2, pp. 227 – 235, 1998. http://www.sciencedirect.com/science/article/pii/S0039602897010820

[62] P. Geysermans, F. Finocchi, J. Goniakowski, R. Hacquart, and J. Jupille, "Combination of (100), (110) and (111) facets in MgO crystals shapes from dry to wet environment," *Phys. Chem. Chem. Phys.*, vol. 11, pp. 2228–2233, 2009. http://dx.doi.org/10.1039/B812376D

[63] G. Jordan, S. R. Higgins, and C. M. Eggleston, "Dissolution of the periclase (001) surface: a scanning force microscope study," *Am. Mineral.*, vol. 84, p. 144, 1999.

[64] D. Costa, C. Chizallet, B. Ealet, J. Goniakowski, and F. Finocchi, "Water on extended and point defects at mgo surfaces," *J. Chem. Phys.*, vol. 125, no. 5, p. 054702, 2006. http://scitation.aip.org/content/aip/journal/jcp/125/5/10.1063/1.2212407

[65] R. S. Alvim, I. B. Jr, D. G. Costa, and A. A. Leitao, "Density-functional theory simulation of the dissociative chemisorption of water molecules on the MgO(001) surface," *J. Phys. Chem. C*, vol. 116, p. 738, 2011.

[66] P. Liu, T. Kendelewicz, G. E. Gordon, and G. A. Parks, "Reaction of water with MgO(100) surfaces. part i:: Synchrotron x-ray photoemission studies of low-defect surfaces," *Surf. Sci.*, vol. 413, p. 287, 1998.

[67] J. T. Newberg, D. E. Starr, S. Yamamoto, S. Kaya, T. Kendelewicz, E. R. Mysak, S. Porsgaard, M. B. Salmeron, G. E. Brown, A. Nilsson, and H. Bluhm, "Autocatalytic surface hydroxylation of MgO(100) terrace sites observed under ambient conditions," *J. Phys. Chem. C*, vol. 115, no. 26, pp. 12 864–12 872, 2011. http://dx.doi.org/10.1021/jp200235v

[68] R. Wlodarczyk, M. Sierka, K. Kwapien, J. Sauer, E. Carrasco, A. Aumer, J. F. Gomes, M. Sterrer, and H.-J. Freund, "Structures of the ordered water monolayer on MgO(001)," *The Journal of Physical Chemistry C*, vol. 115, no. 14, pp. 6764–6774, 2011. http://pubs.acs.org/doi/abs/10.1021/jp200112c

[69] L. Giordano, J. Goniakowski, and J. Suzanne, "Partial dissociation of water molecules in the (3×2) water monolayer deposited on the mgo (100) surface," *Phys. Rev. Lett.*, vol. 81, pp. 1271–1273, Aug 1998. http://link.aps.org/doi/10.1103/PhysRevLett.81.1271

[70] C. Toubin, S. Picaud, and C. Girardet, "Adsorption of small polar molecules as a probe of the surface electric field created by water layers supported by MgO(100): a theoretical study," *Chem. Phys.*, vol. 244, no. 2-3, pp. 227 – 249, 1999. http://www.sciencedirect.com/science/article/pii/S0301010499001603

[71] M. Foster, M. D'Agostino, and D. Passno, "Water on MgO(100)–an infrared study at ambient temperatures," *Surf. Sci.*, vol. 590, p. 31, 2005.

[72] D. Spagnoli, J. P. Allen, and S. C. Parker, "The structure and dynamics of hydrated and hydroxylated magnesium oxide nanoparticles," *Langmuir*, vol. 27, no. 5, pp. 1821–1829, 2011. http://pubs.acs.org/doi/abs/10.1021/la104190d

[73] S. A. Deshmukh and S. K. R. S. Sankaranarayanan, "Atomic scale characterization of interfacial water near an oxide surface using molecular dynamics simulations," *Phys. Chem. Chem. Phys.*, vol. 14, pp. 15 593–15 605, 2012. http://dx.doi.org/10.1039/C2CP42308A

[74] F. Tielens and C. Minot, "Dft study of the water/MgO(100) interface in acidic and basic media," *Surf. Sci.*, vol. 600, p. 357, 2006.

[75] M. Nonnenmacher, M. P. O'Boyle, and H. K. Wickramasinghe, "Kelvin probe force microscopy," *Applied Physics Letters*, vol. 58, no. 25, pp. 2921–2923, 1991. http://scitation.aip.org/content/aip/journal/apl/58/25/10.1063/1.105227

[76] Y. Xu, J. Li, Y. Zhang, and W. Chen, "{CO} adsorption on MgO(001) surface with oxygen vacancy and its low-coordinated surface sites: embedded cluster model density functional study employing charge self-consistent technique," *Surface Science*, vol. 525, no. 1{3, pp. 13 – 23, 2003. http://www.sciencedirect.com/science/article/pii/S0039602802025669

[77] M. Otani and O. Sugino, "First-principles calculations of charged surfaces and interfaces: A plane-wave nonrepeated slab approach," *Phys. Rev. B*, vol. 73, p. 115407, Mar 2006. http://link.aps.org/doi/10.1103/PhysRevB.73.115407

[78] A. D'Ercole, A. M. Ferrari, and C. Pisani, "On the role of electrostatics in the heterolytic splitting of covalent bonds at defective oxide surfaces," *The Journal of Chemical Physics*, vol. 115, no. 1, pp. 509–518, 2001. http://link.aip.org/link/?JCP/115/509/1

[79] J. Y. Lim, J. S. Oh, B. D. Ko, J. Won Cho, S. O. Kang, G. Cho, H. S. Uhm, and E. H. Choi, "Work function of mgo single crystals from ion-induced secondary electron emission coefficient," *Journal of Applied Physics*, vol. 94, no. 1, pp. 764–769, 2003. http://scitation.aip.org/content/aip/journal/jap/94/1/10.1063/1.1581376

[80] S. M. Kathmann, I.-F. W. Kuo, C. J. Mundy, and G. K. Schenter, "Understanding the surface potential of water," *The Journal of Physical Chemistry B*, vol. 115, no. 15, pp. 4369–4377, 2011, pMID: 21449605. http://dx.doi.org/10.1021/jp1116036

[81] C. Noguera and J. Goniakowski, "Polarity in oxide nano-objects," *Chemical Reviews*, vol. 113, no. 6, pp. 4073–4105, 2013. http://pubs.acs.org/doi/abs/10.1021/cr3003032

[82] F. Finocchi, P. Geysermans, and A. Bourgeois, "The role of hydroxylation in the step stability and in the interaction between steps: a first-principles study of vicinal mgo surfaces," *Phys. Chem. Chem. Phys.*, vol. 14, pp. 13 692–13 701, 2012. http://dx.doi.org/10.1039/C2CP41835E

[83] D. Raymand, A. C. van Duin, W. A. Goddard, K. Hermansson, and D. Spångberg, "Hydroxylation structure and proton transfer reactivity at the zinc oxide–water interface," *The Journal of Physical Chemistry C*, vol. 115, no. 17, pp. 8573–8579, 2011. http://pubs.acs.org/doi/abs/10.1021/jp106144p

[84] S. O. Baumann, J. Schneider, A. Sternig, D. Thomele, S. Stankic, T. Berger, H. Grönbeck, and O. Diwald.

[85] J. Coulomb, B. Demirdjian, D. Ferry, and M. Trabelsi, "Thermodynamic and structural properties of water adsorbed film on mgo (100) ionic surface," *Adsorption*, vol. 19, no. 2-4, pp. 861–867, 2013. http://dx.doi.org/10.1007/s10450-013-9538-z

[86] B. Rotenberg, A. J. Patel, and D. Chandler, "Molecular explanation for why talc surfaces can be both hydrophilic and hydrophobic," *Journal of the American Chemical Society*, vol. 133, no. 50, pp. 20 521–20 527, 2011. http://pubs.acs.org/doi/abs/10.1021/ja208687a

[87] G. Tocci, L. Joly, and A. Michaelides, "Friction of water on graphene and hexagonal boron nitride from ab initio methods: Very different slippage despite very similar interface structures," *Nano Letters*, vol. 14, no. 12, pp. 6872–6877, 2014, pMID: 25394228. http://dx.doi.org/10.1021/nl502837d

[88] G. Tocci and A. Michaelides, "Solvent-induced proton hopping at a water{oxide interface," *The Journal of Physical Chemistry Letters*, vol. 5, no. 3, pp. 474–480, 2014. http://dx.doi.org/10.1021/jz402646c

[89] G. Cassone, P. V. Giaquinta, F. Saija, and A. M. Saitta, "Effect of electric field orientation on the mechanical and electrical properties of water ices: An ab-initio study," *The Journal of Physical Chemistry B*, vol. 118, no. 44, pp. 12 717–12 724, 2014, pMID: 25265517. http://dx.doi.org/10.1021/jp507376v

[90] G. Cassone*, P. V. Giaquinta, F. Saija, and A. M. Saitta, "Proton conduction in water ices under an electric field," *The Journal of Physical Chemistry B*, vol. 118, no. 16, pp. 4419–4424, 2014, pMID: 24689531. http://dx.doi.org/10.1021/jp5021356

[91] M. Dagrada, M. Casula, A. M. Saitta, S. Sorella, and F. Mauri, "Quantum monte carlo study of the protonated water dimer," *Journal of Chemical Theory and Computation*, vol. 10, no. 5, pp. 1980–1993, 2014. http://dx.doi.org/10.1021/ct401077x

[92] Y. Bronstein, P. Depondt, F. Finocchi, and A. M. Saitta, "Quantum-driven phase transition in ice described via an efficient langevin approach," *Phys. Rev. B*, vol. 89, p. 214101, Jun 2014. http://link.aps.org/doi/10.1103/PhysRevB.89.214101

[93] Z. Ma and M. E. Tuckerman, "On the connection between proton transport, structural diffusion, and reorientation of the hydrated hydroxide ion as a function of temperature," *Chemical Physics Letters*, vol. 511, no. 4{6,

pp. 177 – 182, 2011. http://www.sciencedirect.com/science/article/pii/S0009261411006762

[94] N. Akiya and P. E. Savage, "Role of water in formic acid decomposition," *AIChE Journal*, vol. 44, no. 2, pp. 405–415, 1998. http://dx.doi.org/10.1002/aic.690440217

[95] Y. Yasaka, K. Yoshida, C. Wakai, N. Matubayasi, and M. Nakahara, "Kinetic and equilibrium study on formic acid decomposition in relation to the water-gas-shift reaction," *The Journal of Physical Chemistry A*, vol. 110, no. 38, pp. 11 082–11 090, 2006, pMID: 16986841. http://dx.doi.org/10.1021/jp0626768

[96] J. Yu and P. E. Savage, "Decomposition of formic acid under hydrothermal conditions," *Industrial & Engineering Chemistry Research*, vol. 37, no. 1, pp. 2–10, 1998. http://dx.doi.org/10.1021/ie970182e

[97] C. Melius, N. Bergan, and J. Shepherd, "Effects of water on combustion kinetics at high pressure," *Symposium (International) on Combustion*, vol. 23, no. 1, pp. 217 – 223, 1991, twenty-Third Symposium (International) on Combustion. http://www.sciencedirect.com/science/article/pii/S0082078406802626

[98] N. Matubayasi and M. Nakahara, "Hydrothermal reactions of formaldehyde and formic acid: Free-energy analysis of equilibrium," *The Journal of Chemical Physics*, vol. 122, no. 7, p. 74509, 2005. http://scitation.aip.org/content/aip/journal/jcp/122/7/10.1063/1.1849165

[99] H.-T. Chen, J.-G. Chang, and H.-L. Chen, "A computational study on the decomposition of formic acid catalyzed by (h2o)x, x = 0–3: Comparison of the gas-phase and aqueous-phase results," *The Journal of Physical Chemistry A*, vol. 112, no. 35, pp. 8093–8099, 2008, pMID: 18690674. http://dx.doi.org/10.1021/jp801247d

[100] B. Lippens and A. Webb, "Formic acid synthesis," Sep. 18 1973, uS Patent 3,759,990. http://www.google.com/patents/US3759990

[101] F. R. Negreiros, E. Apra, G. Barcaro, L. Sementa, S. Vajda, and A. Fortunelli, "A first-principles theoretical approach to heterogeneous nanocatalysis," *Nanoscale*, vol. 4, pp. 1208–1219, 2012. http://dx.doi.org/10.1039/C1NR11051A

[102] A. E. Kuznetsov and D. G. Musaev, "Does the mgo(100)-support facilitate the reaction of nitrogen and hydrogen molecules catalyzed

by zr2pd2 clusters? a computational study," *Inorganic Chemistry*, vol. 49, no. 5, pp. 2557–2567, 2010, pMID: 20128599. http://dx.doi.org/10.1021/ic902531p

[103] E. Schreiner, N. N. Nair, C. Wittekindt, and D. Marx, "Peptide synthesis in aqueous environments: The role of extreme conditions and pyrite mineral surfaces on formation and hydrolysis of peptides," *Journal of the American Chemical Society*, vol. 133, no. 21, pp. 8216–8226, 2011. http://pubs.acs.org/doi/abs/10.1021/ja111503z

[104] C. Xu and D. W. Goodman, "Surface chemistry of polar oxide surfaces: formic acid on nio (111)," *J. Chem. Soc., Faraday Trans.*, vol. 91, pp. 3709–3715, 1995. http://dx.doi.org/10.1039/FT9959103709

[105] C. de Duve and S. L. Miller, "Two-dimensional life?" *Proceedings of the National Academy of Sciences*, vol. 88, no. 22, pp. 10014–10017, 1991. http://www.pnas.org/content/88/22/10014.abstract

[106] G. Wächtershäuser, "Before enzymes and templates: theory of surface metabolism." *Microbiological Reviews*, vol. 52, pp. 452–484, 1988. http://www.ncbi.nlm.nih.gov/pmc/articles/PMC373159/

[107] M. Bonomi, D. Branduardi, G. Bussi, C. Camilloni, D. Provasi, P. Raiteri, D. Donadio, F. Marinelli, F. Pietrucci, R. A. Broglia, and M. Parrinello, "Plumed: A portable plugin for free-energy calculations with molecular dynamics," *Computer Physics Communications*, vol. 180, no. 10, pp. 1961 – 1972, 2009. http://www.sciencedirect.com/science/article/pii/S001046550900157X

[108] S. Grimme, "Semiempirical gga-type density functional constructed with a long-range dispersion correction," *Journal of Computational Chemistry*, vol. 27, no. 15, pp. 1787–1799, 2006. http://dx.doi.org/10.1002/jcc.20495